ALKALI METAL BEAMS FROM SOLID STATE ELECTROCHEMICAL SOURCES

Stephen Campbell Roy

A Thesis Submitted for the Degree of PhD
at the
University of St Andrews

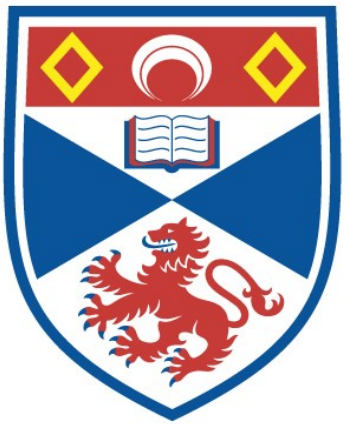

1995

ALKALI METAL BEAMS FROM SOLID STATE ELECTROCHEMICAL SOURCES

A thesis presented for the degree of *Doctor of Philosophy* in the Faculty of Science of the University of St Andrews by Stephen Campbell Roy, B.Sc..

September 1994,

Centre for Electrochemical and Materials Sciences,

Department of Chemistry, St Andrews.

Declaration

I, Stephen Campbell Roy, certify that this thesis has been composed by myself, that it is a record of my own work, and that it has not been submitted in any previous application for a Higher Degree.

This thesis describes the results of research carried out in the Department of Chemistry, University of St Andrews, under the supervision of Dr P. G. Bruce since 1st October 1991.

September 1994 Signed:

I was admitted to the Faculty of Science in the University of St Andrews under Ordinance General No. 12 on 1st October 1991 and as a candidate for the degree of Ph.D. on 26th August 1992.

Signed:

Certification

I hereby certify that Stephen Campbell Roy has spent twelve terms of research work under my supervision and that he has fulfilled the conditions of the Resolution and Regulations appropriate to the degree of Doctor of Philosophy.

September 1994 Signed:

P. G. Bruce

Library Declaration

In submitting this thesis to the University of St Andrews I understand that I am giving permission for it to be made available for use in accordance with the regulations of the University Library for the time being in force, subject to any copyright vested in the work not being affected thereby. I also understand that the title and abstract will be published, and that a copy of the work may be made and supplied to any *bona fide* library or research worker.

Signed:

Acknowledgements

My sincere thanks to:

Peter for introducing me to solid state electrochemistry and providing me with invaluable help and support throughout the past three years.

Phil, Dave, Gerry, Kevin, and Helen at Heriot-Watt University for their expertise and advice concerning the technological aspect of this work.

Jim, Joe, Brian, Colin, Marj, Andrew and Bobby for enabling the experimental apparatus to be built and used in such a short space of time. Jim in particular.

All members, past and present, of the Centre for Electrochemical and Materials Sciences (CEMS) for being good to work beside.

St Andrews University for funding me.

To my parents

Abstract

All solid state electrochemical cells capable of producing beams of lithium, sodium and potassium in ultrahigh vacuum have been developed and investigated. The evolution of alkali metal vapour has been demonstrated by deposition of the metal on a substrate during polarisation of the cell followed by ex-situ analysis of the metal using laser ionisation mass analysis (LIMA).

The electrochemistry of alkali metal evolution from these unusual solid state cells has been investigated using cyclic voltammetry, chronoamperometry and AC impedance measurements at pressures of 10^{-3} mbar and 10^{-8} mbar (UHV). It has been found for all three sources that the mechanism at relatively high pressure involves the nucleation and growth of liquid alkali metals or compounds containing alkali metals on the working electrode prior to their evaporation. In UHV the mechanism for potassium and sodium emission appears to involve the transfer of atoms directly into the gas phase whereas lithium exhibits nucleation and growth.

In order to obtain a more complete characterization of the electrochemical mechanisms a spectro-electrochemical technique involving the simultaneous mass spectrometric analysis of the evolved vapour under UHV conditions along with cyclic voltammetry was developed.

The formation of p-type ZnSe is essential to the fabrication of blue light emitting diodes and semiconductor lasers but has long represented a major problem in optoelectronics. This work shows that the potassium source can be used to p-dope ZnSe during growth of the material by molecular beam epitaxy (MBE). Efforts directed to the preparation of n-type diamond using a lithium source in microwave enhanced chemical vapour deposition (MWECVD) apparatus have demonstrated that the source can introduce lithium to diamond, although full semiconductor characterization of this material has yet to be made.

Chapter 1

Introduction

An important aim of this work was to prepare semiconductor materials with new solid state electrochemical cells capable of releasing lithium, sodium and potassium vapours. Details of these experiments can be found by consulting chapter 6. The majority of work, however, dealt with constructing the cells, ensuring that they could operate effectively and characterising the interfacial electrochemical mechanisms responsible for their ability to emit alkali metals.

This introduction therefore gives background concerning semiconductor properties and semiconductor growth technology; but firstly the scene is set with the following four sections on solid state electrochemistry and its applications.

1.1 Solid State Electrochemistry

Electrochemistry is approximately 200 years old. Many fundamental discoveries concerning the electrical properties of chemicals including the first observation of ionic mobility in solids [1] were made in the early nineteenth century by Michael Faraday. Whilst liquid electrochemistry and its applications were the subject of uninterrupted research after Faraday's work, little more was said about the solid state aspect until 1904 when Haber and Tolloczko [2] recognised that galvanic cells could be constructed with solid electrolytes. Prior to the mid-1930's, work had been carried out with the solid electrolyte analogues of most simple aqueous cell types, Faraday's law had been verified for such systems, and anion and cation transference numbers were determined in a variety of solids, such as the halides of silver and lead [3].

The next major experimental breakthrough in solid electrolytes did not occur until 1957 when Wagner and Kiukkola [4] presented an in-depth study of an oxide ion conductor consisting of 15 mol. % CaO in ZrO_2. This is now one of the most commonly used electrolytes in oxygen electrochemical devices such as fuel cells and sensors. Shortly after this revival, the silver based ionic conductor $RbAg_4I_5$ [5] and sodium beta alumina [6] were found to have magnitudes of ionic conductivity comparable with some aqueous electrolytes at ambient temperature. The prospect of obtaining all solid state batteries with numerous advantages over existing liquid based

systems thus became realizable and led to extensive research which continues to this day.

By 1970 the theoretical aspects of liquid electrochemistry had been developed to such an extent that Bockris and Reddy [7] stated it could essentially be divided into two areas; interfacial electrochemistry (electrodics) or the electrochemistry of bulk solutions (ionics). Their book was published in 1970; two years before the first Solid State Ionics (SSI) meeting.

Contrary to Bockris' and Reddy's nomenclature, SSI was devoted to reactions occurring both in and on solids e.g. conductivity measurements and intercalation respectively. More importantly, the first SSI meeting involved the introduction of intercalation electrochemistry. This subject was introduced because one of the major limitations in developing high energy density secondary batteries operable at room temperature was associated with the reversibility of the cathode material. Unlike solid electrolytes which conduct predominantly by ionic motion, intercalation compounds conduct by ions *and* electrons thus allowing them to function as reversible electrodes. The first intercalation compound was reported by Schauffautl in 1841 (it is a strange coincidence that at approximately the same time Faraday noticed ionic transport in a heated mixture of silver sulphide and lead fluoride).

There are many differences between liquid and solid state electrochemistry. The most obvious being conduction mechanisms. A detailed account of ionic mobility in aqueous electrolytes is beyond the scope of this thesis but reference [8] provides adequate information. Information concerning the conduction mechanisms of intercalation electrodes and solid electrolytes is provided in the following two sections.

All solid state electrochemical devices are a relatively new discovery and investigations of the solid electrolyte/electrode interface have only been carried out over the past 25 years. The state of knowledge in this area is therefore comparatively primitive and much dependent on the type of electrode interface under consideration. Reference [9], published in 1980, contains models of the solid electrolyte/electrode

interphase in a variety of situations and outlines some differences between these and the liquid electrolyte/electrode interface.

1.2 Solid Electrolytes

1) Types of Solid Electrolyte

Solid electrolytes (SEs) are inorganic solids in which one component of the structure, cationic or anionic, is not confined to specific lattice sites of the crystal structure but is essentially free to move throughout the structure. Table 1-1 lists some popular SEs along with their conductivities at specified temperatures.

Table 1-1

Conducting Ion	Chemical Formula	Trivial Name	Conductivity ($\Omega^{-1}cm^{-1}$)	Temperature (°C)
Na+	$Na_{1+x}Al_{11}O_{17+x/2}$	Na-BASE	0.1	300
Li^+	$Li_{14}ZnGe_4O_{16}$	LISICON	0.1	300
Ag^+	$RbAg_4I_5$		0.25	25
F^-	PbF_2		5	500
O^{2-}	$(Ca_xZr_{1-x})O_{2-x}$	zirconia	0.05	1000

The conductivity of concentrated hydrochloric acid at 25°C is approximately 1 $\Omega^{-1}cm^{-1}$ which is similar in magnitude to the majority of SEs listed in Table 1-1.

Table 1-1 provides only a small fraction of the SEs currently available; besides many other SEs which are, for example, proton, copper, indium or chloride ion conductors, direct analogues of the ones listed above such as K-BASE (BASE = β-alumina solid electrolyte) or CaF_2 also exist.

The SEs used in this work are K-BASE, Na-BASE, and two lisicon type electrolytes; $Li_{3.5}Ge_{0.5}V_{0.5}O_4$ and $Li_{3.3}P_{0.7}Si_{0.3}O_4$. Stoichiometric lisicons (or γ phases) are

compounds such as Li_3XO_4:X = P, As, V. The crystal structures of stoichiometric γ phases contain an array of oxide ions, which is intermediate between hexagonal close packed and tetragonal packed with the lithium ions distributed over various tetrahedral sites. The Li^+ ion conductivity of these phases can be enhanced by creating solid solutions of the formula $Li_{3+x}(Y_xX_{1-x})O_4$. The substitution mechanism is of the type $X \rightleftharpoons Y + Li$ where examples of Y are Si, Ge or Ti. This leads to the creation of interstitial lithium ions which are responsible for the high conductivity. More emphasis will be placed on the conduction mechanism of lisicons in the following part of this section.

2) Conduction Mechanisms

When they are polarised, the conductivity in solid electrolytes is predominantly ionic but there is often a small electronic contribution [10]. This can generally be regarded as insignificant, however, and the remainder of this section shall deal with proposed models of ionic conductivity of which there are three:

1) *Vacancy mechanism.* An ion moves into an adjacent vacant site and leaves its own vacant (Fig. 1-1a).

2) *Interstitial mechanism.* An interstitial ion jumps into an adjacent empty interstitial site (Fig. 1-1b).

3) *Interstitialcy mechanism.* An interstitial ion causes one of its neighbours to move off its normal site into an adjacent interstitial site and then occupies the vacant lattice site thereby created (Fig. 1-1c).

When solid electrolytes of more complicated structure are being considered the mechanisms are still the same, but it is often useful to consider larger parts of the crystal structure in order to gain a clearer picture of the mechanism. For example the structure of Na-BASE (Fig. 1-2) contains planes of loosely packed sodium and oxygen ions. These sodium containing planes are held 1.13 nm apart by close-packed

spinel blocks (oxygen layers with aluminium ions in octahedral and tetrahedral positions) which extend normal to the c-axis. The spinel blocks above and below the sodium planes are mirror images of each other and are separated by oxygen bridges. The sodium ions can move easily within the loosely packed planes via an interstitialcy mechanism but not through the closely packed spinel blocks.

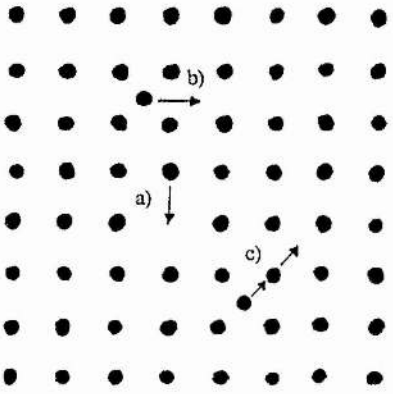

Fig. 1-1. The three types of conduction mechanisms that are possible in a solid lattice. a) Vacancy mechanism. b) Interstitial mechanism. c) Interstitialcy mechanism.

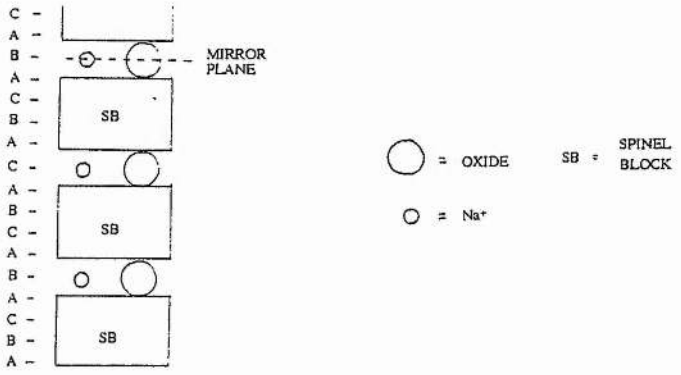

Fig. 1-2. Oxide packing arrangement in Na β-alumina. ABC... represents the oxide layer stacking sequence.

The interstitialcy mechanism also operates during lithium ion conduction in $Li_{3.5}Ge_{0.5}V_{0.5}O_4$. In the parent stoichiometric compound γ-Li_3VO_4, oxide ions are hexagonally close packed with Li^+ and V^{5+} cations filling half the tetrahedral sites which are arranged in face sharing pairs. The VO_4 tetrahedra are isolated from each other and corner share with LiO_4 tetrahedra which are arranged in groups of three edge sharing sites. Fig. 1-3 is a unit cell projection of γ-Li_3VO_4.

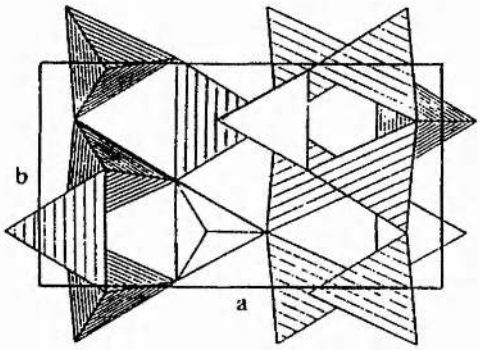

Fig. 1-3. Unit cell projection onto a/b of γ-Li_3VO_4. Open and shaded tetrahedra represent VO_4 and LiO_4 respectively.

On formation of the solid solution, charge compensating Li^+ ions are introduced to octahedral sites. Diffraction data [11] has shown that the interstitial Li^+ ions are located in defect clusters and that an overall picture of the structure includes domains of both the γ-Li_3VO_4 structure and these clusters. In this compound the interstitialcy mechanism involves movement of entire lithium rich clusters into the stoichiometric γ-Li_3VO_4 regions.

1.3 Intercalation Electrodes

Intercalation materials are solids which allow conduction by both electrons and ions. Structurally, intercalation compounds are similar to solid electrolytes in that they contain a connected system of empty lattice positions which allow species capable of fitting into them to move at a high rate. The reversible insertion of guest ions into the

host structure requires the simultaneous accommodation of compensating charges which are either delocalised in a band structure or localised by the redox behaviour of discrete atomic entities.

Examples of intercalation compounds include intercalates of: transition metal oxides (e.g. $Na_{1-x}CoO_2$, $Li_xV_6O_{13}$, $LiMnO_2$, $K_{1+x}Fe_{11}O_{17}$, Na_xWO_3); transition metal dichalcogenides (e.g. $LiTiS_2$) and graphite (e.g. KC_8).

Titanium disulphide was the first intercalation material to be studied in depth because it was found to be a good electronic conductor, light in weight, cheap and environmentally friendly. In 1976 Whittingham [12] showed that Li_xTiS_2 compounds could be formed in an electrochemical cell with lithium as the anode, $LiPF_6$ in propylene carbonate as the electrolyte and a single crystal of TiS_2 as the cathode. The cell emf was found to be 2.5 V and X-ray analysis of the discharge products showed that the reaction proceeded by intercalation of lithium into the TiS_2 lattice (Eq. 1-1) with very little structural modification of the host.

$$xLi^+ + xe^- + TiS_2 \rightleftharpoons Li_xTiS_2 \qquad (1\text{-}1)$$

Starting with a cell containing a fully charged TiS_2 cathode (i.e. $LiTiS_2$) it was found that a plot of cell emf against x in Li_xTiS_2 completely retraced itself upon cell recharge thus proving the system's reversibility (Fig. 1-4).

More recently [13] work involving a study of the TiS_2/1.4 M $LiAsF_6$ in 2-methyl THF interface has shown that the intercalation of Li^+ ions into TiS_2 involves a solvated cation adjacent to the electrode losing part of its solvation sheath and becoming adsorbed, thus forming an adion on the electrode surface. This is accompanied by the injection of an electron into the conduction band of the host. The partially solvated cation then diffuses across the surface of the electrode until it reaches a site at which insertion of the ion can occur, the ion loses the remaining solvent molecules and enters the host lattice.

The intercalation electrodes used in this work are $K_{1+x}Fe_{11}O_{17}$, $Na_{1-x}CoO_2$ and $LiMn_2O_4$. Potassium ferrite is structurally analogous to the β-aluminas and Dudley and Steele [14] have found that the ionic conduction mechanism is also directly comparable. Sodium cobalt oxide has the crystal structure shown in Fig. 1-5 with Na^+ ions sandwiched between two oxygen layers. Ionic conduction in this material proceeds via a vacancy mechanism.

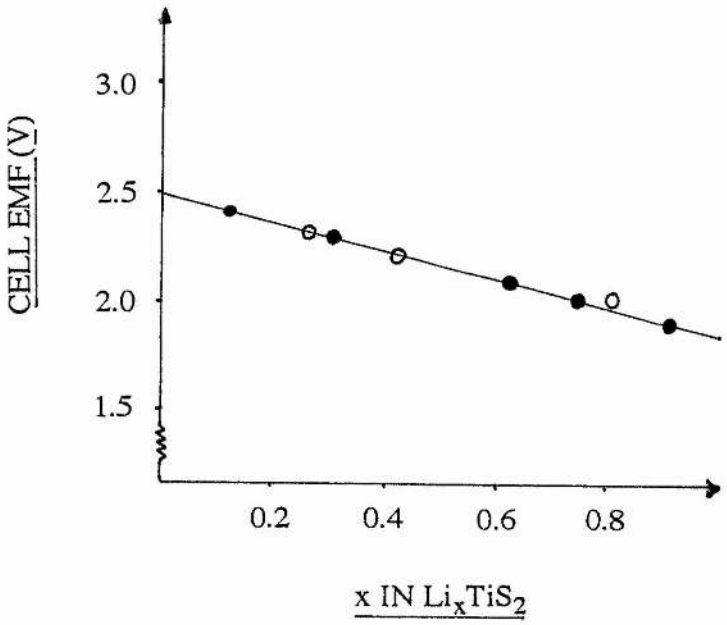

Fig. 1-4. Cell emf of Li/TiS_2 couple. Open-circuit values obtained on discharge of (•) TiS_2 and recharge of (o) $LiTS_2$.

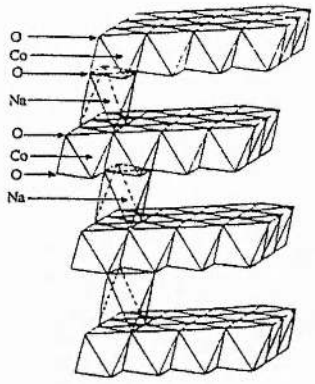

Fig. 1-5. The structure of $Na_{1-x}CoO_2$ used in this work. The sodium ions are located in octahedral sites between adjacent oxide layers. Cobalt ions reside in octahedral sites within the oxide layers.

$LiMn_2O_4$ is another outstanding battery electrode material. It was discovered by Wickham and Croft in 1958 [15] and developed in the early eighties by Goodenough [16]. The structure of $LiMn_2O_4$ is that of a normal spinel with oxide ions forming a cubic close packed array and Mn^{3+} and Mn^{4+} cations occupying half of the octahedral sites. Li^+ ions are found in one eighth of the tetrahedral sites and the framework of the spinel structure's interstitial space provides 3D conduction pathways. The mechanism for ionic conductivity proceeds by an interstitial mechanism with Li^+ ions hopping from the tetrahedral sites to neighbouring vacancies.

Besides the previously mentioned electrochemical means of inserting guest ions into parent structures, intercalation compounds can also be prepared by chemical methods. One method currently gaining in popularity is sol-gel processing [17] where controlled hydrolysis-condensation reactions of molecular precursors gives a colloidal suspension of solid particles (a sol). In turn, the sol particles join together to form a gel which is heated to remove solvent and cause the conversion of the amorphous residue to crystalline material. Traditional high temperature solid state reactions were employed to prepare the intercalation electrodes *and* solid electrolytes used in this

work. This method involves heating a mixture of reactants at an elevated temperature to obtain the product. For example, heating a mixture of Mn_2O_3 and Li_2CO_3 at 850°C results in the synthesis of lithium manganese oxide.

1.4 Existing Applications of Solid State Ionics

The union of solid electrolytes with intercalation electrodes or conventional metal electrodes forms the central part of the solid state ionic device. A recent review in the journal named "Solid State Ionics", by Tillement [18], contains 127 references which deal with SSI devices. The purpose of this section is to summarise the four main applications - namely rechargeable batteries, fuel cells, sensors and electrochromics.

1) Rechargeable Batteries

Rechargeable or secondary batteries are designed to use the chemical energy of a spontaneous redox reaction as a source of electrical energy during discharge. Charging the battery brings about the opposite effect since electrical energy is now being used to bring about a non-spontaneous redox reaction. Intercalation electrodes such as $LiMn_2O_4$ are playing an increasingly important role in battery development.

2) Fuel Cells

Fuel cells are based on the same principles as batteries in that they are designed to create electricity by harnessing a chemical reaction. Unlike batteries, which store their reactants within the cell, these devices receive gaseous or liquid reactants at the electrodes from an external store and vent their reaction products.

Zirconia (ZrO_2) is often used as an electrolyte in fuel cells which generate water from air. In this instance reduction of O_2 can take place on porous electrodes of Ni, Co, Pt, Au, or Ag which are prepared by deposition techniques such as sputtering to optimise their surface areas. O^{2-} ions are then transported through the zirconia until they reach an anode upon which they are oxidised by hydrogen to produce water. The electrons released as a result of this oxidation are used to drive an external load.

3) Sensors

SSI sensors are electrochemical devices that are used to determine the concentrations of particular chemical species which are usually found in gases or liquids. Much of the development so far has been devoted to oxygen sensors which are currently being used to determine the oxygen partial pressure in, for example, automobile exhaust systems, molten steel and food packing.

A typical oxygen sensor consists of a tube of zirconia with one end open and the other closed which contains a reference gas such as air. Both the interior and exterior of the tube are coated with porous electrodes which are connected to a voltmeter. Operating the cell between temperatures of 500 and 1000°C facilitates the transport of O^{2-} ions through the zirconia. Eq. 1-2 relates the oxygen partial pressure of the reference gas, P''_{O2}, and the oxygen partial pressure to be measured, P'_{O2}, to the cell voltage E.

$$E = (RT/4F)\ln(P''_{O2}/P'_{O2}) \qquad (1\text{-}2)$$

4) Electrochromics

An electrochromic device is able to change its optical properties in a reversible and persistent way under the action of an electrical impulse. These devices use intercalation electrodes (e.g. Li_xWO_3) for which, the optical transmittance can be reversibly altered by extraction or injection of guest ions and electrons.

Electrochromic SSI devices have numerous potential applications in technology - one example being the smart window which darkens when exposed to sunlight.

1.5 A New Application of Solid State Ionics

Having now mentioned some of the SSI materials and their established applications our attention turns towards a new SSI device which this thesis deals with and that intends to further the development of semiconductor manufacture.

In 1981 Davies and others [19] reported on the use of a solid state electrochemical source of sulphur vapour which was used to dope GaAs in an MBE (molecular beam epitaxy) machine. The MBE process is described in section 1.7. Conventional MBE involves heating stainless steel cylinders containing elements comprising the semiconductor to a temperature that causes their evaporation and the subsequent generation of beams which are directed to a substrate upon which epitaxial growth of the semiconductor takes place. The reason why it was decided to adopt this new method was to overcome difficulties associated with the volatility of sulphur. MBE is an ultrahigh vacuum technique and the apparatus has to be cleaned prior to any semiconductor growth by baking it at an elevated temperature. Elements such as sulphur, iodine and alkali metals cannot withstand these temperatures and would evaporate from the cylinders thus causing contamination of the interior of the growth chamber before any semiconductor growth. Solid state electrochemical cells, however, do not have this problem. The sulphur cell is shown in Fig. 1-6 and consists of two electrodes: one silver, the other a Ag_2S intercalation compound, both in contact with a AgI solid electrolyte. By polarising this cell, Ag^+ ions are removed from the Ag_2S which results in its decomposition and the subsequent release of sulphur vapour. This set up had previously been described by Rickert [20] as a means of gaining the following information: the chemical potential of sulphur in Ag_2S; the chemical potential of sulphur in the gas phase; the partial pressures of the various types of sulphur molecules and the activity of sulphur. It was also used by Rickert to investigate the transfer of silver across the phase boundary $Ag_{(s)}/Ag_2S$ [21].

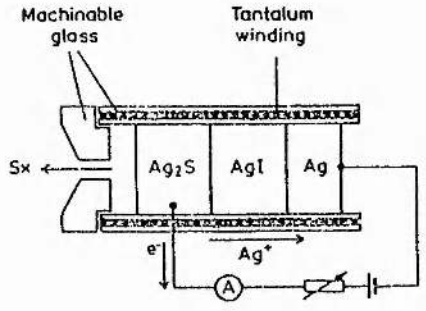

Fig. 1-6 Solid state electrochemical source of sulphur.

Besides extending this idea to the generation of *Se vapour* in an MBE machine with an analogous source (Ag_2Se instead of Ag_2S), Andrews *et al.* [22] also demonstrated that sources of this type were more controllable than conventional sources of gas used in MBE since they were found to have very rapid responses to changing EMFs (~1 sec.). This was much faster than conventional sources (typically 60s) and since many semiconductor devices require very abrupt transitions from highly to lightly doped material this was viewed as an important technological advance.

More recently Cavenett and co-workers [23] have shown that the sulphur source can also be used to grow the alloy ZnS_xSe_{1-x}.

In 1991 Cavenett *et al.* [24] generated iodine in an MBE machine (in order to dope ZnSe) by an electrochemical method which was slightly different from that outlined above. This source is illustrated in Fig 1-7. The only difference between it and the sulphur source in Fig. 1-6 is the replacement of the Ag_2S intercalation electrode with a platinum gauze. On heating the cell to above 146°C the Ag^+ ions become mobile and application of an external voltage across the platinum gauze and silver electrodes results in the passage of Ag^+ to the cathode with charge neutrality being maintained by the generation of iodine at the anode as a result of the half-cell reaction:

$2I^- \rightarrow I_2 + 2e.$

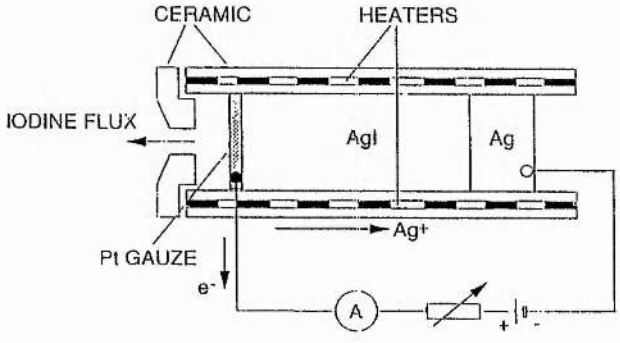

Fig. 1-7. Solid state electrochemical source of iodine.

Approximately one year later Bruce *et al.* [25] adopted a similar method for producing potassium vapour, again for doping ZnSe. In order to achieve this a potassium β-

alumina solid electrolyte was attached to a potassium ferrite intercalation electrode and a platinum gauze pressed onto the K-BASE surface (Fig. 1-8).

Polarising this source as shown causes potassium ions to move from the intercalation electrode, through the solid electrolyte and onto the gauze where they are reduced to potassium atoms by electrons which travel around external circuitry as a result of a charge compensating iron oxidation ($Fe^{2+} \rightleftharpoons Fe^{3+} + e$) occurring within the potassium ferrite. The source is operated at temperatures exceeding 180°C to ensure that the produced potassium vaporises.

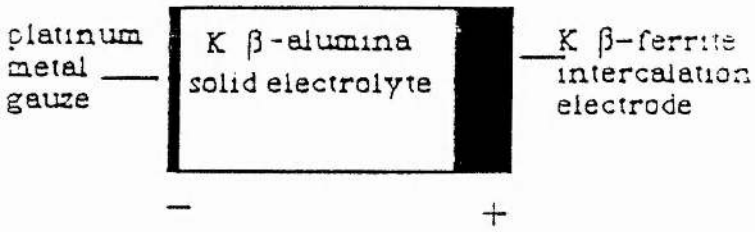

Fig. 1-8. Solid state electrochemical source of potassium.

Chapter 4 gives a detailed account of the procedure used to prepare this source whilst chapter 6 provides results of the MBE experiment.

Besides addressing the important problems associated with manufacturing this source, extending the idea to the generation of lithium and sodium vapours and using both potassium and lithium sources as precursors for semiconductor growth, this work also focuses on the solid electrolyte/metal gauze interface upon which generation of the alkali metal vapour takes place and attempts to arrive at conclusions concerning the electrochemical mechanisms behind alkali metal production by employing electroanalytical measurements and in-situ mass spectrometry. Most of this aspect of the research (including all of the in-situ mass spectrometry) deals with the Na-BASE/stainless steel/vacuum interface of the sodium source for reasons given

in section 5-1. It is the purpose of the remainder of this section to: outline an older system which is similar in principle to the sodium source; to mention other studies of the Na-BASE/electrode interface; and give some background concerning electrochemical mass spectrometry (EMS).

Alkali Metal Thermoelectric Converters (AMTECs) are devices which can convert heat into electrical energy. The principle of operation was first outlined in the patent literature by Kummer and Weber in 1968 [26] and to this day, extensive development is being carried out world-wide in order to maximise its efficiency. The major incentive behind this work is the minimisation of energy losses in spacecraft since AMTECs have the ability to use high temperature combustion and nuclear heat sources which are often integral components of the vehicle itself.

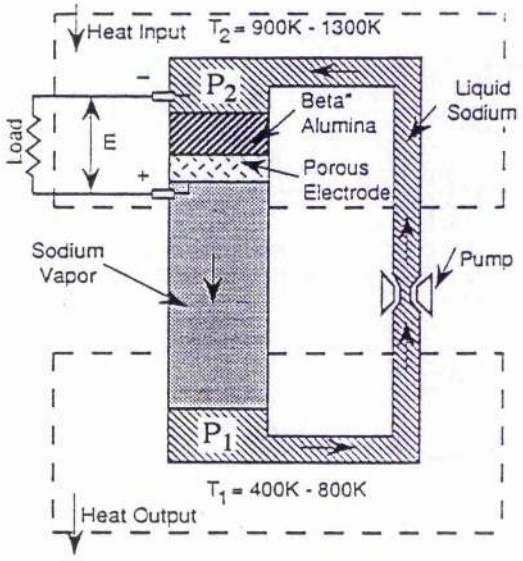

Fig. 1-9. Schematic diagram of the alkali metal thermoelectric converter (AMTEC). Taken from reference [27].

The diagram in Fig. 1-9 explains how the AMTEC operates. A closed container is divided into two regions by a pump and a septum consisting of a solid electrolyte membrane (sodium β-alumina) and porous electrode. The generator contains a working fluid (sodium), whose pressure P_2, in the upper region is greater than P_1,

input raises the incoming liquid sodium to temperature T_2 (600-1000°C). Sodium then migrates through the solid electrolyte as Na^+ ions ($Na \rightleftharpoons Na^+ + e$) as a result of the pressure differential (P_2-P_1) across the solid electrolyte. Electrons left behind leave the P_2 region via the negative electrode. On passing through the Na-BASE, sodium ions are recombined with electrons at the electrode-electrolyte interface, the electrons meanwhile having passed through the electrical load. Neutral sodium evaporates from the porous electrode at pressure P_1 and temperature T_2 passing in the gas phase to a condenser at temperature T_1 (100-500°C). Condensed liquid sodium is returned to the high pressure region by the pump, thus completing the cycle.

The major barrier to application of this device is identification of an electrode which can maintain optimum power densities for operation times of >10000 hours. So far the most widely used cathode material has been a columnar, porous, magnetron-sputtered molybdenum film. This has allowed the AMTEC to operate at an energy conversion efficiency of 19% and at power densities near 1.0 W/cm^2. However, there is a problem associated with the use of porous Mo electrodes in AMTECS due to the evaporation of sodium ion transport enhancing sodium molybdate, Na_2MoO_4, which is formed within the electrode as the cell operates [28]. This is thought to cause degradation of device performance.

More recently it has been suggested that the replacement of sodium and Na-BASE ceramic with another metal and solid conductor of the metals' cations in an AMTEC may be considered as a potential means of attaining good performance characteristics under different operating conditions. This has prompted research into a system based on potassium and a recent paper in Solid State Ionics by Williams *et al* of the Jet Propulsion Laboratory at California Institute of Technology [29], which deals with high temperature measurements of the conductivity of K-BASE, concludes by stating that its conductivity is high enough to allow the use of potassium as a working fluid in AMTECs operating between temperatures of 800K and 1100K.

Experiments which are geared towards improving the performance of AMTECs by testing different materials are also supplemented by research which is concerned with

facilitating performance optimisation by evaluating contributions such as contact/lead resistance, solid electrolyte resistance, and kinetic and mass-transport parameters of the porous electrode to the cell's internal impedance. This has led to the establishment of an equivalent circuit which can be used to accurately mimic the frequency response of an AMTEC [30, 31].

This is not the first time that interfacial aspects of electrode/Na-BASE have been studied. Besides research dealing with the AMTEC, work by Armstrong *et al.* [32, 33] in the early seventies, which focused primarily on the frequency response of the interphase, enabled them to deduce a variety of equivalent circuits which represented interphase models that could explain some previous experimental observations on a variety of metal/solid electrolyte interphases including Na-BASE/sodium. More recently [34], Butchereit *et al.* have paid close attention to the effects of Na-BASE surface roughness, types of electrode and the influence of water vapour on the electrical response of this technologically important interface.

The possibility of measuring electrochemical reaction products via mass spectrometry was first suggested by Gadde and Bruckenstein in the early seventies [35]. In this work a mass spectrometer was used to measure the rate of electrochemical production of oxygen from a 0.1 M solution of $HClO_4$ at a porous electrode. In order to do this the peak height of the mass-32 response was related to the number of moles of oxygen and measured as a function of time and current.

Over the past ten years, electrochemical mass spectrometry (EMS) has been used as a means of investigating the oxidation of methanol on noble metals such as platinum or palladium [36]. This is a reaction of technological importance due to its significance in the electrocatalysis of fuel-cell reactions.

The object of this work is to demonstrate the feasibility of obtaining an in-situ analysis of the production of sodium from the source by mass spectroscopy.

The remainder of this introduction deals with background concerning semiconductor properties and epitaxial growth technology which is essentially crystal growth on a substrate that dictates the lattice structure of the grown layer.

1.6 Intrinsic and Extrinsic Semiconductors

Semiconductors are electronic conductors. They can be amorphous, polycrystalline, single-crystal, elemental or compound. This section considers single-crystal semiconductors since the majority of semiconductor devices are based on these due to their superior electrical characteristics.

1) Intrinsic

These materials have inherent semiconducting properties with the number of electrons in the conduction band being governed by the magnitude of the band gap and also temperature. At room temperature group IV elements such as silicon and germanium are examples of intrinsic semiconductors as is the inorganic compound GaAs which is isoelectronic with group IV elements as far as the number of electrons in the valence shells are concerned.

2) Extrinsic

Apart from thermal generation, charge carriers in semiconductors can also be created by adding certain types of impurity atoms. For silicon, the impurities of most interest are the elements of groups III and V. This addition is known as *doping*, and semiconductors containing added impurities are known as *doped* semiconductors with semiconducting properties which are extrinsic in nature.

a. n-type Semiconductivity

If a very small amount of a group V element (e.g. As or P) is added to a pure crystal of silicon it is found that the impurities occupy lattice sites that are normally occupied

by Si atoms. These dopants are called substitutional impurities. Now, for example, an As atom has five valence electrons and four of these make covalent bonds with the Si atoms; the fifth electron, however, cannot be accommodated in the bonding arrangement and is bound to the impurity atom by weak electrostatic forces. The magnitude of thermal energy k_BT at room temperature is 0.025 eV which is comparable to the magnitude of energy required to ionise the extra electron attached to the impurity atom. Thus, at ordinary temperatures, the thermal vibrations of the lattice atoms will impart enough energy to the electron to shake it free and if a large number of donor atoms is randomly distributed in the semiconductor, the electron concentration rises above the intrinsic concentration. Such a semiconductor is known as an n-type semiconductor and since the arsenic atoms donate free electrons to the crystal they are known as donor atoms. Since the electrons can be set free by supplying an energy which is only about tens of meV, the energy level must be situated very near the bottom of the conduction band edge (Fig. 1-10).

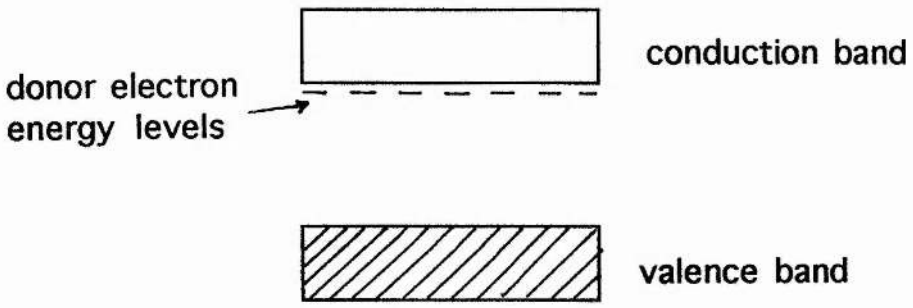

Fig. 1-10. Energy band diagram of an n-type semiconductor showing donor levels.

b. p-type Semiconductivity

When silicon is doped with an element of group III (e.g. B or Al) the valence electrons of the impurity complete three of the covalent bonds, leaving one bond vacant which accepts an electron from a neighbouring atom and creates a hole in the crystal. At 0°K the hole remains bound to the impurity atom but breaks away from it

at higher temperatures, whereupon it wanders freely in the crystal. An impurity atom that contributes a hole is called an acceptor atom because it accepts a bound electron from the covalent bond. Semiconductors doped with acceptor atoms are deemed p-type.

The energy band diagram for a p-type semiconductor is shown in Fig. 1-11. The acceptor levels lie in the forbidden gap close to the valence band edge.

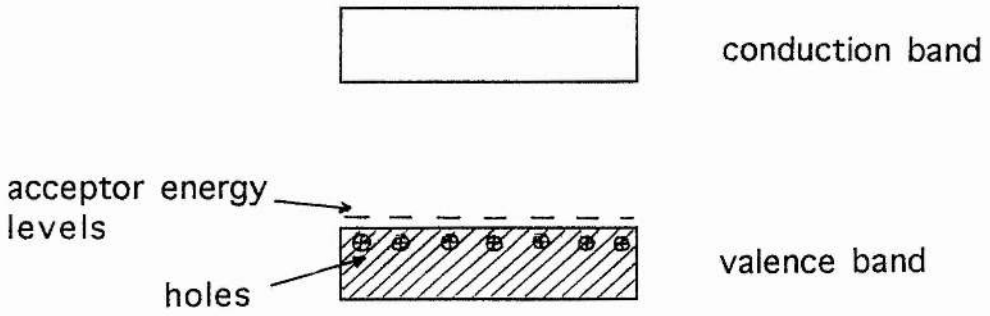

Fig. 1-11. Energy band diagram of a p-type semiconductor showing acceptor levels.

c. Compound Semiconductors

Since this research was initiated by the interest in obtaining p-type ZnSe - a compound semiconductor with useful optoelectronic properties - it is worthwhile to show that the same principles mentioned above also apply to these materials.

So far the only two compound semiconductors which have been mentioned are GaAs and ZnSe. These are classified as III-V and II-VI semiconductors respectively. In III-Vs, group II elements can replace the trivalent atoms and act as acceptors whilst group VI elements can replace the pentavalent atoms and act as donors. Introduction of a group IV element can result in either a p-type or an n-type semiconductor depending on which sublattice is doped. Because of this trait, atoms of group IV are called *amphoteric* impurities.

In II-VI semiconductors, group III elements replace the group II elements and act as donors. Elements of group VII (Cl, Br, and I) also act as donors by replacing group

VI elements. Similarly, a p-type semiconductor can be obtained by doping either with group I or with group V elements.

1.7 Semiconductor Growth by Epitaxy

It should be noted that besides epitaxy, three other methods are currently being used for semiconductor processing. These are: alloying; solid-state diffusion; and ion implantation.

1) Liquid Phase Epitaxy

This technique is based on the melting point depression of a semiconductor material when it is mixed with a second element - hence it can be used to grow a crystal from solution at the temperature of the mixture. For example, the melting point of GaAs is 1238°C. However, when GaAs is mixed with Ga metal, the mixture has a considerably lower melting point. Thus, to grow GaAs, a Ga solution containing GaAs and any desired dopants is placed onto a GaAs single crystal substrate which is kept in a graphite boat. The boat is kept at about 850°C in a furnace. When the furnace is cooled slowly, the GaAs crystallises from the solution onto the substrate.

2) Vapour Phase Epitaxy

a. Chemical Vapour Deposition (CVD)

Epitaxial growth of silicon by CVD is illustrated in Fig. 1-12.

Liquid $SiCl_4$ is kept in a bubbler with a stream of H_2 gas passed through it. The $SiCl_4$ + H_2 vapour is mixed with more H_2 near the mouth of the quartz reactor. Silicon wafers are placed on a graphite base inside the reactor and heated to a temperature in excess of 1100°C. The following reaction occurs on the wafer surface:

$$SiCl_4 + 2H_2 \rightleftharpoons Si + 4HCl$$

The Si is deposited on the silicon substrate, and the HCl gas leaves through a suitable vent.

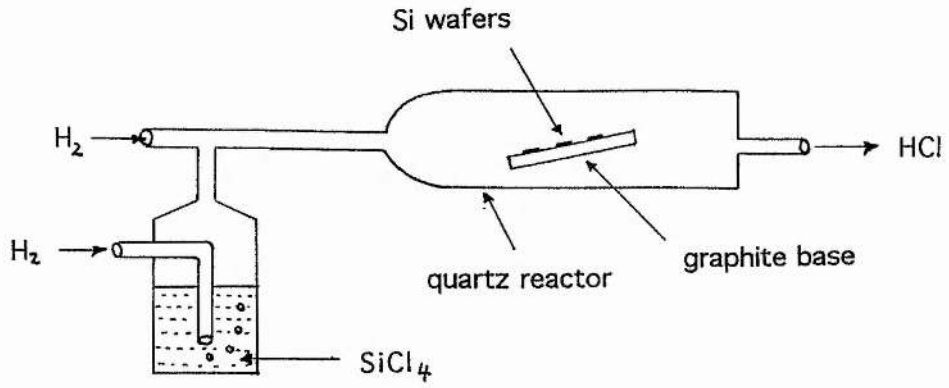

Fig. 1-12. Epitaxial growth of silicon by CVD.

In order to grow doped Si with a desired resistivity and conductivity type, gases containing dopant atoms are introduced to the gas system. PH_3, AsH_3 and SbH_3 are used for n-type doping, whereas diborane (B_2H_6) is used for p-type doping.

Since the early eighties metal organic vapour phase epitaxy (MOVPE) or metal organic chemical vapour deposition (MOCVD) has rapidly developed into one of the major methods for the preparation of optoelectronic devices. This technique is essentially the same as that outlined for silicon - the only difference being the important role played by organometallic precursors. Examples of its current use as a viable means of obtaining ZnSe and related alloys can be found in references [37] and [38] where dimethylzinc (DMZ) and diethyl selenide (DESe) are the main precursors. Since its advent, the MOVPE route has been responsible for much research into novel precursors capable of improving electronic properties of the semiconductors which they react to form [39].

b. Microwave Enhanced Chemical Vapour Deposition (MWECVD) for Synthesising Diamond

More than 98% of present day electronic semiconductor devices such as rectifiers, switches and amplifiers are silicon based. Silicon integrated circuits, however, do not function conveniently at high temperatures. Between 100 and 500 degrees Celsius many of silicon's bonding electrons become mobile, making it impossible to control conductivity. Unlike silicon, diamond can work better at higher temperatures. This makes it an ideal candidate for integrated circuits which must operate within thermally hostile environments such as spaceships. A problem associated with the development of these diamond based devices (namely an efficient means of obtaining n-type diamond) is addressed in chapter 6.

Today there are several CVD methods for preparing diamond films [40]. The MWECVD technique which is used in this work is illustrated in Fig. 1-13.

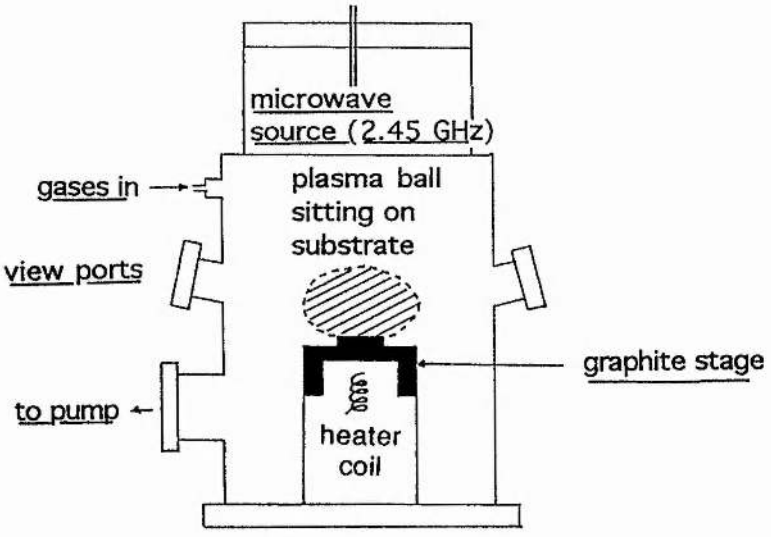

Fig. 1-13. Schematic diagram of MWECVD apparatus.

During this process carbon containing carrier gases e.g. methane, acetone, carbon monoxide, or adamantane are decomposed by a microwave plasma discharge (Eq. 1-3).

$$C_xR_{y\,(gas)} \rightleftharpoons C_{(solid)} + yR_{(gas)} \qquad (1\text{-}3)$$

In order to suppress the growth of graphite an etchant such as atomic hydrogen or oxygen is introduced to the reaction mixture. This is illustrated by the additional reaction steps in Eqs. 1-4 and 1-5 where E^* represents the etchant.

$$nC_{(solid\ graphite)} + mE^* \rightleftharpoons C_nE_{m(gas)} \qquad (1\text{-}4)$$

$$nC_{(solid\ diamond)} + mE^* \rightleftharpoons C_nE_{m(gas)} \qquad (1\text{-}5)$$

The rate for graphite etching has to be higher than for diamond in order to promote diamond growth. During etching the etchant reacts with any graphite like precursors to form molecular structures more closely resembling the structure of diamond.

Similar to CVD, MWECVD also involves the use of a substrate which forces the diamond to grow with a fixed crystallographic orientation. Crystals of nickel, copper, silicon carbide, beryllium oxide and boron nitride have suitable lattice spacings and have been used as templates for growing diamond crystals.

It has been predicted by several authors [41, 42] that lithium should be a suitable dopant for effective production of n-type diamond. This work involves the preparation of a solid state electrochemical cell capable of generating lithium vapour with the aim being to show that it can be interfaced with a MWECVD machine during attempts at preparing n-type diamond.

c. Molecular Beam Epitaxy (MBE)

Reduced to its essentials, a system for MBE consists of an ultrahigh vacuum system containing sources for beams of elements which constitute the semiconductor. These beams impinge upon a heated single crystal substrate such as GaAs where epitaxial growth takes place. Figure 1-14 illustrates this process for the growth of GaAs.

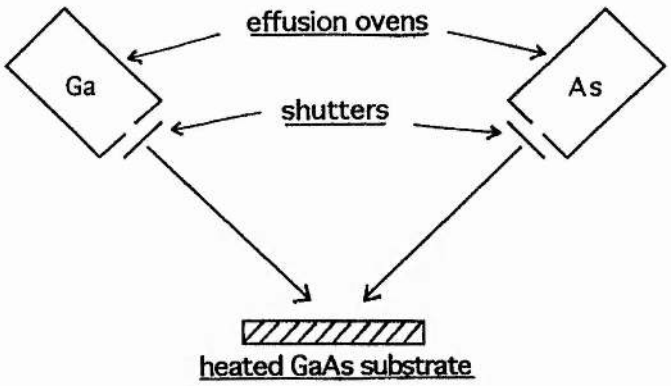

Fig. 1-14. A representation of the molecular beam epitaxy (MBE) process.

The beam sources are usually cylindrical stainless steel containers which hold the elements and are heated to create the beams. The container, or effusion oven as it is usually called, has an orifice that faces the substrate wafer. A controllable shutter is placed in front of the orifice in order to allow the beam to be shut off. The beam intensity may be altered by changing the oven temperature; a facility which also allows dopant profiles to be varied within the semiconductor.

This method is not only limited to the use of pure elements such as Ga and As; compounds such as $ZnCl_2$ can also be placed inside the effusion oven. When this is heated above 130°C, chlorine gas is released [43].

MBE experiments with *alkali metals* have been performed for a number of years now, and several new techniques for generating them (including our own) have been developed in order to surmount problems associated with their high volatility and reactivity. Reference [44] outlines the use of a lithium dispenser which consisted of a metallic strip rolled around a powder containing a mixture of Li_2CrO_4 and reducing agents. This set up generated lithium from the salt when an electric current was passed through it. A sodium dispenser was recently used by Cheng *et al.* in an attempt at creating p-type ZnSe [43] - this experiment failed, however, for reasons thought to be due to the release of additional impurities from the dispenser.

Materials and Equipment

2.1 Synthesis of Materials for the Potassium Source.

Preparation of $K_{1+x}Fe_{11}O_{17}$.

K_2CO_3 (Fisons) and Fe_2O_3 (Johnson Matthey) were ground together for 10 minutes in air in a 1:5 mole ratio respectively. The powder was placed in a gold crucible, calcined in an electric muffle furnace at 650°C for 2 hours in order to decompose the carbonate, transferred to a flowing oxygen tube furnace and left for 24 hours at 950°C. The reacted material was subsequently quenched in air to room temperature.

Preparation of $KAl_{11}O_{17+x/2}$.

K_2CO_3 and Al_2O_3 (Fluka) were reacted together by the same method as outlined above except that the mixture was placed in a platinum crucible and solid state reaction was carried out in air at 1200°C in a muffle furnace.

2.2 Synthesis of Materials for the Sodium Sources.

Preparation of $Na_{1+x}Fe_{11}O_{17}$.

Exactly the same method was adopted as for potassium ferrite except that Na_2CO_3 (Fisons) was used instead of K_2CO_3.

Preparation of $Na_{1-x}CoO_2$.

A 3:2 molar ratio of Na_2O_2 (BDH): Co_3O_4 was mixed together for 10 minutes in an MBRAUN argon filled glove box and transferred to a gold boat which was placed inside a silica tube which was fitted with taps that enabled the reaction to be carried out under a constant flow of oxygen. This was then taken from the glove box and placed inside a tube furnace which was raised in temperature by 4°C/min until it reached 500°C. The mixture was left at this temperature for 2 days. After this period the temperature was lowered to 25°C, again at a rate of 4°C/min.

Preparation of $NaAl_{11}O_{17+x/2}$.

Exactly the same procedure for potassium aluminate was adopted except that Na_2CO_3 was used instead of K_2CO_3.

2.3 Synthesis of Materials for the Lithium Sources.

Preparation of $LiMn_2O_4$.

Li_2CO_3 (BDH) and Mn_2O_3 (Johnson Matthey), in a molar ratio of 1:2 respectively, were ground up for 10 minutes as a slurry in ethanol and evaporated to dryness. Reaction was carried out in a gold crucible which was placed in a muffle furnace, initially at 650°C for 16 hours to decompose the carbonate followed by 24 hours at 850°C, before quenching in air to room temperature.

Preparation of $Li_{3.5}Ge_{0.5}V_{0.5}O_4$.

Lithium germanium vanadate was prepared by the reaction of appropriate quantities of Li_2CO_3, GeO_2 (Aldrich) and V_2O_5. The reactants were initially ground up for 10 minutes as a slurry in ethanol and evaporated to dryness. Reaction was carried out in a gold crucible which was placed in a muffle furnace, initially at 650°C for 18 hours followed by 6 hours at 850°C, before quenching in air to room temperature.

Preparation of $Li_{3.75}Si_{0.75}P_{0.25}O_4$.

Lithium phosphosilicate was prepared by mixing $NH_4H_2PO_4$ (Aldrich 1.61g.), $LiOH.H_2O$ (Aldrich 2.77g.) and SiO_2 (Aldrich 0.38g.) in acetone for 10 minutes. The dried mixture was then placed in a platinum crucible which was heated to 1000°C in a tube furnace and left at this temperature for 16 hours before quenching in air to room temperature.

2.4 Equipment for Initial Tests on the Sources

Prior to any use of the sources during in-situ mass spectrometry, electrochemical measurements or semiconductor growth, initial tests were carried out to ensure that they were capable of producing beams of the desired elements.

1) X-ray Diffraction Equipment

Throughout this project a combination of the following two X-ray diffractometers were used to check that each of the previously mentioned materials held correct crystal structures:

1) Philips PW 1349

2) Stoe STADI/P

A description of the X-ray powder diffraction experiment is included in the following chapter.

2) Laser Ionisation Mass Analysis (LIMA) Equipment

This technique [45] was used to find out what elements the sources had produced after each experiment. It essentially involved ablating a small (~0.1 mm^2) area of a stainless steel disk, which had previously been exposed to vapour from each source (see Fig. 4-7), with a laser and analysing the contents of the resulting plume with a time of flight mass spectrometer. The instrument used was constructed by Cambridge Mass Spectrometry Ltd. and is represented by Fig. 2-1.

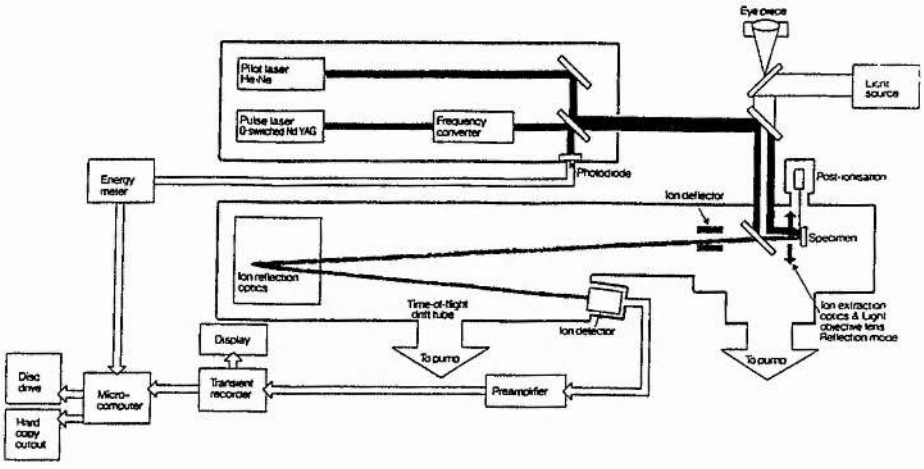

Fig. 2-1. Schematic diagram of the LIMA spectrometer.

The disks were irradiated with 4-5 ns pulses from a Nd:YAG (Spectra-Physics DCR-11) laser at 266 nm. Positive or negative ions were extracted by applying an appropriately biased voltage of 3 kV. Free expansion of the plume occurred in the space between the sample and the extraction plates. The base pressure in the chamber was 10^{-8} torr. The diameter of the focused beam was of the order of two microns and could be increased to ca. 10 microns by moving the sample on a precision translation stage without changing the focusing optics. Ion currents were measured on a LeCroy 9400 digitiser before being sent to a HP series 9000 microcomputer for further data processing.

2.5 Equipment for Electroanalytical Measurements and In-situ Mass Spectrometry

In order to characterize the electrochemical mechanisms responsible for production of the beams it was necessary to construct the following apparatus.

1) Three Electrode Cell and Cell Holder

Figure 2-2 shows what the source looked like whilst electroanalytical measurements were performed.

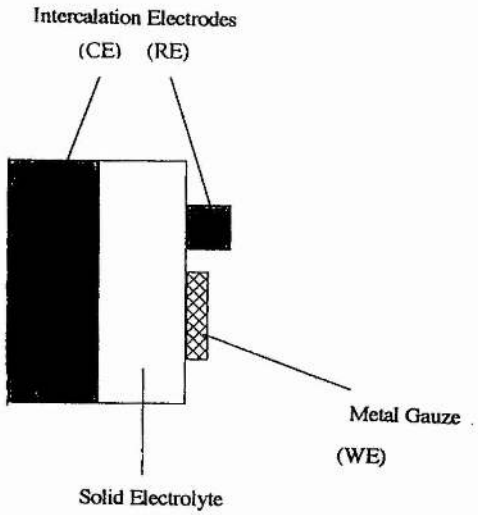

Fig. 2-2. Three electrode cell for carrying out electrochemical measurements.

The stainless steel gauze cathode is known as the working electrode (WE), since this where the electrode processes of interest occur, whilst the intercalation material which supplies the current is deemed the counter electrode (CE). In many studies of electrode processes a third electrode called a reference electrode (RE) is positioned near the working electrode. This enables the working electrode to be isolated by cancelling any electrical response which would occur at the CE/electrolyte interface

and also removes the majority of bulk iR drop due to the electrolyte itself. In this work a 3 mm diameter Specac die was used to compact enough of the intercalation material to form a pellet of ~1-2 mm in length which was used as the RE. To improve the pellet's mechanical strength it was sintered under the same conditions as its corresponding cell. These conditions are described in chapter 4.

2) UHV Apparatus

In order to make measurements in ultrahigh vacuum, a macor ceramic cell holder which contained the three terminal arrangement was placed inside a cylindrical stainless steel heating block capable of maintaining the cell at temperatures of up to 350°C. This was mounted on a stainless steel flange which was fitted with: three electrode contacts for electrochemical measurements; a power supply for the heaters and two thermocouple plugs - one for the heating block and one for the cell. The flange was bolted onto an UHV chamber which was pumped by an Edwards E04 oil vapour diffusion pump backed by an Edwards E2M8 rotary pump. Pressures within the chamber could be taken from 10^{-3} mbar to 10^{-8} mbar by switching the diffusion pump off or on respectively. The chamber was large enough to accommodate the head of a quadrupole mass spectrometer which was used to gain an in-situ analysis of the products of the cell reaction and is described below.

Figure 2-3 is a schematic representation of this set up whilst Fig. 2-4 shows it pictorially.

3) Electrochemical Equipment

Three different electroanalytical measurements were made on the sources throughout this work. The following instruments were used for each technique.

Cyclic Voltammetry

A Schlumberger (Solartron) 1286 potentiostat was used to control a Yokogawa 3025 X-Y chart recorder.

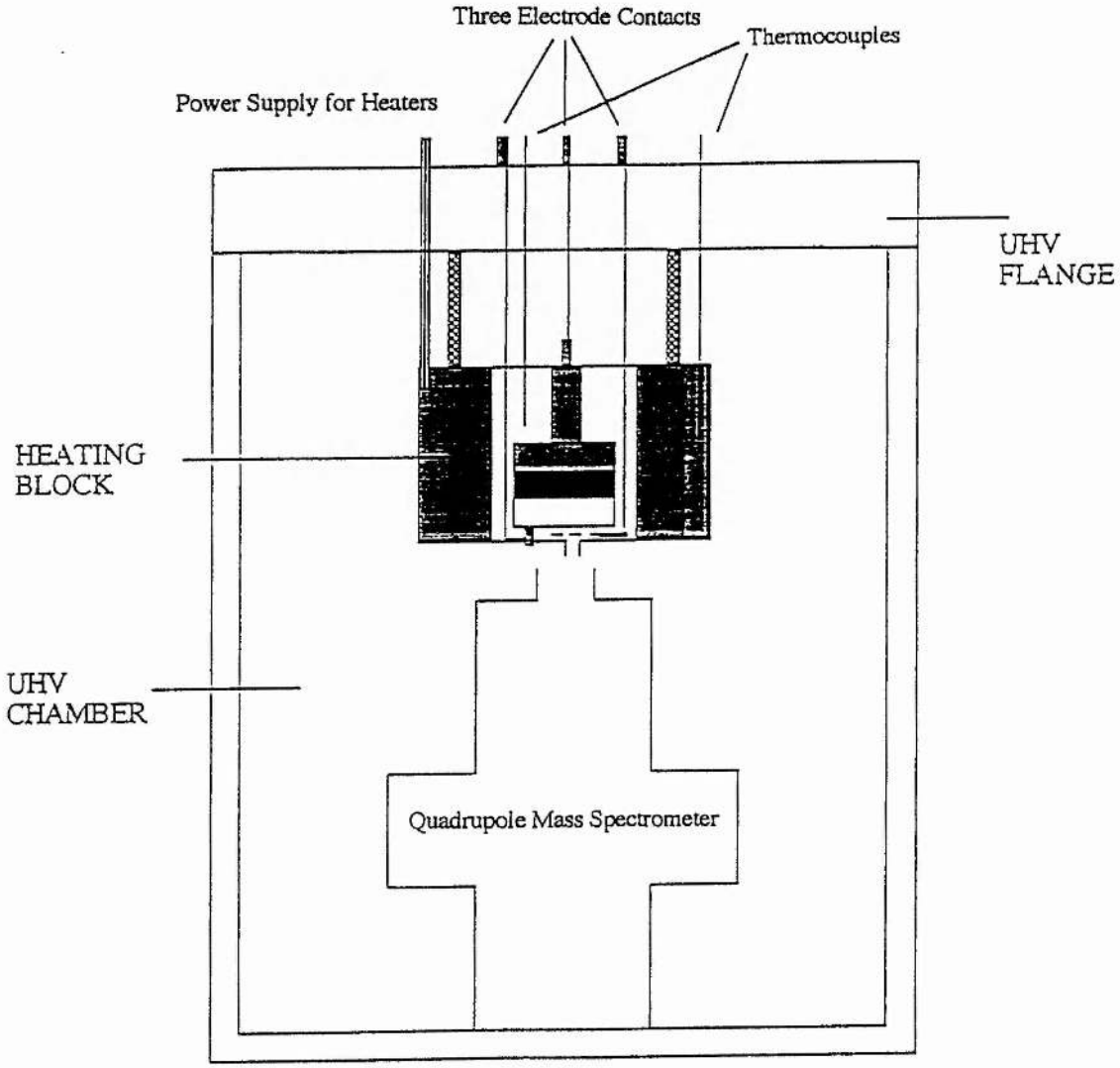

Fig. 2-3. UHV apparatus.

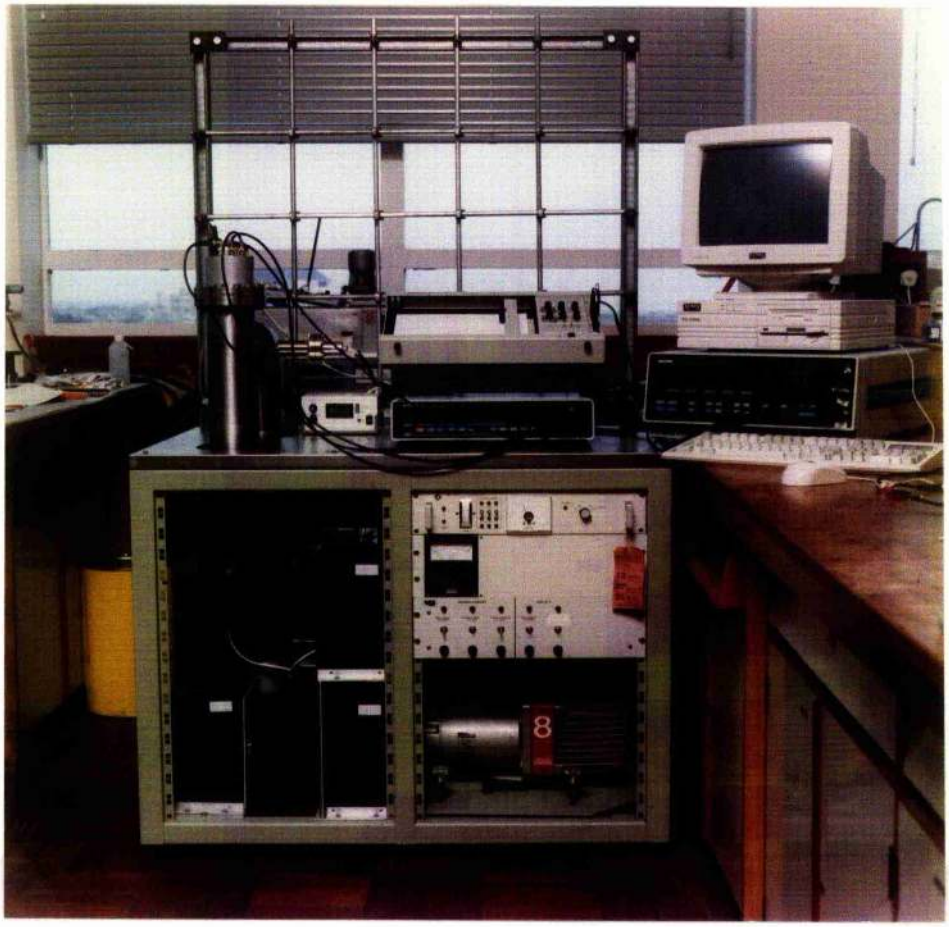

Fig. 2-4. The set-up that was used for electrochemical measurements. The UHV chamber shown in Fig. 2-3 is situated at the top left hand side of the photograph.

Chronoamperometry

A Schlumberger (Solartron) 1286 potentiostat was used to control a JJ Instruments CR 450 Y-t chart recorder.

AC Impedance

The potentiostat was connected to a Schlumberger (Solartron) 1255 frequency response analyser. An ac perturbation of 50 mV was applied to the sources over a variety of frequency ranges and data were collected and processed by a Zenith microcomputer.

4) Quadrupole Mass Spectrometer

This was originally a triple quadrupole mass spectrometer used to study ion-molecule reactions [46]. In order to render the instrument suitable for simply analysing the products of the cell reaction, two of the quadrupole rod sections were removed and a new ioniser, designed to accept a molecular beam axially with respect to the quadrupole axis, was attached to the quadrupole section.

The resulting mass analyser head is illustrated in Fig. 2-5 and consists of three main regions: the ion source; the quadrupole rods; and the detector.

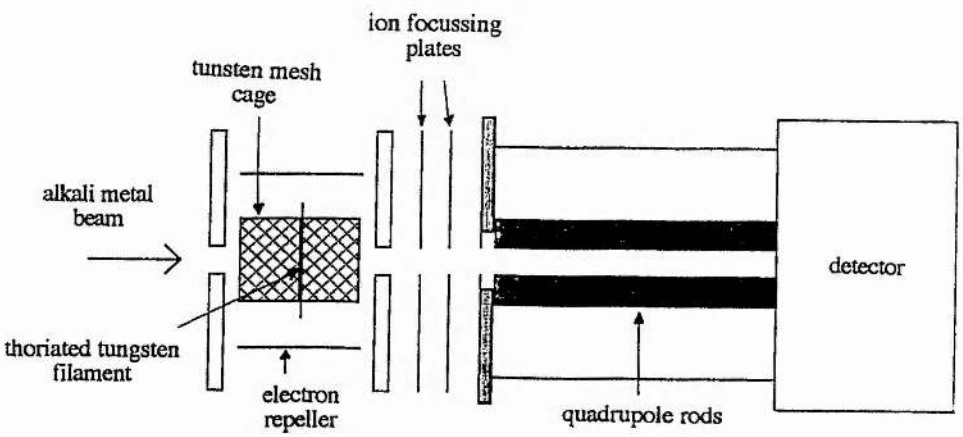

Fig. 2-5. Schematic diagram of the quadrupole mass spectrometer.

The ioniser is a modification of a design by Professor J. H. Lech of the Department of Electrical Engineering and Electronics at the University of Liverpool, and is described in the Ph. D. thesis of A. E. Holme (1972) entitled "The Quadrupole Mass Spectrometer". Ions formed in the source are accelerated and focused into the quadrupole section. Filtering of the ion beam results from the fact that only those ions within a specific range of mass-to-charge ratios are permitted to pass through the filter. This range is determined from values of the DC and RF (radio frequency) voltages which are applied to the poles of the quadrupole section [47]. Ions which are able to pass through the filter are collected by the ion detector.

The ion abundance, as a function of atomic mass, was initially observed on a Telequipment D1010 oscilloscope then transferred to a Bryans 28000 x-y chart recorder.

2.6 Equipment for Semiconductor Growth

1) Potassium Doped ZnSe

a. MBE Machine

Figure 2-6 is a schematic diagram of the VG Semicon MB288 kit which was used to grow layers of ZnSe. Conventional effusion cells were used for producing Zn and Se whilst the potassium cell was placed in a cell holder fitted with electrode contacts. This cell holder is illustrated in Fig. 6-1.

b. Photoluminescence Spectroscopy

Data were collected on a PL6100 Fourier Transform Photoluminescence (PL) Spectrometer.

c. Capacitance - Voltage Profiling

A Bio-Rad PN4200 capacitance - voltage (CV) profiler was used to obtain the data.

d. Secondary Ion Mass Spectrometer

A DEKTAK profilometer situated at the Defence Research Agency in Malvern was used to obtain these results.

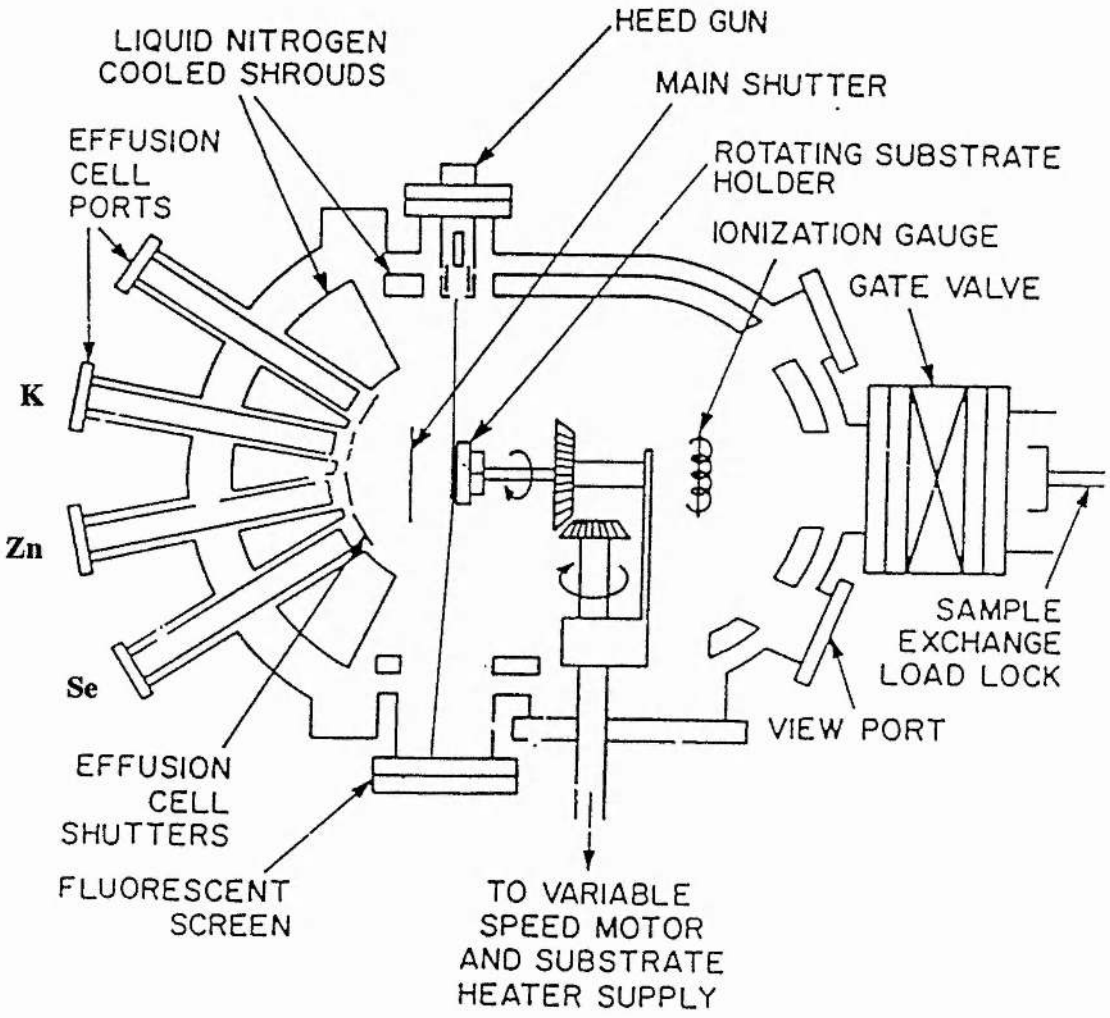

Fig. 2-6. Schematic diagram of the molecular beam epitaxy (MBE) apparatus.

2) Lithium Doped Diamond

a. MWECVD Machine

This is illustrated in Fig. 2-7 and like the MBE machine is based on metal gasket UHV technology. The substrate heater (shown more clearly in Fig. 1-13) is fully encapsulated in molybdenum and stainless steel and the plasma is generated in the spherical multi-port growth chamber (3) with microwave radiation at a frequency of 2.45 GHz. The same cell holder as shown in Fig. 6-1 was used to contain the lithium source. This set-up was attached to a loadlock situated to the left of the growth chamber. Further details about this experiment can be found in section 6.7.

b. Optical Emission Spectroscopy

This was used to determine the elements which were present in the plasma. Data were collected with a Monolight 6800 Series Optical Spectrum Analyser in the range 200-900 nm.

c. Scanning Electron Microscope

A Hitachi S-2700 SEM was used to examine the surface morphology of the diamond films.

d. Laser Ionisation Mass Analyser

The same instrument outlined in section 2.4 of this chapter was used to examine the contents of the grown diamond films.

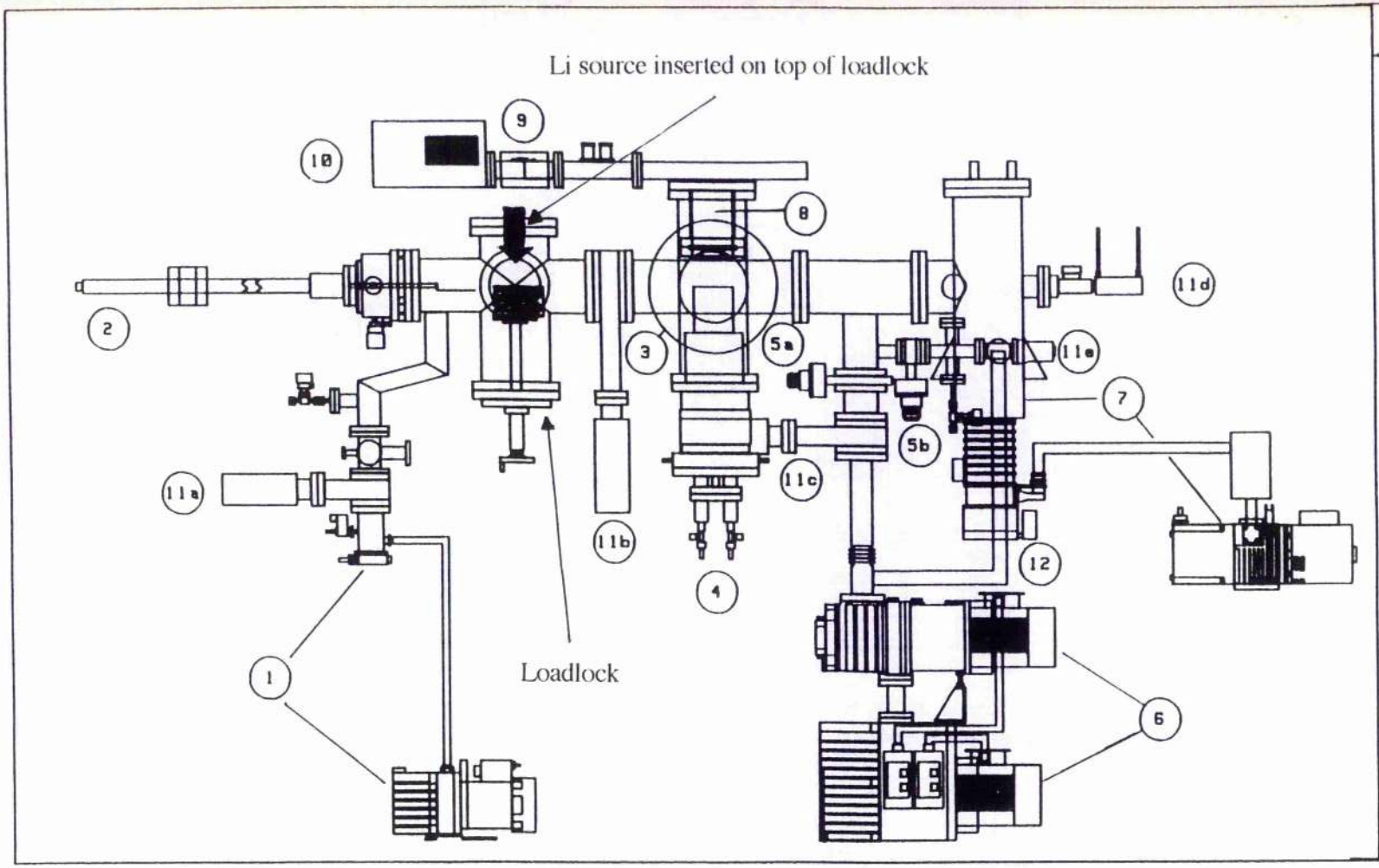

	KEY
1	loadlock pumping system
2	transfer arm
3	spherical multi-port growth chamber
4	heated platen
5 a-b	throttle valves
6	roots pumping system
7	diffusion pump system
8	microwave air cavity
9	dummy load
10	1kW microwave source
11 a-e	pneumatic gate valves
12	bypass line

Fig. 2-7. Schematic diagram of the microwave enhanced chemical vapour deposition (MWECVD) apparatus used for growing diamond films. Taken from reference [48].

Chapter 3

Some Theory Behind the Experimental Techniques

3.1 X-Ray Powder Diffraction

The following paragraphs provide a brief synopsis of how the X-ray diffractometers mentioned in chapter 2 ensure that each intercalation electrode and solid electrolyte possesses the predicted crystal structure.

Diffraction has been in use since the early part of this century not only for the determination of the structure of crystalline materials, but also for their fingerprint characterisation. X-rays are electromagnetic radiation of wavelength ~1Å (10^{-10}m). They occur in part of the electromagnetic spectrum between γ rays and the ultraviolet and are produced when high-energy charged particles, e.g. electrons accelerated through 30,000V, collide with matter.

Crystals with regularly repeating structures are capable of diffracting X-ray radiation since it has a wavelength similar to the interatomic separation ~1Å. This situation is analogous to the diffraction of light by an optical grating. When an X-ray beam is incident on a set of lattice planes there is some reflection from each plane, but a diffracted beam only occurs when there is constructive interference of the reflected rays, or, when Bragg's Law (Eq. 3-1) is satisfied,

$$2d\sin\theta = n\lambda. \qquad (3\text{-}1)$$

Here: d is equal to the distance separating each plane; θ is the angle of incidence of the X-rays; and nλ corresponds to an integral number of X-ray wavelengths. In practice n is equal to 1. For situations where, say n=2, the d-spacing is instead halved by doubling up the number of planes in the set; hence n is left equal to 1. Now by varying θ over a specified range the number of reflections from the crystal can be detected and corresponding d spacings can be calculated.

By using the results of this experiment in conjunction with existing powder diffraction data concerning the materials used throughout this work, it was possible to ensure that each prepared batch of materials had the correct crystal structures.

3.2 Electroanalytical Methods

1) Introduction

Throughout the three results chapters, electroanalytical techniques are used to gain an insight into atomic behaviour on the metal gauze surface upon which the alkali metals are produced. It is the purpose of this introduction to state some fundamental rules upon which the interpretation of data from electrochemical measurement is based.

Nernst Equation

Equation 3-2 represents a reversible electrode reaction during which an oxidisable species O is reduced to R by n electrons and the reducible species R is oxidised to O and n electrons,

$$O + ne \rightleftharpoons R. \qquad (3\text{-}2)$$

The following expression called the Nernst equation relates the electrode potential E to the standard potential $E^{o}_{ox/red}$ and the activities of the components of the system, a_{red} and a_{ox}.

$$E = E^{o}_{ox/red} + (RT/nF)\ln(a_{ox}/a_{red}). \qquad (3\text{-}3)$$

It is very often necessary to characterise the redox properties of a given system with unknown activity coefficients in a state far from standard conditions. For this purpose, the formal potential ($E^{o'}$) is introduced, defined in terms of concentration (Eq. 3-4).

$$E = E^{o'} + (RT/nF)\ln(c_{ox}/c_{red}). \qquad (3\text{-}4)$$

The formal potential is the potential assumed by an electrode immersed in a solution with unit concentrations of all the species appearing in the Nernst equation.

Not only is it important to know that electrode potential changes with the concentration of electroactive species, it is also beneficial to know how it changes the rate of an electrode reaction.

Butler-Volmer Equation

The following semi-empirical treatment of electron transfer culminates in the derivation of the Butler-Volmer equation; an expression upon which many electroanalytical techniques "pivot".

Similar to chemical reactions the rate constants of electrode reactions can be written in terms of the Arrhenius equation. The following two Arrhenius expressions relate the potential dependent anodic (k_a) and cathodic (k_c) rate constants to the corresponding potential dependent activation enthalpies ΔH_a and ΔH_c,

$$k_a = P_a \exp(-\Delta H_a/RT) \qquad (3\text{-}5)$$

$$k_c = P_c \exp(-\Delta H_c/RT). \qquad (3\text{-}6)$$

Equations 3-7 and 3-8 show how ΔH_c and ΔH_a are potential dependent. α is known as the electron transfer coefficient and the fact that it is often experimentally found to equal 0.5 signifies that the transition state is usually located approximately half way between the electrode surface and the outer Helmholtz plane.

$$\Delta H_c = \Delta H_c^{o} + \alpha nFE \qquad (3\text{-}7)$$

$$\Delta H_a = \Delta H_a^{o} - (1-\alpha)nFE \qquad (3\text{-}8)$$

According to the definition of the rate of an electrode reaction, the current densities of both anodic and cathodic electrode reactions are given by Eqs. 3-9 and 3-10 respectively,

$$j_a = nFk_a c_{red} \qquad (3\text{-}9)$$

$$-j_c = nFk_c c_{ox}. \qquad (3\text{-}10)$$

The overall current density is given by,

$$j = j_a + j_c = nF(k_a c_{red} - k_c c_{ox}). \qquad (3\text{-}11)$$

When $j = 0$, the system is in equilibrium and,

$$k_a c_{red} = k_c c_{ox} > 0. \qquad (3\text{-}12)$$

The reason why the above products do not equal zero is because, like chemical equilibria, electrode equilibria also have a dynamic character.

Now when $c_{ox} = c_{red}$ at the formal potential ($E^{o'}$ in equation 3-4),

$$k_a = k_c = k^o. \qquad (3\text{-}13)$$

where k^o is termed the formal rate constant.

A combination of Eqs. 3-5, 3-6, 3-7, 3-8 and 3-13 gives Eq. 3-14,

$$k^o = P_a \exp(-\Delta H_a^o + (1-\alpha)nFE^{o'}/RT) = P_c \exp(-\Delta H_c^o - \alpha nFE^{o'}/RT). \qquad (3\text{-}14)$$

By considering this equation along with Eqs. 3-5, 3-6, 3-7 and 3-8 once more; it is apparent that,

$$k_a = k^o \exp[(1-\alpha)nF(E-E^{o'})/RT] \qquad (3\text{-}15)$$

and,

$$k_c = k^o \exp[-\alpha nF(E-E^{o'})/RT]. \qquad (3\text{-}16)$$

The substitution of these expressions into Eq. 3-11 gives the following important result which relates the overall current density (j) or more simply, the rate of the electrode reaction, to the electrode potential E,

$$j = nFk^o[\exp[(1-\alpha)nF(E-E^{o'})/RT]c_{red} - \exp[-\alpha nF(E-E^{o'})/RT]c_{ox}]. \qquad (3\text{-}17)$$

At equilibrium the two opposing currents pass through the electrode with values termed the exchange current (j_o). j_o can be shown to be dependent on the magnitude of c_{ox} and c_{red} by manipulating Eq. 3-17 to give 3-18,

$$j_o/nF = c_{ox}k^o\exp[-\alpha nF(E-E^{o'})/RT] = c_{red}k^o\exp[(1-\alpha)nF(E-E^{o'})/RT]. \qquad (3\text{-}18)$$

By replacing $E-E^{o'}$ with its status in the Nernst equation (Eq. 3-4) the next relationship, which allows the electron transfer coefficient to be found from the dependence of j_o on c_{ox} or c_{red}, is derived,

$$j_o = nFk^o c_{ox}^{1-\alpha} c_{red}^{\alpha}. \qquad (3\text{-}19)$$

Finally in order to arrive at the Butler-Volmer equation which relates current density to overpotential η, a measure of the electrode potential minus the equilibrium electrode potential; the values for k^o from Eq. 3-19 and $E-E^{o'}$ from the following expression,

$$E - E^{o'} = \eta + (RT/nF)\ln(c_{ox}/c_{red}) \qquad (3\text{-}20)$$

are substituted into Eq. 3-17.

$$j = j_o[\exp[(1-\alpha)nF\eta/RT] - \exp[-\alpha nF\eta/RT]] \qquad (3\text{-}21)$$

According to the Butler-Volmer equation a graph of j vs.η takes the form of the hyperbolic function $j = \sinh\eta$ and the j-η dependence is often termed the voltammogram.

Tafel Equations

Eqs. 3-22 - 3-24 are named after J. Tafel who formulated them as an empirical relationship for the evolution of hydrogen. They enable experimental voltammograms of electrochemical systems to be manipulated in order that they can produce values of the fundamental parameters associated with cell reactions.

1. <u>When the overpotential is small ($\eta << 0.01V$)</u>

By expanding the exponential terms in Eq. 3-21 as a Taylor series (i.e. $e^x = 1 + x + x^2/2! + ...$) it reduces to Eq. 3-22.

$$j = j_o nF\eta/RT \qquad (3\text{-}22)$$

2. <u>When the overpotential is large ($\eta >> 0.1V$) and anodic</u>

The second exponential term in Eq. 3-21 is much smaller than the first; therefore it becomes Eq. 3-23.

$$j = j_o\exp[(1-\alpha)nF\eta/RT] \qquad (3\text{-}23)$$

3. When the overpotential is large ($\eta >> 0.1V$) and cathodic

The first exponential term in Eq. 3-21 is much smaller and therefore it can be neglected to give Eq. 3-24.

$$j = -j_o \exp(-\alpha n F \eta / RT) \qquad (3\text{-}24)$$

The preceding expressions have dealt solely with theory behind electron transfer. Besides this, mass transport and phase formation also play important roles during electrochemical reactions. Aspects of these two processes are dealt with in the following three sections on electroanalytical techniques.

2) Potential Step

The potential step (or chronoamperometry) experiment is outlined first because it is the simplest type of non-steady state technique. It involves an instantaneous perturbation of electrode potential followed by scrutiny of the variation in current with time. This variation often leads to deduction of the rate controlling process of the electrode reaction e.g. electron transfer, diffusion or phase formation. These three processes are respectively represented by current-time transients (CTTs) 3a, 3b and 3c in Fig. 3-1.

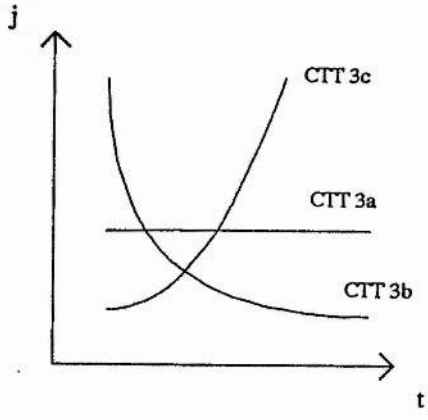

Fig. 3-1. Current-time responses to potential steps.

CTT 3a

This shows an invariant Faradaic current which may arise in two circumstances.

1) If a liquid electrolyte/electrode interface is being studied and k^o for $O + e \rightleftharpoons R$ is very small.

If this is the case the surface concentration of O will not change significantly due to the pulse. Therefore, the electrochemical mechanism is kinetically controlled since the slowest step involves the transfer of an electron to O. Theory concerning the Butler-Volmer equation listed in the introduction can be used to extract values of transfer coefficients and exchange current densities from steady state current-voltage measurements of systems possessing this characteristic.

2) If a solid electrolyte/electrode interface is being studied

The surface concentration of O does not change due to the pulse because this would violate electroneutrality which must hold within the solid electrolyte.

CTT 3b

Current decreases with $t^{-1/2}$. This is commonly encountered when liquid electrolyte/electrode interfaces are being studied and is a consequence of diffusion of O from the bulk electrolyte to the electrode surface. For many electrode processes the rates of electron transfer are high compared with that of steady state mass transport and CTTs of the shape depicted by 3b are frequently used as a test for diffusion control by the observation of a straight line through the origin when current is plotted against corresponding values of $t^{-1/2}$.

To understand why j should decrease with $t^{-1/2}$ as a result of diffusion it is helpful to assume that the electrode is perfectly flat and of infinite dimensions, so that the relaxation of a concentration gradient can only occur perpendicular to the electrode surface. This allows diffusion to be characterized by Fick's laws in a one dimensional form. In order to arrive at the equation which mimics CTT 3b it is necessary to solve

Fick's second law (Eq. 3-25), a 2nd order differential equation which describes the change in concentration of a species with time due to diffusion, by employing the following initial and boundary conditions.

initial condition: at t=0 and at all x values, $c_{ox} = c_{ox}^{\infty}$

boundary condition: for $t > 0$, at $x=0$, $c_{ox}^{o} = 0$

at $x=\infty$, $c_{ox} = c_{ox}^{\infty}$

$$\delta c_{ox}/\delta t = D.\delta^2 c_{ox}/\delta x^2 \qquad (3\text{-}25)$$

This leads to Eq. 3-26: the Cottrell equation.

$$j = nFD^{1/2}c_{ox}^{\infty}/\pi^{1/2}t^{1/2} \qquad (3\text{-}26)$$

CTT 3c

A rising CTT is indicative of an electrode process that allows the nucleation and growth of a new phase on the electrode surface. This can be explained by considering the nucleation and growth of an isolated disc which is one atom thick. If the rate determining step is the incorporation of atoms or molecules at the edge of the disc, the current flowing into this centre will be

$$j = nFk^{*}2\pi rh. \qquad (3\text{-}27)$$

Therefore as the radius (r) of the disc increases so does the current.

Theoretical analyses of plots like CTT 3c generally involve treating j as a function of t^n, where n depends on: the type of nucleation involved; the geometry of phase growth; and the rate determining step in phase formation. The following example

shows how a CTT corresponding to the nucleation and growth of a disc which is one atom thick can be predicted.

The current flowing into the centre is once again given by Eq. 3-27. Q(r), the amount of charge required to form a disc of new material is represented by,

$$Q(r) = \pi r^2 hnF\rho/M. \qquad (3\text{-}28)$$

By differentiating this expression with respect to time, the instantaneous current into the centre with radius r is,

$$j(r,t) = (2\pi hnF\rho r(t)/M).dr(t)/dt. \qquad (3\text{-}29)$$

Now by rearranging Eq. 3-29 and substituting j(r,t) for the meaning of j in Eq. 3-27, the rate of radial expansion is given by,

$$dr(t)/dt = Mk^*/\rho. \qquad (3\text{-}30)$$

It follows that the radius at any time can be obtained by integrating Eq. 3-30 to give,

$$r(t) = Mk^*t/\rho. \qquad (3\text{-}31)$$

When this is substituted into Eq. 3-27,

$$j = 2\pi nFk^{*2}hMt/\rho. \qquad (3\text{-}32)$$

And so the current associated with the growth of an isolated disc shaped nucleus is therefore expected to increase linearly with time.

When nucleation and growth of the more complicated three dimensional centres (e.g. right circular cones [49], hemispheres [50] and hemispheroids [51]) are considered it

is found, again by geometrical reasoning, that current can vary as a *power* of t. Thus when experimental rising CTTs are superimposed on the variety predicted by theory it is possible to deduce the shapes that nucleation points take as phase formation proceeds. Many papers can be found in the electrochemical literature which include this type of experiment. They are often supplemented with additional evidence gained via microscopic techniques such as SEM (scanning electron microscopy [52]) and more recently SPM (scanning probe microscopy [53]).

3) Cyclic Voltammetry

This technique involves the study of the j-E curve obtained after a great number of potential steps have been applied to the system. In order to obtain this data, the potentiostat mentioned in chapter 2 is used to sweep the potential of the working electrode linearly with time whilst monitoring the current which flows through it. The scan rate (υ) can be varied from that which is relatively slow (e.g. 1 mV/s) to that which is relatively fast (e.g. 200 mV/s) and the resulting j-E trace represents the electrode processes occurring within the potential range of interest.

Figure 3-2 shows the cyclic voltammogram for a reversible electrode process occurring with the electrode immersed in a liquid or polymer electrolyte.

The word *reversible* implies that the rate of electron transfer is rapid compared to the rate of mass transport (diffusion). If we begin with pure O, reduction to R occurs at potentials negative of $E^{o'}$. The current increases as the rate of reduction increases at more negative potentials but eventually a maximum is reached and thereafter the current decreases steadily. This cathodic peak is located at the same potential (E_p) irrespective of sweep rate and results from the competition of two factors: the increase in the rate of reduction as the potential is made more negative and the development of a thickening depletion layer across which O must diffuse. At potentials greater than the peak, the O concentration at the electrode surface is small compared to the concentration far from the electrode and the current is controlled by the rate of

diffusion of O through the depletion layer. The same argument applies to the occurrence of the anodic peak which corresponds to the oxidation of R to O.

When an *irreversible* system is studied, the potentials corresponding to E_p are found to vary with the sweep rate. This is because the rate of electron transfer is comparable with that of mass transfer.

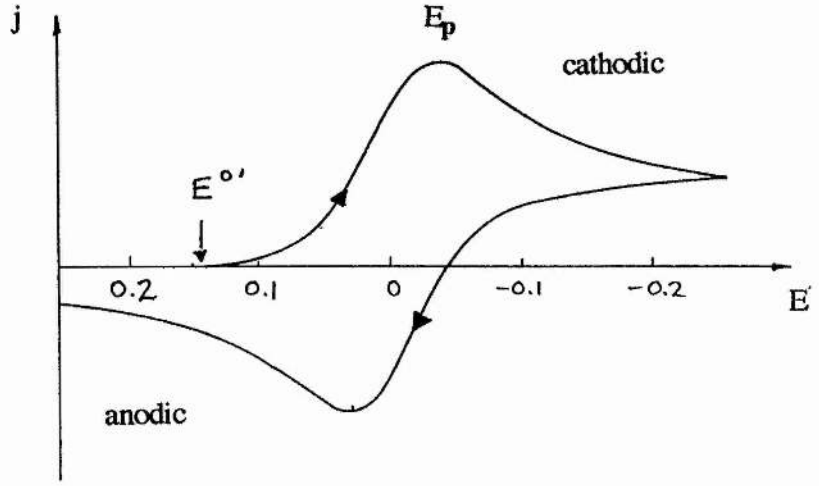

Fig. 3-2. The cyclic voltammogram of a reversible system.

The formation of a new phase on the working electrode can also be observed via the cyclic voltammetry experiment. Figure 3-3 is a typical CV representing the formation (plating) and removal (stripping) of a metal M. The most important feature is the loop in the cathodic region. This represents phase formation on the electrode surface because on sweep reversal, the system is still at a potential where growth of the deposit can continue. Therefore values of current on the reverse sweep should be higher than those on the forward. Upon reaching anodic potentials the deposit is oxidised and an anodic wave obtained. By integrating the values of charge bound by forward and reverse anodic sweeps it is possible to determine the magnitude of

charge and hence the number of moles of R deposited on the electrode surface. Comparison of this value with that obtained from integration of the cathodic profiles enables the efficiency of the plating and stripping process to be assessed. This is known as a Coulombic efficiency calculation.

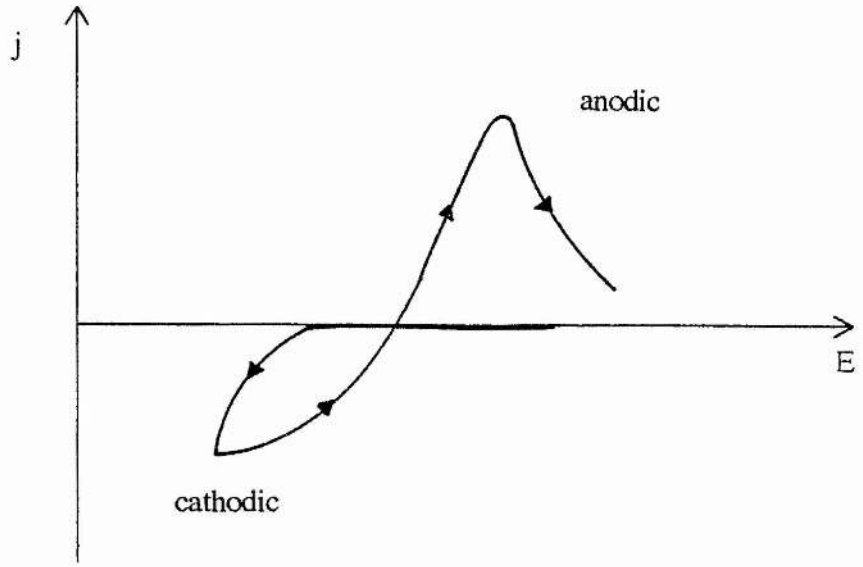

Fig. 3-3. Cyclic voltammogram representing the nucleation and growth of a new phase on an electrode surface.

4) AC Impedance

The two previous techniques allow the deduction of electrode processes which govern a measurable *time* dependent variable such as current.

AC impedance involves measuring impedances due to electrochemical processes as a function of the *frequency* of an applied sinusoidal voltage. These impedances can then be used to interpret the mechanisms of electrochemical phenomena in attempts at arriving at the same conclusions as those that can be drawn from the time dependent methods. The ac method is generally more versatile than transient techniques, such as chronoamperometry, when used to study electrode kinetics however. This is because

information concerning fast reactions has to be obtained at short times otherwise diffusion rather than kinetics becomes rate determining. The instrumentation responsible for the ac technique allows measurements to be made on the microsecond timescale which is considerably faster than the timescale of a pulse experiment.

Data obtained from electrochemical systems often resemble the graphs shown in Fig. 3-4.

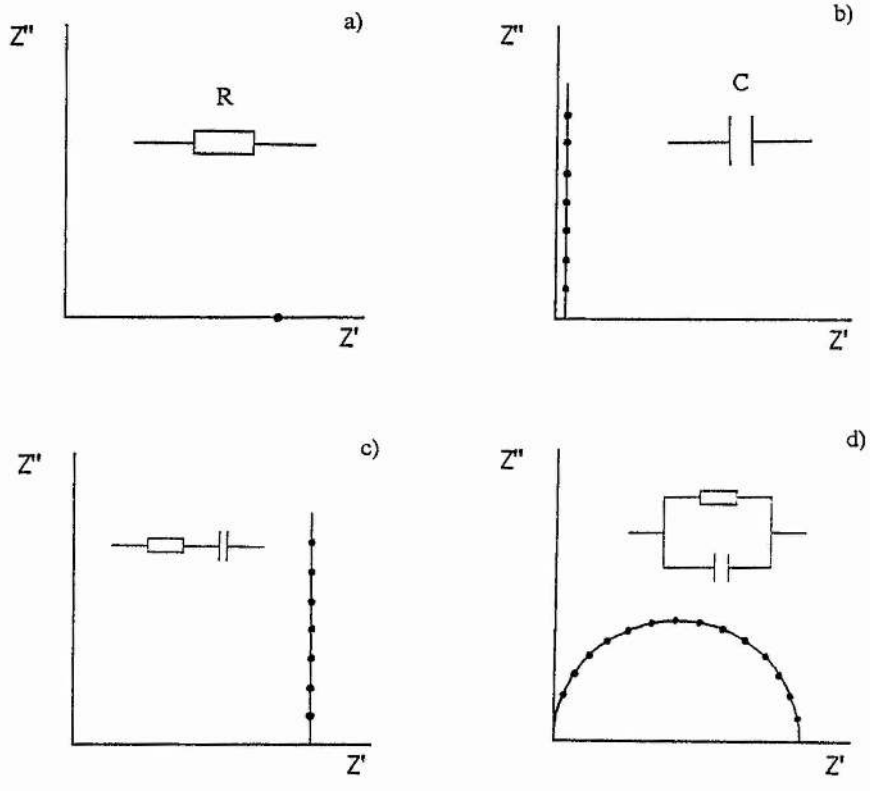

Fig. 3-4. a) The complex plane impedance plot representing a resistor. b) The complex plane impedance plot representing a capacitor. c) A resistor and a capacitor in series. d) A resistor and a capacitor in parallel.

The aims of the following parts of this section are to explain the meaning of each of these graphs and their electrochemical significance, but first an explanation of the axes symbols Z" and Z' is necessary.

When a sinusoidally varying voltage is applied to a conductor the corresponding current induced by this also varies in a sinusoidal manner. Two parameters relate this current to the voltage:

1) The magnitude of impedance Z (expressed in ohms), which is defined as being the ratio of voltage to current maxima V_{max}/j_{max}.

2) A phase angle difference θ between the sinusoidal E and j.

Figure 3-5 is a vector diagram which relates these two parameters to Z" and Z'

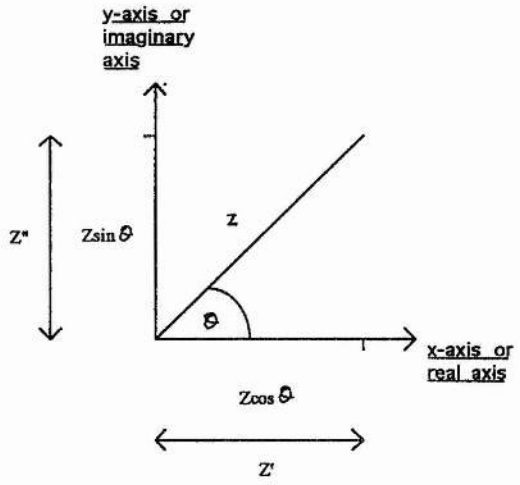

Fig. 3-5. A vector or Argand diagram showing how Z" and Z' are related to phase angle (θ) and impedance (Z).

It is now apparent that Z' = Zcosθ and Z" = Zsinθ. Another way of expressing Z' and Z" is to make them the real and imaginary parts of a complex number (Z^*) respectively i.e. $Z^* = Z' - iZ"$ where i is the complex number operator, $\sqrt{-1}$. Due to this, the graphs shown in Fig. 3-4 are often referred to as complex plane impedance plots.

The Meaning of Figures 3-4a)-d)

1) Figure 3-4 a) - Purely Resistive Circuit

In a purely resistive circuit fed from an ac voltage, current and voltage are exactly in phase, therefore $\theta = 0°$ and $Z = Z' = R$.

2) Figure 3-4 b) - Purely Capacitive Circuit

In a purely capacitive circuit the voltage lags behind the current by 90°. This results in a frequency dependent impedance which can be derived in the following way.

The current j drawn by a capacitor is the rate of change of its charge (Eq. 3-33)

$$j = dq/dt. \qquad (3\text{-}33)$$

Therefore,

$$j = d(CE)/dt. \qquad (3\text{-}34)$$

And,

$$j = C.dE/dt. \qquad (3\text{-}35)$$

When a sinusoidally varying potential defined by Eq. 3-36 is applied to the capacitor,

$$E = E_M \sin\omega t. \qquad (3\text{-}36)$$

Then,

$$j = C.d(E_M \sin\omega t)/dt. \qquad (3\text{-}37)$$

And so,

$$j = \omega C E_M \cos\omega t. \qquad 3\text{-}38$$

Which is equivalent to current leading voltage by 90° (Eq. 3-39).

$$j = \omega C E_M \sin(\omega t + \pi/2). \qquad (3\text{-}39)$$

Now by definition,

$$Z = E/j. \qquad (3\text{-}40)$$

So,

$$Z = E_M \sin\omega t / \omega C E_M \sin(\omega t + \pi/2). \qquad (3\text{-}41)$$

When t=0,

$$Z = E_M(0°)/\omega C E_M(90°) \qquad (3\text{-}42)$$

So,

$$Z = 1/\omega C(90°). \qquad (3\text{-}43)$$

The impedance of the capacitor is therefore frequency dependent and can be expressed by the following complex notation (Eq. 3-44),

$$Z = -i/\omega C. \qquad (3\text{-}44)$$

When capacitances are plotted on the complex impedance plane as a function of frequency, a vertical spike coincident with the Z" (imaginary) axis is obtained since Z' = 0 for a phase difference of 90°. Fig. 3-4 b) shows the spike displaced slightly along the Z' axis for clarity.

3) Figure 3-4 c) - Resistor and Capacitor in Series

Impedances are directly additive when resistors and capacitors are connected in series. Therefore, $Z^* = R - i/\omega C$ and the complex impedance plane defines a vertical spike displaced a distance R along the real axis.

4) Figure 3-4 d) - Resistor and Capacitor in Parallel

When resistors and capacitors are connected in parallel the reciprocal of the total impedance equals the sum total of the reciprocals of the individual impedances. The total impedance, Z^*, can be expressed by Eq. 3-45.

$$Z^* = R[1/(1 + (\omega CR)^2)] - iR[\omega RC/(1 + (\omega RC)^2)] \qquad (3\text{-}45)$$

This equation, providing the Z' and Z" scales are equal, defines a semicircle in the complex impedance plane, with a diameter R extending along the real axis.

At the frequency corresponding to the maximum of the semicircle, ω_{max}, the magnitude of the impedance of the resistor and capacitance are equal:

$$R = 1/\omega_{max}C \qquad (3\text{-}46)$$

By extracting values of ω_{max} from plots of Z" against logω (Bode plots), this expression can be used to calculate values of capacitance.

The Electrochemical Significance of Resistors and Capacitors

In electrochemistry, resistances can represent physical or kinetic barriers which inhibit phenomena such as ion transport or charge transfer. Capacitances can, for example, represent dielectric polarisation between the immobile hydrocarbon chains of a polymer electrolyte, or the separation of charge normal to an interface comprising an electrode and electrolyte (i.e. the double layer capacitance).

The following example shows how an equivalent circuit can be used to represent physical phenomena occurring within an electrochemical system. Figure 3-6 is called the Randles equivalent circuit and is often the central part of equivalent circuits used to mimic the frequency response of electrochemical cells.

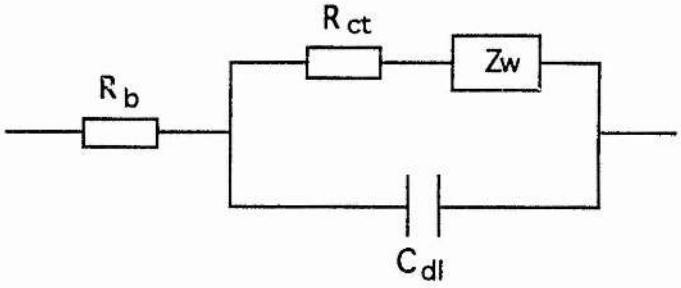

Fig. 3-6. An example of an equivalent circuit that represents processes occurring within an electrochemical cell.

The symbols have the following meanings:

R_b = bulk resistance of the electrolyte (Ω)

R_{ct} = charge - transfer resistance (Ω)

C_{dl} = double layer capacitance (Farads)

Z_w = Warburg diffusional impedance (Ω)

The corresponding complex impedance plane plot for this equivalent circuit is shown in Fig. 3-7. A semicircle, corresponding to the parallel combination of charge transfer resistance and double layer capacitance at the electrode/electrolyte interface is displaced along the Z' axis by a value R_b which represents the bulk resistance of the electrolyte.

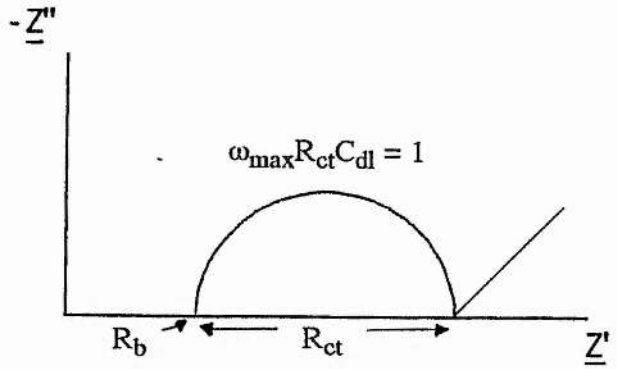

Fig. 3-7. The complex impedance plane plot which originates from the equivalent circuit in Fig. 3-6.

By varying, for example, the temperature of the system, accumulating data and using the equivalent circuit to "break" the data into individual components, temperature dependent values of R_{ct} could be determined. This would enable values of activation energies for electron transfer to be calculated since R_{ct} is indirectly related to the rate of charge transfer.

One aspect of Fig. 3-6 which should also be explained is the symbol Z_w (Warburg impedance) which leads to the line inclined at an angle of 45° on Fig. 3-7 and is a consequence of diffusion. The representation of diffusion on the complex impedance plane can be derived theoretically by solving Fick's second law (Eq. 3-25) with appropriate boundary conditions [54].

Cell Testing: Electrochemistry 1

4.1 Manufacture and Operation of the Li Sources

1) Introduction

Solid electrolytes and intercalation electrodes used to construct the lithium sources were prepared by high temperature solid state reactions as described in chapter 2. Pellets of the materials could be prepared by pressing uniaxially and sintering them at high temperatures to improve their mechanical strengths. In producing all solid state ceramic cells major difficulties were encountered in obtaining a robust interface between electrolyte and electrode which could survive mechanical stress at high temperatures and ensure intimate electrode contact. Optimum electrode contact is essential because the rate at which electrode processes occur and hence the performance that may be obtained is dependent not only on the conductivity of the solid electrolyte and the charge transfer or diffusion-limited impedance of the electrode reactions, but also on the extent of contact area between solid phases comprising the electrodes and the ionic conductor [55].

2) Experimental

The first attempt at constructing the Li source involved the use of lithium germanium vanadate as the solid electrolyte. Due to problems associated with this material during cell operation, an alternative solid electrolyte (lithium phosphosilicate) had to be found before results which indicated the successful production of pure lithium vapour were obtained. Both attempts employed $LiMn_2O_4$ as the intercalation electrode.

a) "Lithium Germanium Vanadate" Source

The X-ray powder diffraction patterns shown in figures 4-1 and 4-2 represent the crystal structures of lithium germanium vanadate and lithium manganese oxide respectively. The structure of the prepared $Li_{3.5}Ge_{0.5}V_{0.5}O_4$ was checked by generating its pattern from existing data [56] via the computer programme THEO

and comparing the two patterns (Figs. 4-1a and b). The powder pattern of $LiMn_2O_4$ was compared with data from ASTM 18-736 (Figs. 4-2a and b). In both cases the materials were found to be pure.

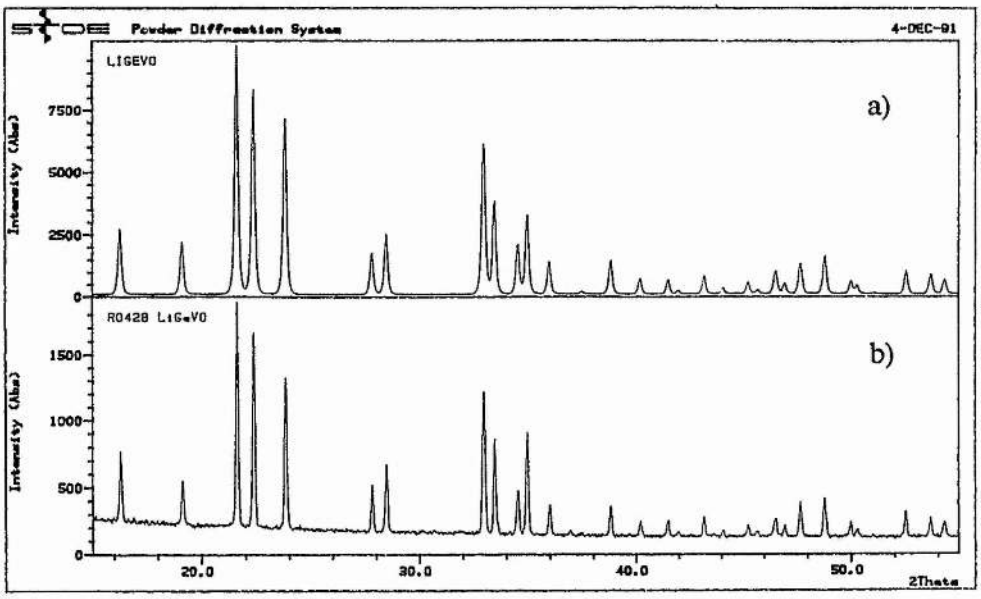

Fig. 4-1. a) Powder pattern of $Li_{3.5}Ge_{0.5}V_{0.5}O_4$ generated by THEO. b) Powder pattern of prepared $Li_{3.5}Ge_{0.5}V_{0.5}O_4$.

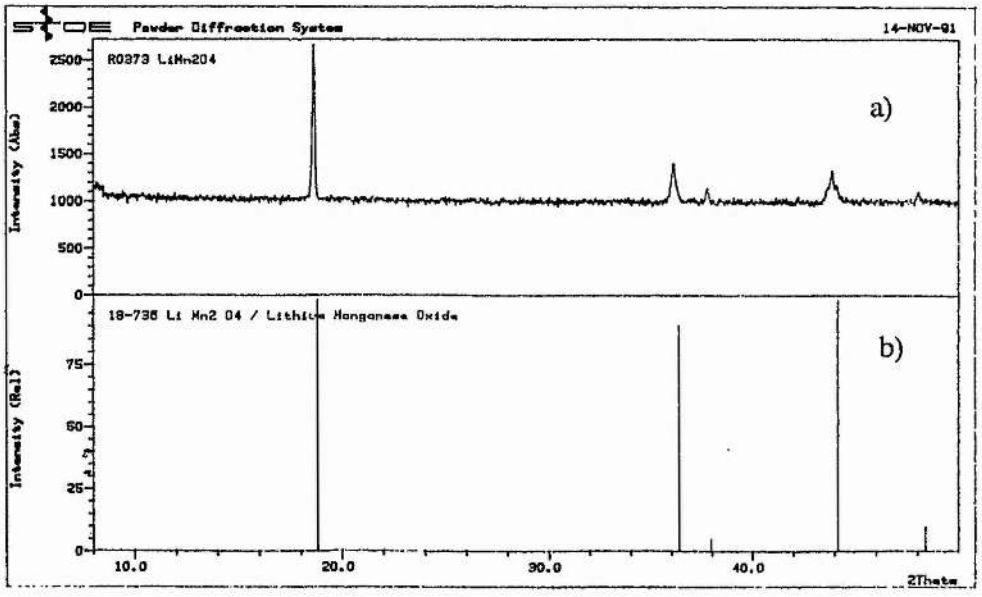

Fig. 4-2. a) Powder pattern of prepared $LiMn_2O_4$. b) Powder pattern of $LiMn_2O_4$ from ASTM 18-736.

Cell preparation involved using a glass filter funnel to transfer 0.4 g of lithium germanium vanadate into a 13 mm Specac die and pressing the material manually with the plunger before adding 4 drops of acetone as a binder. Initial attempts at pressing 0.5 g of $LiMn_2O_4$ directly on top of this led to fracture of the pellet at the interface after sintering. In order to circumvent this problem which was thought to be due to differences in thermal expansion of the two materials, the vanadate surface was sprinkled with a 1:1 molar mixture of the two materials until it was just no longer visible. Approximately half a regular spatula-full of interface material was required for this operation. The plunger was then used to compact the lithium germanium vanadate plus interface material manually before wetting the exposed surface of the interface with 4 drops of acetone. 0.5 g of $LiMn_2O_4$ was placed on top of this and the entire assembly then pressed by a weight of 1.5 tons for 5 minutes before sintering the resulting pellet (placed with its $LiMn_2O_4$ side down in a gold boat lined with $LiMn_2O_4$ powder and covered with $Li_{3.5}Ge_{0.5}V_{0.5}O_4$) from 25°C to 650°C and back to 25°C at a rate of 4°C/min in a tube furnace. On removal from the furnace the $LiMn_2O_4$ side of the pellet was painted with silver to act as a current collector.

b) "Lithium Phosphosilicate" Source

Figure 4-3 shows the X-ray powder diffraction pattern of $Li_{3.75}P_{0.25}Si_{0.75}O_4$. The material was prepared by a method outlined by Shannon at al [57]: in their paper they also enclosed a diffraction pattern of the material which was used to ensure that the synthesised product held the correct crystal structure.

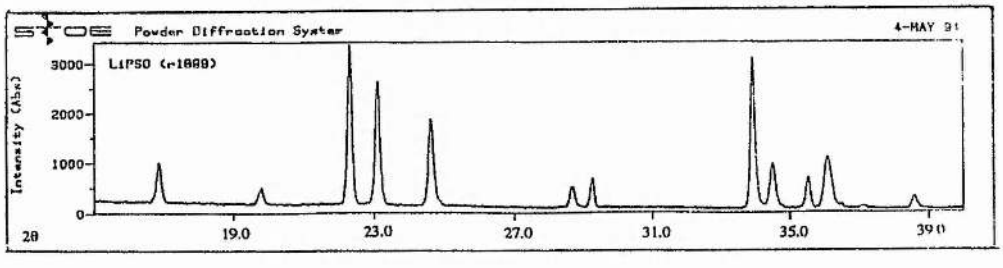

Fig. 4-3. Powder pattern of $Li_{3.75}P_{0.25}Si_{0.75}O_4$.

Once again a graded interface between intercalation electrode and solid electrolyte had to be inserted in order to facilitate the sintering process. 0.3g of the phosphosilicate was placed in the die and compacted manually. A 1:1 molar mixture of the two materials was then sprinkled on top of the electrolyte until its surface was just covered. This was followed by the addition of 6 drops of acetone then 0.5g of $LiMn_2O_4$. The powders were pressed together by a weight of 1 ton for 5 minutes and sintering was carried out in exactly the same manner as for the "lithium germanium vanadate" source.

The cells are illustrated in figure 4-4. On removal from the furnace a thin circular layer of silver paint was applied to the $LiMn_2O_4$ side of each pellet to act as a current collector. Circular pieces of stainless steel gauze were rubbed with emery paper, boiled in distilled water and dried with a heat gun before being placed on the electrolyte surfaces prior to the following LIMA experiments. During these experiments each source was placed in the cell holder shown in figure 4-5 and polarised at a certain temperature for a given period of time. This cell holder was designed to incorporate a stainless steel disk upon which deposition of lithium was intended to take place. The disk was positioned approximately 3 mm from the surface of the stainless steel gauze. Figure 4-6 shows the cell holder inside a stainless steel reaction chamber fitted with two electrode contacts, a thermocouple, and a pipe which allowed the attachment of a rotary vacuum pump capable of maintaining a vacuum of approximately 10^{-3} mbar. The reaction chamber was inserted inside a tube furnace and external circuitry was attached which incorporated a 10 V dc power supply and a resistor (R) in parallel with a digital voltmeter (DVM) to ensure that a current was passing through each source.

Fig. 4-4. a) "Lithium germanium vanadate" source. b) "Lithium phosphosilicate" source.

a)

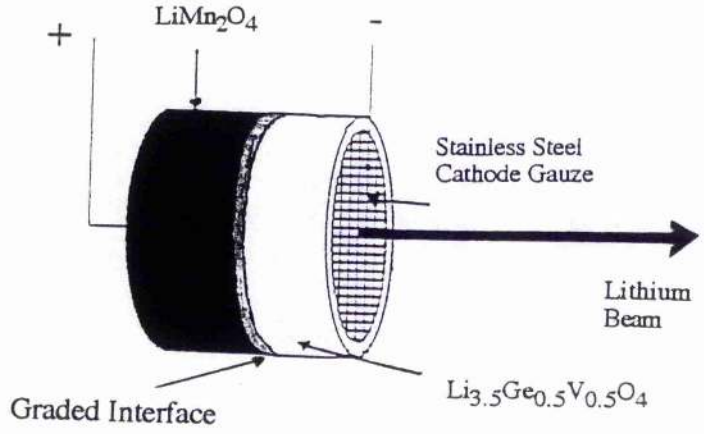

b)

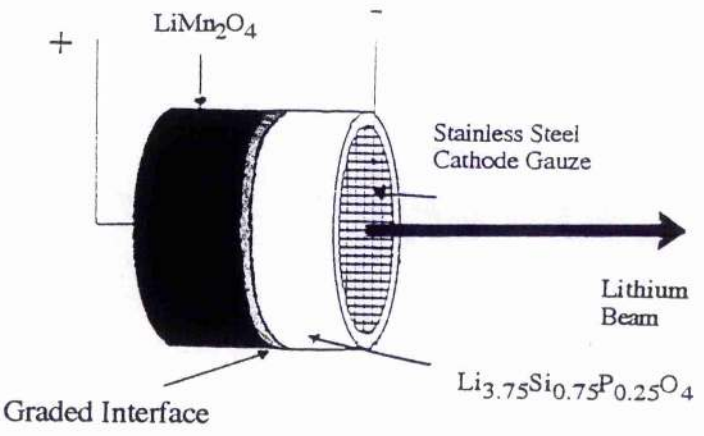

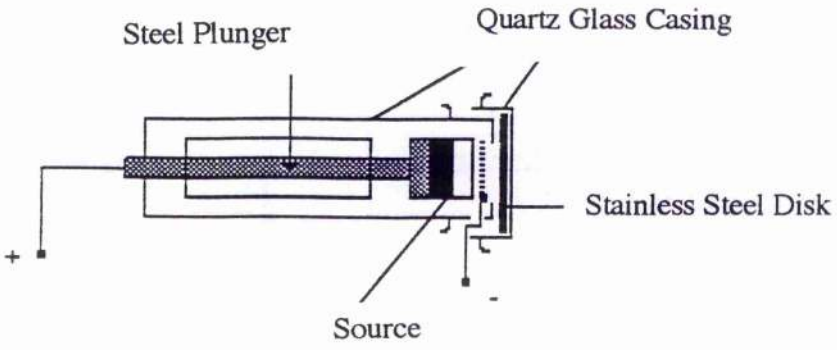

Fig. 4-5. Cell holder used for the LIMA experiment.

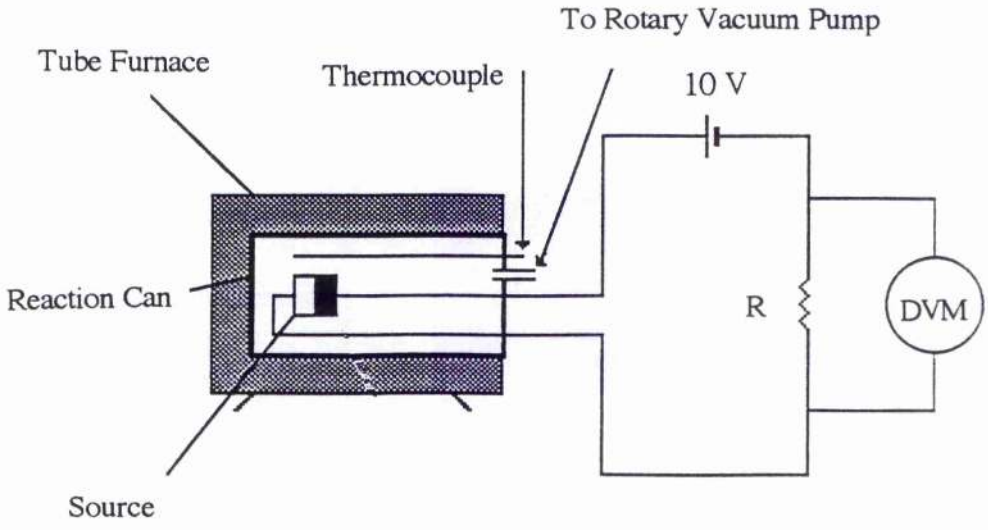

Fig. 4-6. Equipment used for polarising the sources at elevated temperatures.

Figure 4-7 provides a clearer representation of the source's operation during this experiment.

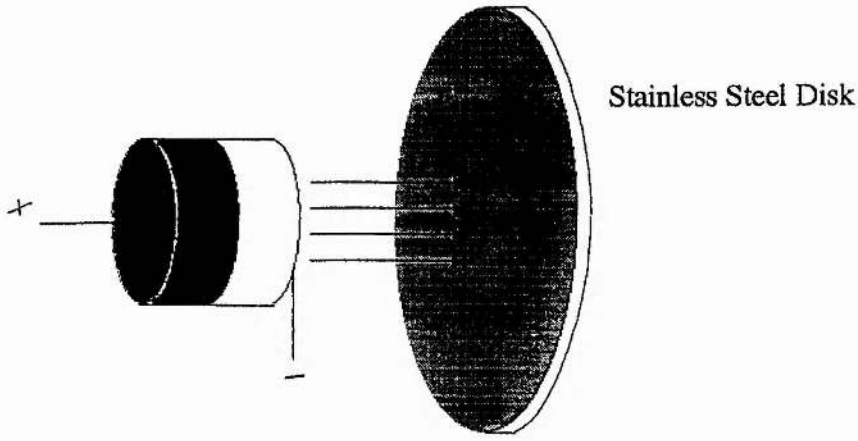

Fig. 4-7. A simplified view of the source at work.

Before being placed in the cell holder the disk was polished with diamond paste, rinsed with deionised water and dried in an oven at 100°C. An initial LIMA spectrum was recorded from the disk prior to experiment in order to ensure that this cleaning procedure had been successful in eradicating traces of any unwanted elements. Figure 4-8 shows a typical LIMA spectrum of the disk after cleaning.

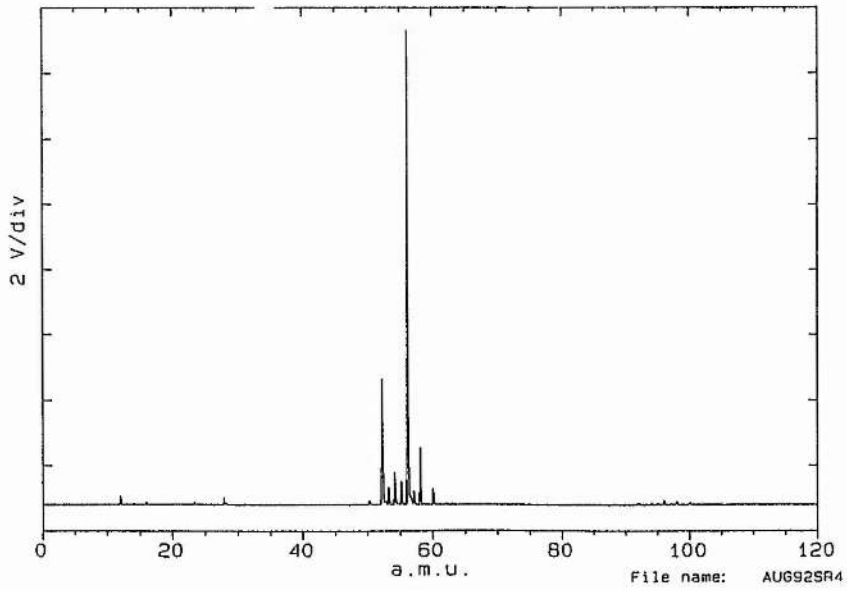

Fig. 4-8. LIMA spectrum of a clean disk. The peaks between m/z = 50-60 correspond to elements which constitute the stainless steel itself.

The cluster of peaks between mass to charge numbers 50 to 60 corresponds to elements which comprise the stainless steel itself; the most notable being iron (m/z = 56) and chromium (m/z = 52).

2) Results and Discussion

Table 4-1 lists the conditions under which each source was operated during the LIMA experiments.

Table 4-1.

Conditions	Cell Type	
	"$Li_{3.5}Ge_{0.5}V_{0.5}O_4$"	"$Li_{3.75}P_{0.25}Si_{0.75}O_4$"
Temperature (°C)	275	250
Voltage (V)	10	10
Duration of Polarisation	4 days	4 days
Chamber Pressure (mbar)	10^{-3}	10^{-3}
Current (μA)*	48	75

*The values of current correspond to those observed on ceasing polarisation of the cell.

The mass spectra in figure 4-9 were taken from the surface of the disk after passing a current through the "lithium germanium vanadate" source and also after a control experiment with the cell operating at the same temperature and for the same time but with the power switched off. These results show that lithium reached the disk only when the cell was polarised but on removal from the cell holder it was observed that the surface of the electrolyte had deteriorated. Preliminary experiments where the cell had been operated at potentials greater than 10 V often led to entire destruction of the cell. Figure 4-10 shows a LIMA spectrum taken from the surface of the disk after one such experiment. Peaks at m/z = 51 and 74 correspond to vanadium and germanium respectively.

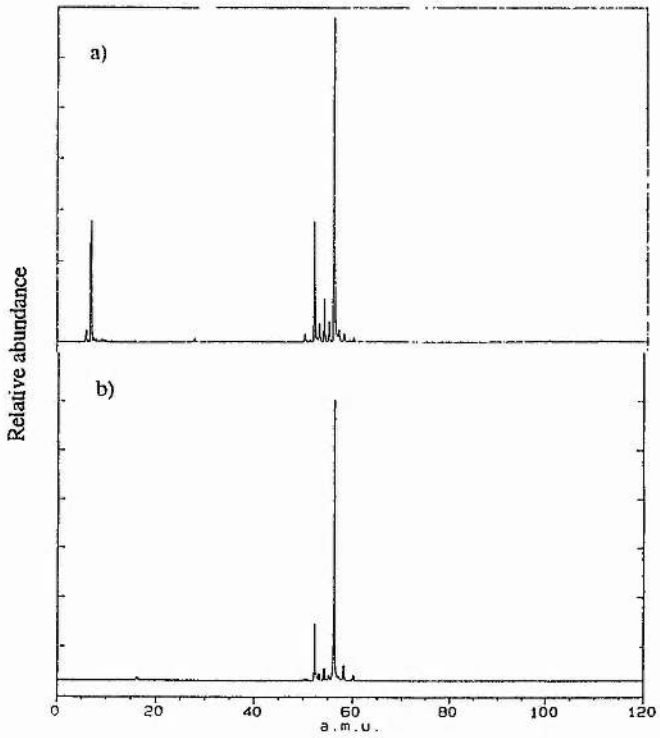

Fig. 4-9. a) LIMA spectrum taken from the surface of the stainless steel disk after polarising the "lithium germanium vanadate" source. The peak at m/z = 7 is due to lithium. b) After a control experiment with the power switched off.

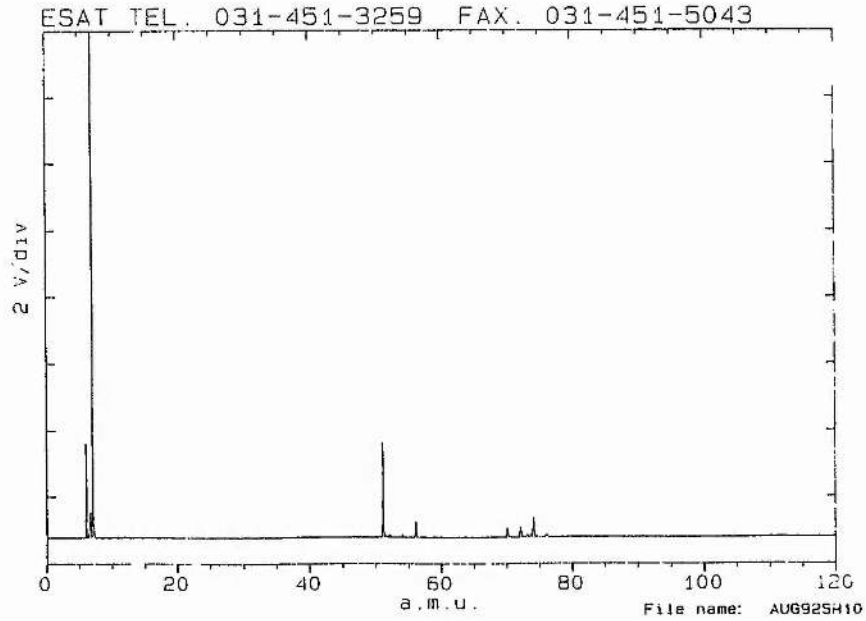

Fig. 4-10. LIMA spectrum taken from a disk contaminated with $Li_{3.5}Ge_{0.5}V_{0.5}O_4$ powder after polarisation. Peaks at m/z = 51 and 74 correspond to vanadium and germanium respectively.

To negotiate this problem, which may have been due to reduction of V^{5+} within the electrolyte, the experiment was repeated with the "lithium phosphosilicate" source. Figure 4-11 shows that this cell was also capable of producing a beam of pure lithium and on removal from the cell holder the electrolyte surface showed no deterioration.

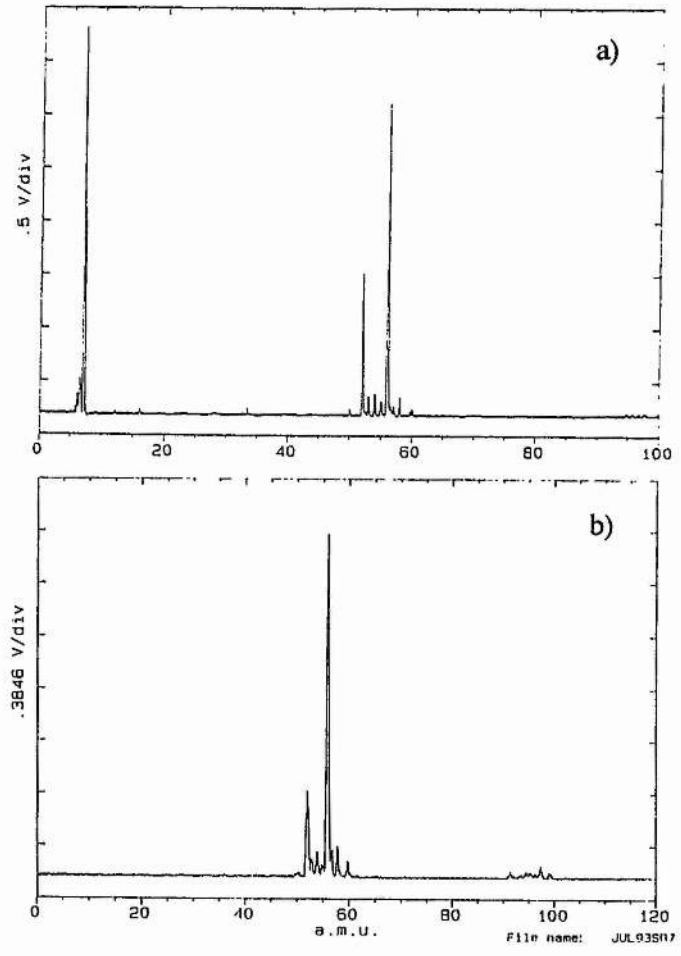

Fig. 4-11. a) LIMA spectrum taken from the surface of the stainless steel disk after polarising the "lithium phosphosilicate" source. b) After a control experiment with the cell switched off.

4.2 Cyclic Voltammetry with the Li Source Operating at 10^{-3} mbar

Since the LIMA experiment showed that the source released lithium when polarised at elevated temperature, it was important to learn more about the mechanism(s) behind its production. In order to start this investigation the three electrode cell shown in Fig. 2-2 was used to produce the following two cyclic voltammetry results.

Firstly, the potential was swept from 0 V to +3.0 V with respect to $LiMn_2O_4$ at a scan rate of 200 mV/s with the cell at 350°C and 10^{-3} mbar. This showed that there were no oxidation processes occurring up to this potential (Fig. 4-12).

Secondly, a cathodic scan from 0 V to -5 V and back to 0 V followed by an anodic scan to +5 V provided a nucleation loop at relatively high cathodic overpotentials (Fig. 4-13) which indicated the formation of lithium or lithium containing compounds on the stainless steel gauze surface. The Coulombic efficiency of the process was calculated by cutting and weighing the areas bound by the anodic and cathodic sweeps and using the ratio Q_a/Q_c where Q_a represents anodic charge and Q_c the cathodic. This gave a value of 0.74 which meant that 26% of the lithium produced during the reduction had evaporated.

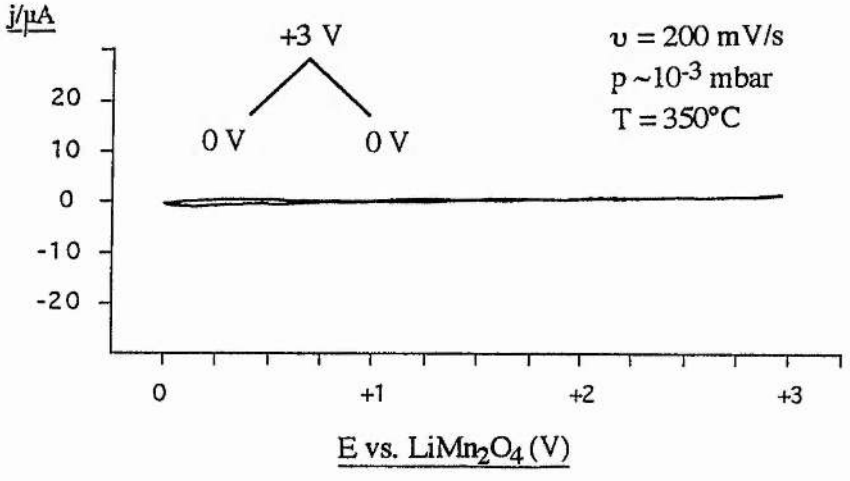

Fig. 4-12. A cyclic voltammogram of the Li source recorded at anodic potentials.

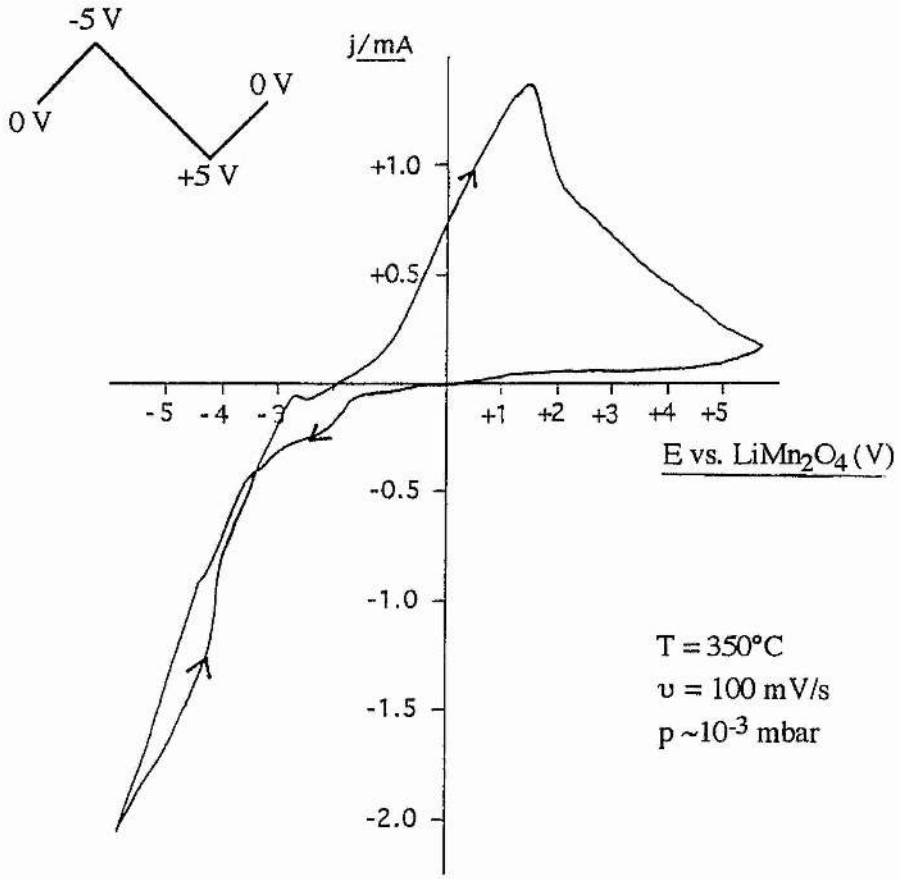

Fig. 4-13. A cyclic voltammogram of the Li source recorded at cathodic and anodic potentials and showing a nucleation loop in the cathodic region.

4.3 Manufacture and Operation of the K Source

A schematic diagram and some background concerning this source can be found on page 15 of the introduction. It is composed of a potassium ferrite intercalation electrode attached to K-BÁSE. Figures 4-14 and 4-15 are X-ray powder diffraction patterns of K-BASE and potassium ferrite respectively and are consistent with previous X-ray data [58 and 59 respectively] obtained from these compounds.

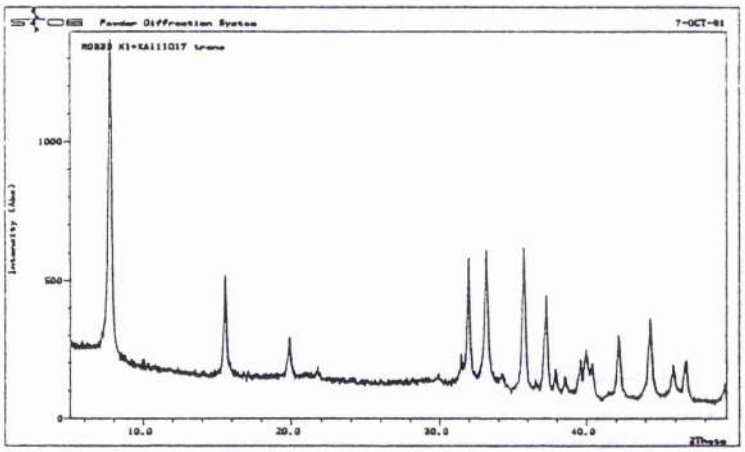

Fig. 4-14. Powder pattern of K-BASE.

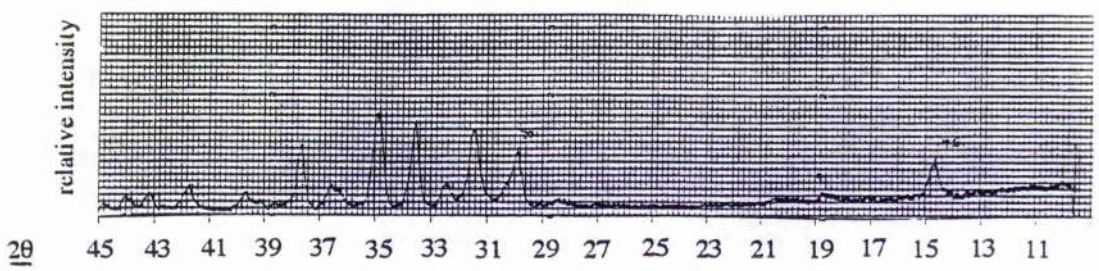

Fig. 4-15. Powder pattern of $K_{1+x}Fe_{11}O_{17}$.

A paper which deals with problems concerning the union of potassium ferrite and K-BASE can be found by consulting reference [60]. In this work by Dudley and Steele, attempts were made at hot pressing potassium ferrite and K-BASE between temperatures of 1150°C and 1250°C. These attempts invariably led to cracking at the interface which often resulted in destruction of the entire assembly due to contraction of the ferrite with respect to the K-BASE since the materials have different thermal expansion coefficients. The paper also shows that when K-BASE is hotpressed onto an equimolar solid solution of the ferrite and K-BASE there is a reasonably smooth transition from one phase to the other without any cracks.

Fortunately the method which was used to create the interface for the potassium source did not lead to as many problems. In order to prepare the source, 0.3 g of K-BASE powder was placed inside a 13mm die and pressed manually with the plunger before adding 6 drops of acetone which functioned as a binder. 0.4 g of potassium ferrite was then added on top of the K-BASE and both powders were pressed with a weight of 1 ton for a few minutes. The resulting composite pellet was then placed with its ferrite side down in a gold boat which had previously been lined with potassium ferrite. Each pellet inside the boat was covered with K-BASE powder and sintering was carried out in a programmable tube furnace by heating the cells from 25°C to 1000°C and back to 25°C at a rate of 4°C min^{-1} in an oxygen atmosphere to prevent iron reduction within the ferrite.

The cell is illustrated in Fig. 4-16. On removal from the furnace a thin circular layer of silver paint was applied to the ferrite side of each pellet to act as a current collector. A circular piece of stainless steel gauze was rubbed with emery paper, boiled in distilled water and dried with a heat gun before being placed on the electrolyte surface prior to the following LIMA and SEM experiments. Details of the LIMA experiment can be found in the preceding section.

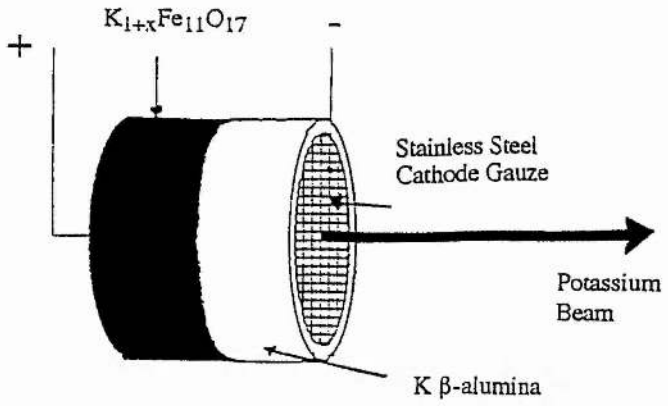

Fig. 4-16. Potassium source.

Before being placed in the cell holder the disk was polished with diamond paste and rinsed with deionised water. An initial LIMA spectrum was recorded from the disk prior to experiment in order to ensure that this cleaning procedure had been successful in eradicating traces of any unwanted elements. Figure 4-17 shows a typical LIMA spectrum of the disk after cleaning.

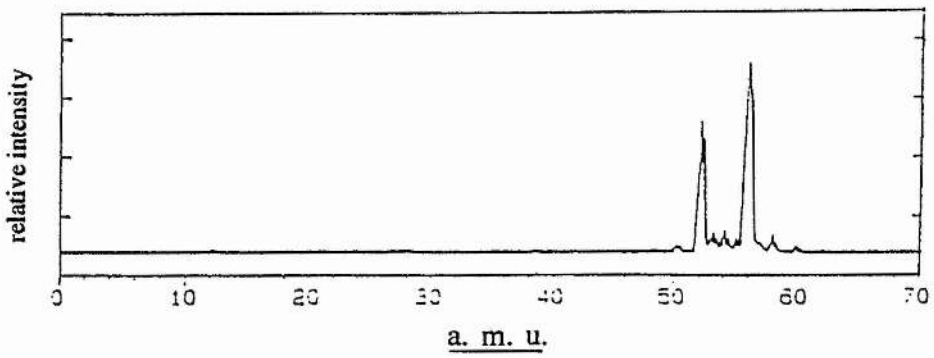

Fig. 4-17. LIMA spectrum of the stainless steel disk after cleaning.

The cluster of peaks between mass to charge numbers 50 to 60 corresponds to elements which comprise the stainless steel itself; the most notable being iron (m/z = 56) and chromium (m/z = 52). After polarising the cell with a potential of 10V at a temperature of 180°C for 48 h and repeating the experiment, peaks at m/z = 39

and 41 corresponding to the two isotopes of potassium were evident alongside the familiar family of peaks due to stainless steel (Fig. 4-18). The reason why the ^{39}K peak is split into two is due to signals from different regions of the rough potassium surface, as is frequently observed from rough surfaces.

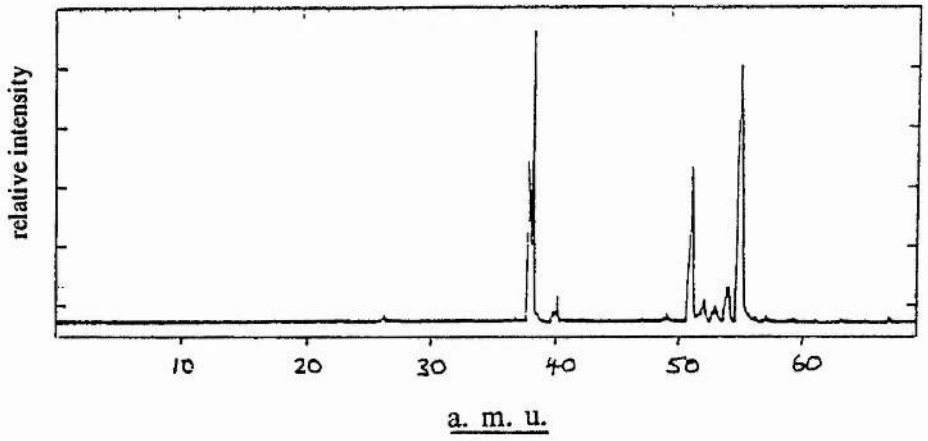

Fig. 4-18. LIMA spectrum of the stainless steel disk recorded after polarising the potassium source. The peak at m/z = 39 is due to potassium.

Carrying out a control experiment with the power switched off, the cell operating for the same length of time, and at the same temperature, indicated that no potassium was being evolved from the source simply as a result of the evaporation of potassium containing compounds from the surface of the K-BASE (Figs. 4-19 a) and b)).

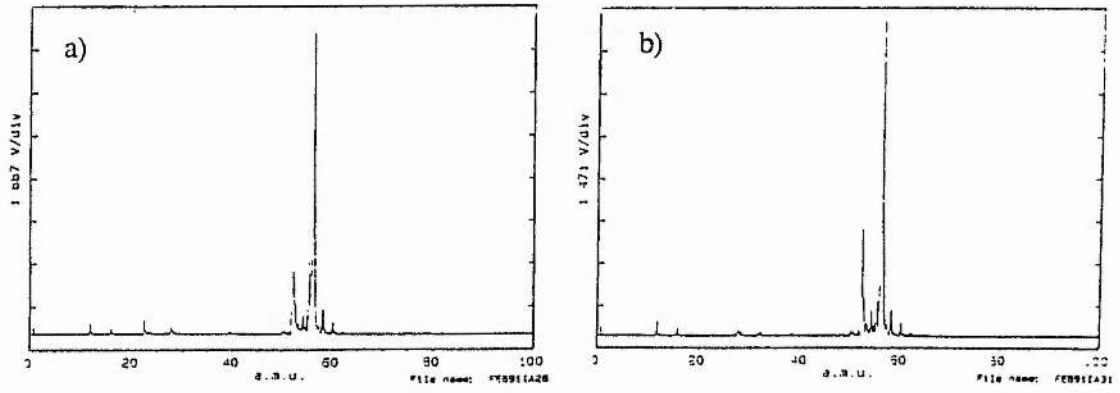

Fig. 4-19. a) LIMA spectrum of the stainless steel disk recorded before a control experiment with the potassium source. b) After the control experiment.

Additional peaks at m/z = 1, 12, 16 and 28 were thought to be due to hydrogen, carbon, oxygen and silicon contamination due to insufficient cleaning of the disk.

4.4 Cyclic Voltammetry with the K Source Operating at 10^{-3} mbar

The same procedure which was outlined at the start of section 4.2 was used to commence an investigation into the electrochemical mechanisms behind potassium evolution.

Unless otherwise stated, all measurements were made with the cell at a temperature of 350°C and a pressure of 10^{-3} mbar.

The cyclic voltammogram in Fig. 4-20 was recorded from 0 V to +5 V and back to 0 V with a scan rate of 200 mV/s. It indicates that there are no oxidation processes which occur up to +5 V vs. the reference potential. Applying a cathodic scan from 0 V to -10 V to 0 V followed by an anodic scan at a rate of 100 mV/s (Fig. 4-21) with the source operating under the same conditions showed that a nucleation loop was present at negative potentials. Similar to cyclic voltammetry results obtained with the previous source, this indicated the formation of potassium or potassium containing compounds on the stainless steel surface. A Coulombic efficiency of 0.59 indicated that 41% of the deposited potassium had been released into the gas phase at this scan rate.

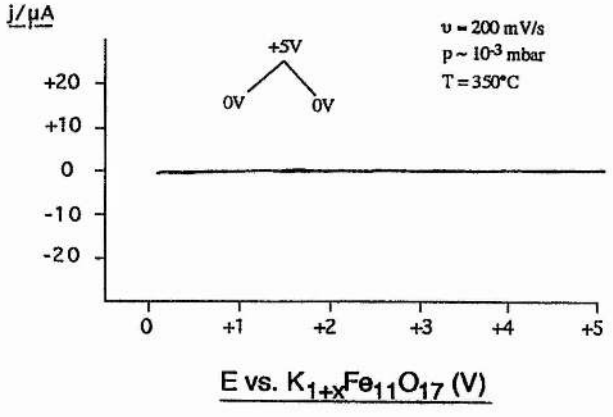

Fig. 4-20. A cyclic voltammogram of the K source recorded at anodic potentials.

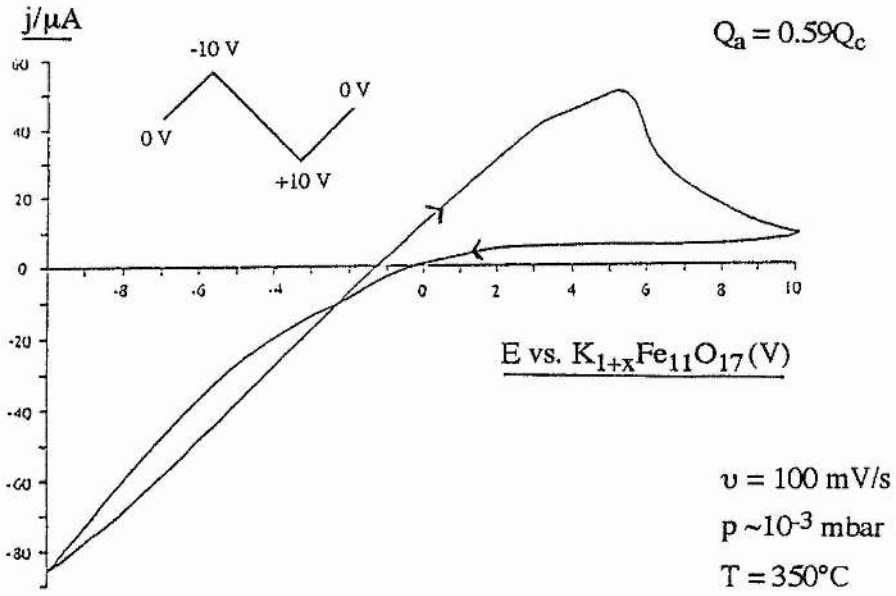

Fig. 4-21. Cyclic voltammogram showing the deposition and stripping of liquid potassium.

Figure 4-22 shows the effect of repetitive scanning in the cathodic direction. The nucleation loop becomes less well pronounced since potassium is now being deposited on itself and not on clean stainless steel; therefore less nucleation is taking place and so values of cathodic current on the reverse sweep become similar to those on the forward sweep.

Now, provided that pure potassium is being produced on the stainless steel, it is to be expected that the effect of decreasing the scan rate should result in diminished anodic waves (or lower Coulombic efficiencies) since more time is available for the potassium to evaporate.

This reasoning was tested by repeating the cyclic voltammetry experiment three times (each time with a clean gauze) with decreasing sweep rates. The results are presented in table 4-2 and verify this prediction.

Table 4-2.

Scan rate / mVs^{-1}	Coulombic efficiency (Q_a/Q_c)	% of deposit which evaporated
1	0.61	39%
10	0.63	37%
200	0.70	30%

The fact that it was impossible to remove the potassium even at sweep rates as low as 1 mV/s suggests that a following chemical reaction was taking place after K^+ reduction i.e. an EC mechanism was being observed. Possible following chemical reactions may be the formation of potassium oxide or potassium carbonate.

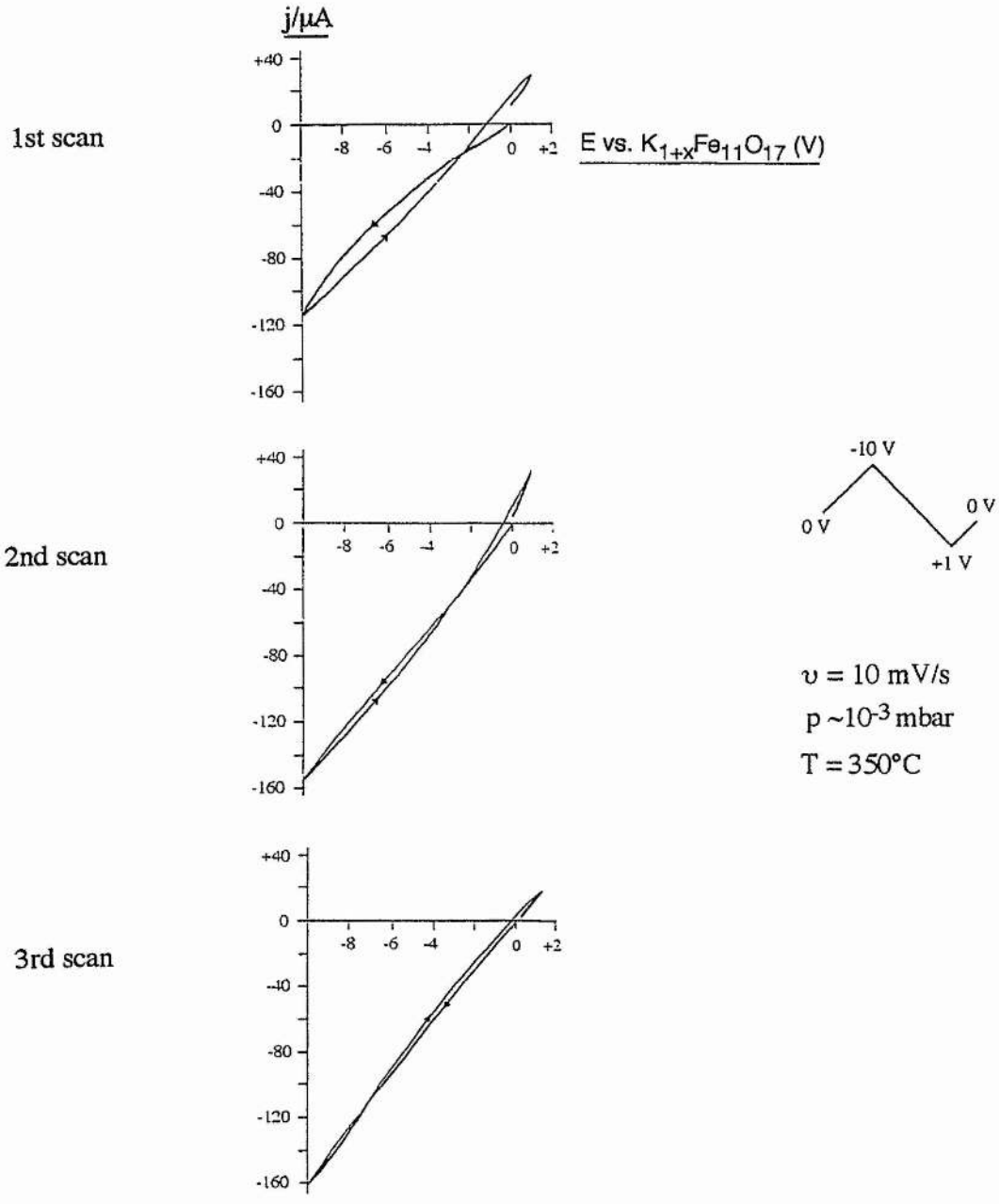

Fig. 4-22. Repetitive scans in the cathodic direction showing a reduction in size of the nucleation loop.

4.5 Manufacture and Operation of the Na Sources

Two attempts were made at building this source. The first involved making one which was directly analogous to the potassium source with sodium ferrite as the intercalation material and sodium aluminate as the solid electrolyte. This did not work for reasons dealt with below, but by using sodium cobalt oxide as an intercalation electrode instead, the source was found to operate efficiently.

a) "Sodium Ferrite" Source

Exactly the same method was used for the manufacture of this cell (Fig. 4-23) as has previously been outlined in section 4.3 except Na-BASE was used as the electrolyte and sodium ferrite as the anode.

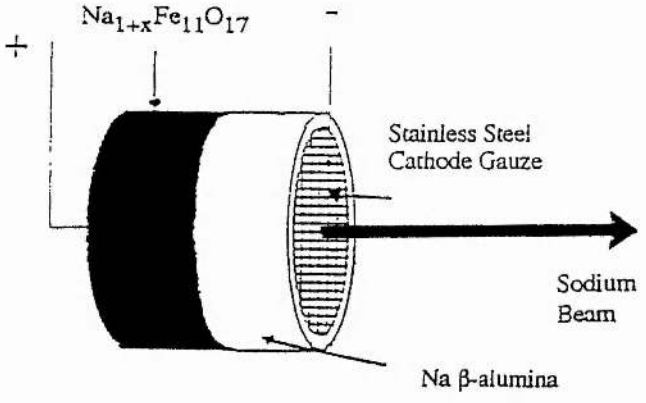

Fig. 4-23. "Sodium ferrite" source.

b) "Sodium Cobalt Oxide" Source

An X-ray powder pattern obtained from a sample of the sodium cobalt oxide prepared by the method outlined in chapter 2 is presented in Fig. 4-24a alongside data from ASTM 32-1068 which represents material of composition $Na_{0.75}CoO_2$ (Fig. 4-24b).

All expected reflections were present in the prepared material but it was also noted that the pattern contained additional peaks occurring at 2θ values: 31.5°; 32.5°; 42.8°; and 45.0°. These were thought to be due to other phases of sodium cobalt oxide being present in the reaction mixture [61].

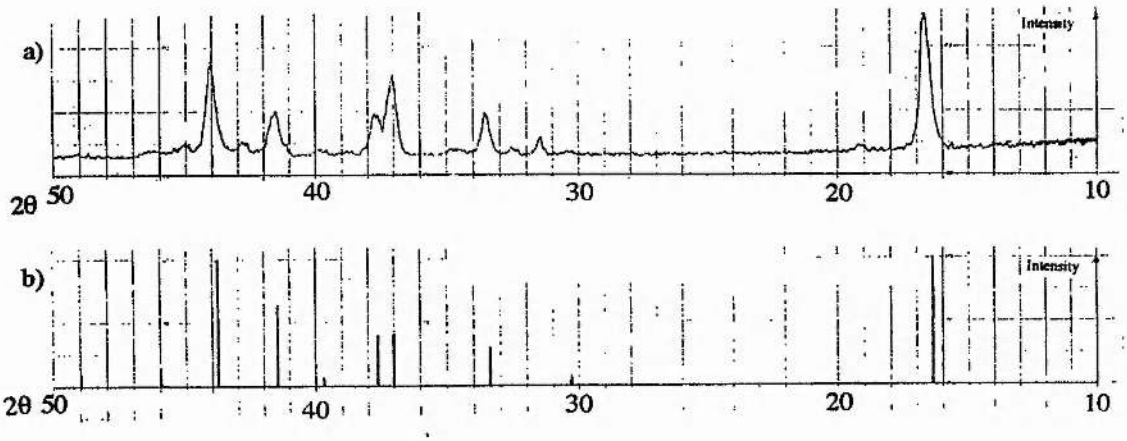

Fig. 4-24. a) A powder pattern of prepared $Na_{1-x}CoO_2$. b) Data from ASTM 32-1068.

Figure 4-25 is an XRD pattern of the Na-BASE. According to previous data [62] the prepared material is composed predominantly of the β" polymorph.

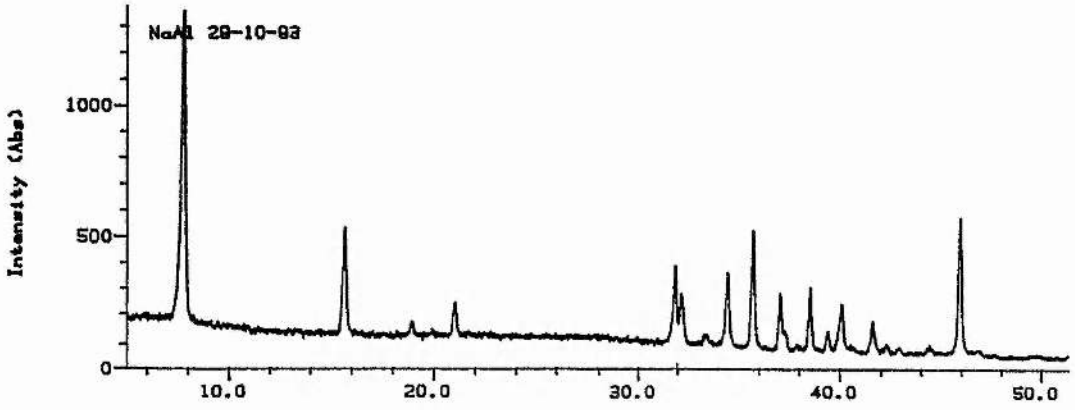

Fig. 4-25. Powder pattern of Na-BASE.

The cell (shown in Fig. 4-26) was prepared as follows. 0.75g of sodium cobalt oxide was placed in a 13mm die and gently compacted with the plunger by hand.

drops of acetone were then used to moisten the surface of the powder before adding 0.3g of Na-BASE and pressing the two materials together with a weight of 1 ton for a few minutes. The composite pellet was placed in a gold boat lined with Na-BASE powder and covered with sodium cobalt oxide before placing the boat in a silica tube fitted with taps which allowed the passage of oxygen as the temperature of the silica tube was: raised from 25°C to 500°C at a rate of 4°C min^{-1}; left at this temperature for 17 hours; and then cooled back to 25°C once again at 4°C min^{-1}. This sintering process was carried out with the silica tube inserted in a tube furnace. The cell was sintered in an oxygen atmosphere to prevent the reduction of cobalt within the sodium cobalt oxide. On removal from the silica tube the base of the pellet's sodium cobalt oxide side was painted with conductive silver paint to act as a current collector.

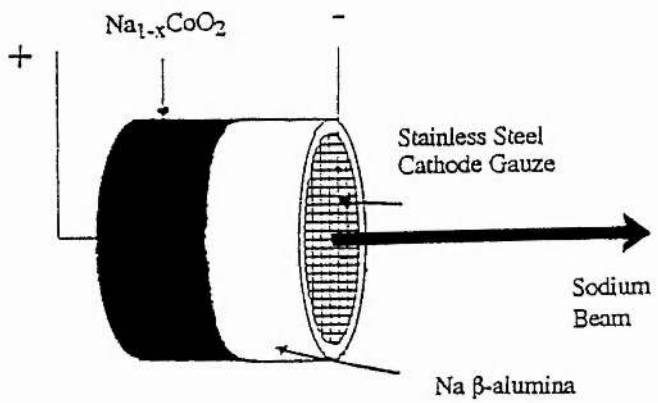

Fig. 4-26. "Sodium cobalt oxide" source.

The LIMA experiment outlined in section 4.1 was used to check if each cell was capable of producing sodium vapour. Table 4-3 lists the conditions under which each cell was operated.

Table 4-3.

Conditions	Cell Type	
	"sodium ferrite"	"sodium cobalt oxide"
Temperature (°C)	180	250
Voltage (V)	10	10
Duration of Polarisation	48 hrs	24 hrs
Chamber Pressure (mbar)	10^{-3}	10^{-3}
Current (μA)*	0.3	123

* The values of current correspond to those observed on ceasing polarisation of the cell.

Figure 4-27a and b represent the surface composition of the stainless steel disk before and after polarising the "sodium ferrite" source respectively.

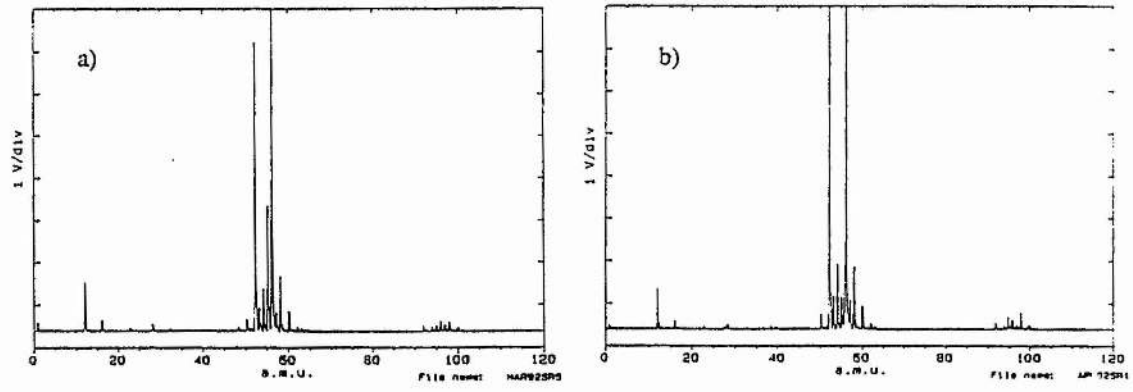

Fig. 4-27. a) LIMA spectrum taken from the surface of the stainless steel disk before polarising the "sodium ferrite" source. b) After polarisation.

Additional peaks at m/z = 1, 12 and 16 were due to hydrogen, carbon and oxygen respectively. These elements were thought to have originated from the diamond paste which was used to initially clean the disks. The cluster of peaks located between a.m.u. numbers 90-100 represented molybdenum which was also

thought to have arisen from the paste. More importantly, it was noted that there were no signs of any sodium production during its operation.

LIMA spectra which correspond to the "sodium cobalt oxide" source again, before and after polarisation, are shown in Figs. 4-28a and b respectively. This time the presence of sodium confirmed that the cell had evolved Na vapour which had then deposited on the stainless steel. The peak due to sodium is split in two due to signals from different regions of the rough sodium surface.

A control experiment, carried out under identical conditions, except that the potential difference was not applied, indicated no sodium evolution (Figs. 4-28c and d).

The fact that the "sodium ferrite" source was incapable of producing sodium stemmed from technical problems associated with X-ray diffraction apparatus which meant that the material which was presumed to be sodium ferrite was unable to be analysed. This caused the author to continue with the experiment based on the assumption that the sodium ferrite was indeed analogous in terms of structure and properties to potassium ferrite. Shortly after the LIMA results had been obtained, XRD apparatus became available and a powder pattern of the material indicated that it was composed predominantly of unreacted iron oxide. Figures 4-29a and b show powder patterns of "sodium ferrite" and Fe_2O_3 respectively.

A brief literature search was then carried out which showed that although attempts had been made to synthesise sodium ferrite, no success had been reported [63].

Although the construction of this cell was largely regarded as a waste of time, the fact it is incapable of releasing sodium provides evidence that the deintercalation of Na^+ from an intercalation anode is a requirement before production of Na vapour can ensue.

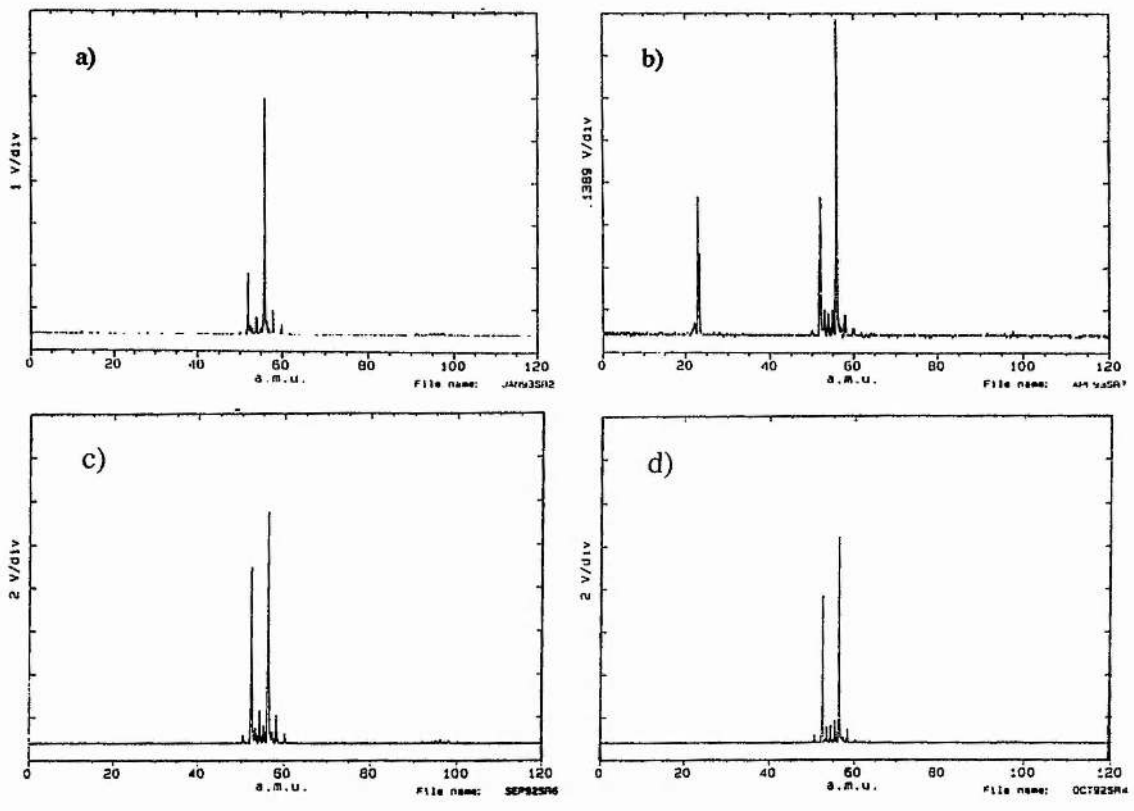

Fig. 4-28. a) LIMA spectrum taken from the surface of the stainless steel disk before polarising the "sodium cobalt oxide" source. b) After polarisation. c) Before carrying out a control experiment. d) After the control experiment.

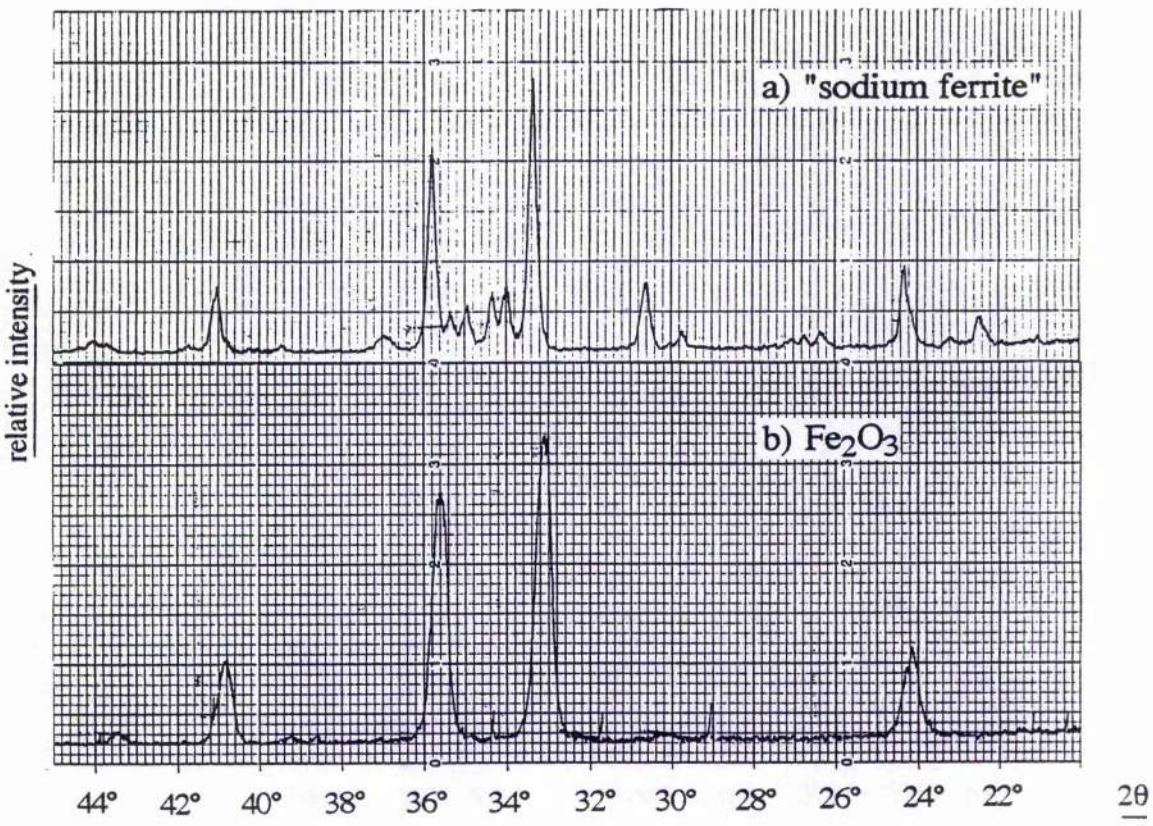

Fig. 4-29. a) Powder pattern of what was originally thought to be sodium ferrite. b) Powder pattern of Fe_2O_3.

4.6 Summary

This chapter has shown that it is possible to fabricate all solid state electrochemical cells which can emit lithium, sodium and potassium. These sources allow electrochemical measurements to be made which have provided information regarding the mechanisms behind which alkali metal evolution proceeds.

Difficulties were encountered during construction of the Li source. These were due firstly to problems associated with the intercalation electrode/solid electrolyte interface and secondly to the performance of the solid electrolyte, lithium germanium vanadate, when polarised. The former problem was solved by grading the interface whilst the later was avoided by replacing lithium germanium vanadate with lithium phosphosilicate. Electrochemical data concerning the Li source pointed towards a mechanism involving initial nucleation and growth of lithium on the cathode surface followed by its evaporation.

Unlike the Li source, graded interfaces did not need to be employed in order to construct potassium and sodium sources.

Electrochemical measurements made on the potassium source showed that, like lithium, the cell reaction involved initial nucleation and growth of potassium followed by its evaporation. Carrying out cyclic voltammetry experiments with varying sweep rates indicated that an EC mechanism was occurring at 10^{-3} mbar.

The following chapter contrasts the electrochemical measurements in this chapter with ones obtained in ultra-high vacuum. It also provides an in-depth analysis of the performance of the sodium source both at 10^{-3} mbar and in UHV.

Chapter 5

Cell Mechanisms: Electrochemistry 2

5.1 Introduction

This chapter gives a more detailed examination of electrochemical evolution of alkali metals. It begins with a brief investigation of potassium and lithium emission before providing a more comprehensive account of sodium production. The main reason for deciding to focus on sodium production was because, unlike potassium and lithium sources, the sodium source was not used as a precursor for semiconductor growth during this work and is therefore not dealt with in chapter six. Also, there is a great wealth of literature which deals with the Na-BASE/electrode interface and the sodium sources were comparatively easy to prepare.

Data recorded from all three sources at ~10^{-3} mbar are compared and contrasted with that obtained in UHV (~10^{-8} mbar) and the vast majority of it is concerned with the solid electrolyte/*stainless steel*/vacuum interphase; the remainder being a brief acknowledgement of Na-BASE/*platinum*/vacuum. Stainless steel is essentially an alloy of iron and chromium, but also contains trace amounts of Mo, Mn, V, Ni, Si and C. Ever since the first intentional alloying of iron with chromium in 1821 by Berthier [64], stainless steel has been used widely in the construction of items ranging from kitchen utensils to jet engines. The reason for its popularity is its corrosion resistance which is a result of a passive film on its surface. Although there is some dispute concerning the nature of this passive film [65] it is generally accepted that it is composed of oxygen.

There are many ways of envisaging the release of alkali metals from the sources. The atoms may be transferred into the gas phase directly or they may coalesce on the stainless steel surface to form nucleation points which in turn evaporate. In the later case the mechanism for nucleation could for example be: two dimensional; surface diffusion controlled; progressive, or instantaneous. The mechanism may also involve the chemisorption or physisorption of atoms on the stainless steel surface. There is also the possibility that an alloy may form with the metal substrate since according to reference [66], small amounts of sodium can dissolve in iron at 350°C. Finally, at higher pressures, the presence of oxygen and carbon dioxide in the chamber could

result in the initial formation of an alkali metal oxide or carbonate which could then decompose to produce the alkali metals.

5.2 Electrochemical Measurements on K and Li Sources

The three electrode cell shown in Fig. 2-2 was used in conjunction with the UHV apparatus shown in Fig. 2-3 to obtain the following results.

1) K Source

Cyclic Voltammetry

The three electrode cell was left to equilibrate in the UHV chamber at 350°C and ~10^{-8} mbar for 24 hrs.. The first sweep from 0 V to -4 V to +4 V and back to 0 V showed that unlike the result discussed in section 4.4 where the source was operating at the higher pressure of 10^{-3} mbar, a nucleation loop in the cathodic region was not observed. Instead, there was a linear variation of current with overpotential at relatively high cathodic values. Subsequent sweeps were found to be identical to that shown in Fig. 5-1. This suggested that only the iR drop of the K-BASE between reference and working electrodes was contributing to the impedance of current flow. A Coulombic efficiency of 0.16 indicated that 84% of the potassium that was produced had evolved into the gas phase - considerably more than that at 10^{-3} mbar.

The equilibrium potential is defined as the voltage corresponding to zero current on the reverse cathodic sweep i.e. -1.5 V. It should be noted that on the initial cathodic sweep and at voltages more positive than the equilibrium potential a significant current (~5 μA) is flowing through the cell. This may be due to underpotential deposition (upd) since on sweeping cathodically the initial formation of submonolayers and monolayers of potassium may occur. Why this process should happen at potentials positive from the equilibrium potential (the underpotential range) can be explained by considering a quasi Nernst equation,

$$E = E^{o} + (RT/nF)\ln(a_{ox}/a(\Gamma)) \qquad (5\text{-}1)$$

Where $a(\Gamma)$ is the activity of the potassium adsorbate which is less than unity and varies with surface coverage since $E>E_e$ [67]. This means that potentials more positive than E_e correspond to K-adsorbate formation which in turn explains the observable current.

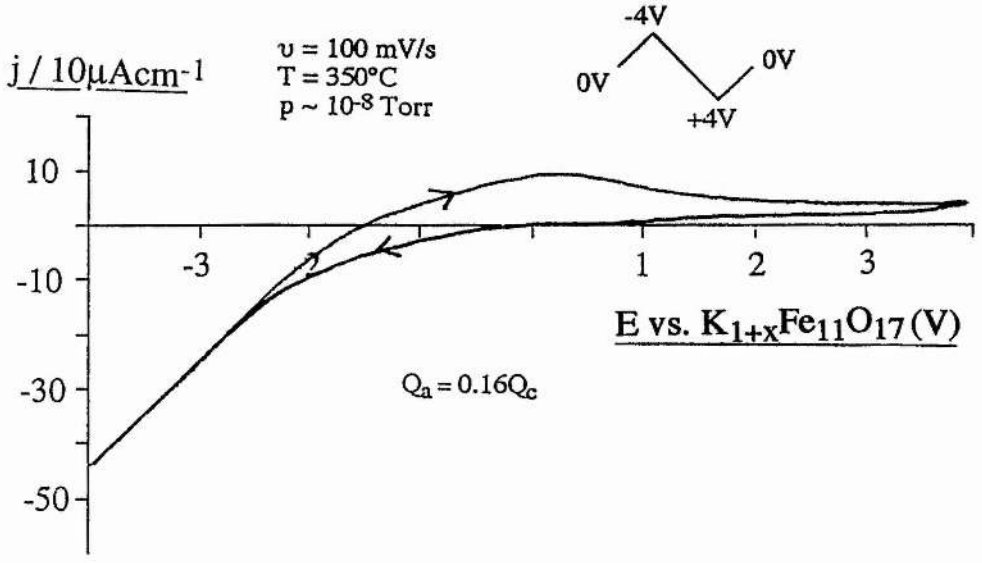

Fig. 5-1. Cyclic voltammogram of the potassium source in UHV. It shows a linear variation of current with cathodic potentials where potassium is produced.

Chronoamperometry

Fig. 5-2 shows current-time responses of the source after stepping the potential from +2.0 V to cathodic potentials vs. the reference potential with the cell operating in a vacuum of 10^{-3} mbar and at a temperature of 350°C. Two aspects should be noted here; at very short times the current rises and falls due to double layer charging effects and at longer times the current rises sharply. The general shape of this graph is consistent with a process involving nucleation and growth of discrete centres of a new metallic phase.

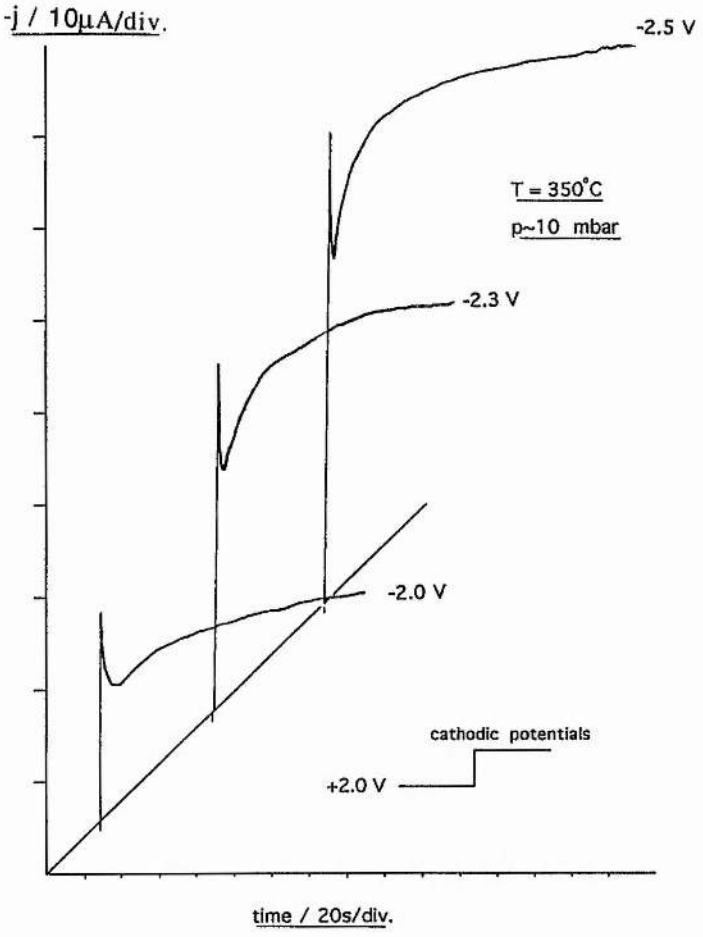

Fig. 5-2. Current-time transients recorded with the potassium source operating at 10^{-3} mbar. The rising parts represent the formation of liquid potassium or potassium containing compounds on the stainless steel gauze surface.

Repeating this experiment with the source operating in UHV (~10^{-8} mbar) provided the j-t traces shown in Fig. 5-3. This time there was no observed increase of current with time which provided proof that nucleation was no longer a rate controlling step. Unlike the experiments carried out at 10^{-3} mbar, each of these j-t transients contained intermittent spikes. The periodic nature of these spikes suggests that they may have been due to instrumental problems.

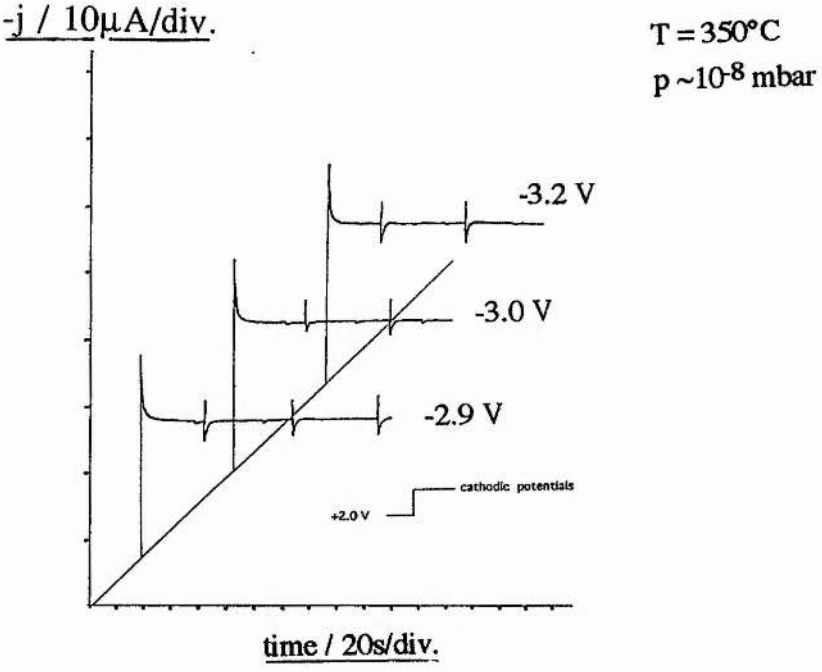

Fig. 5-3. Current-time responses of the potassium source in UHV to voltage pulses from +2.0 V to various cathodic potentials.

AC Impedance

A complex impedance plane plot recorded at -2.5 V vs. $K_{1+x}Fe_{11}O_{17}$ with a signal amplitude of 50 mV is shown in Fig. 5-4. During this experiment the cell was maintained at 10^{-3} mbar and 350°C. The complex impedance defined a semicircle at high frequencies and an inductive shape at low frequencies.

By using theory outlined in chapter 3 a value of capacitance was assigned to the high frequency semicircle. This value, 4.46 nF, was too low to be attributed to a double layer process since capacitances of the electrical double layer have values in the μF domain. Equation 5-2 shows that capacitance is related inversely to the length of separation of the plates of the capacitor (l).

$$C = \varepsilon\varepsilon_0 A/l \qquad (5\text{-}2)$$

The area of contact of the working electrode with the K-BASE surface (A) was estimated to be approximately 0.14 cm^2 and $\varepsilon\varepsilon_0$ was taken to be ~10^{-14} Fcm^{-1}. Using this expression to calculate the value of l from the measured capacitance gave 3.1 x 10^{-7} cm which was too large to be associated with the double layer.

A length of 3.1 x 10^{-7} cm is more likely to be due to the separation (grain boundaries) of particles comprising the solid electrolyte between reference and counter electrodes. The intercept of the semicircle with the Z' axis was assumed to be the grain boundary resistance and had a value of 120 kΩ. This was comparable with previous results obtained from two electrode measurements on a sintered pellet of K-BASE [68].

Having the presence of an inductive shape was consistent with a theoretical axiom by Armstrong and Metcalfe [69] for rate determining two dimensional nucleation and growth. In this paper a Fourier transform of a potentiostatic transient was used to obtain the impedance.

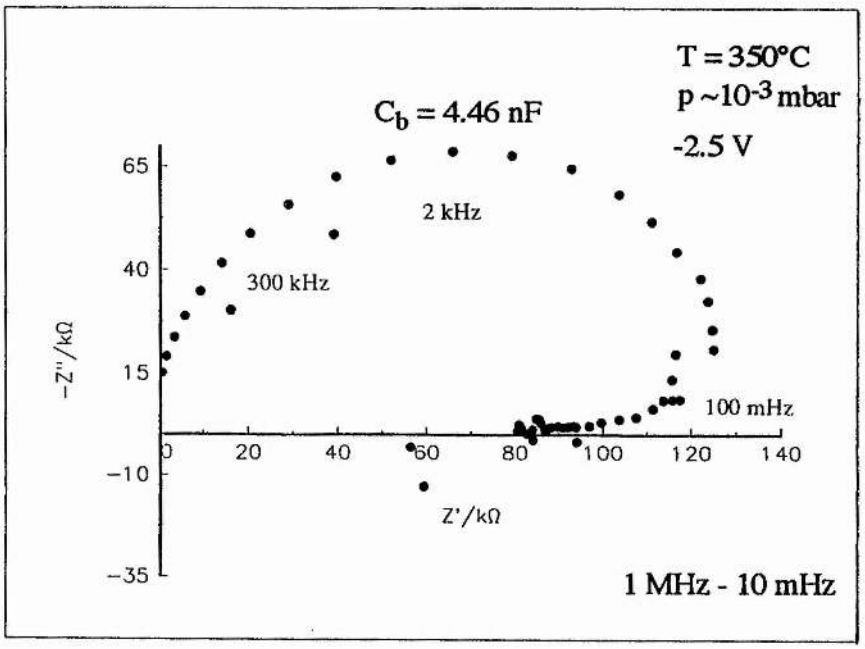

Fig. 5-4. AC impedance data from the potassium source operating at 10^{-3} mbar and at a relatively high cathodic potential.

2) Li Source

Cyclic Voltammetry

After equilibration for 24 hrs. at 350°C and ~10^{-7} mbar (UHV) the stainless steel gauze working electrode of the lithium source was swept from 0 V to cathodic potentials and back to anodic potentials. The first sweep is shown in Fig. 5-5. It shows a nucleation loop and has the same features as recorded during subsequent sweeps. Like the lithium cyclic voltammetry result at 10^{-3} mbar (Fig. 4-13), but unlike the potassium cyclic voltammetry result in UHV (Fig. 5-1), the nucleation and growth of lithium represented a rate limiting step. By consulting reference [70] it was found that liquid lithium has a vapour pressure which is three orders of magnitude lower than liquid potassium. This helps to rationalise the fact that lithium nucleation is still observed when the source is operating in UHV whereas potassium nucleation is not.

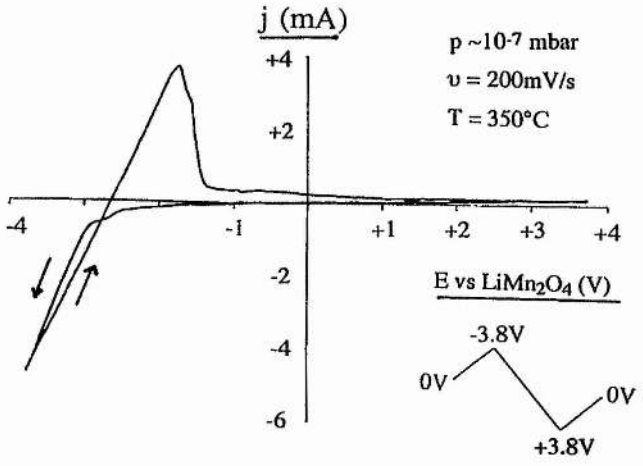

Fig. 5-5. Cyclic voltammogram of the lithium source in UHV showing a nucleation loop.

Chronoamperometry

At 10^{-3} mbar a rising current-time transient (Fig. 5-6), obtained after stepping the potential of the gauze from +2.0 V to -3.5 V, provided further evidence for phase formation on the stainless steel gauze surface.

At 10^{-7} mbar (UHV) and 350°C there is also an increase of current with time once the voltage has been stepped from +2 V to -2.5 V (Fig. 5-7) which once again indicates nucleation and growth as well as complementing the observed nucleation loop on the cyclic voltammogram in Fig. 5-5. It should be noted that after initial double layer charging the current decays to reach a steady value of ~0.25 mA for approximately 10 s before the onset of phase formation. This has been observed before during studies of the electrodeposition of a single nucleus of mercury on carbon fibre [71]. When only one nucleus is being formed the falling charging transient and small nucleation growth current are separable thus giving rise to an induction time for nucleation to proceed. However, when (as in this case) multiple droplets are formed,

the nucleation current is finite from a time close to the onset of the pulse. Gunawardena *et al.* attribute the minima in this case to an overlap of both decaying charging current and nucleation growth current [72].

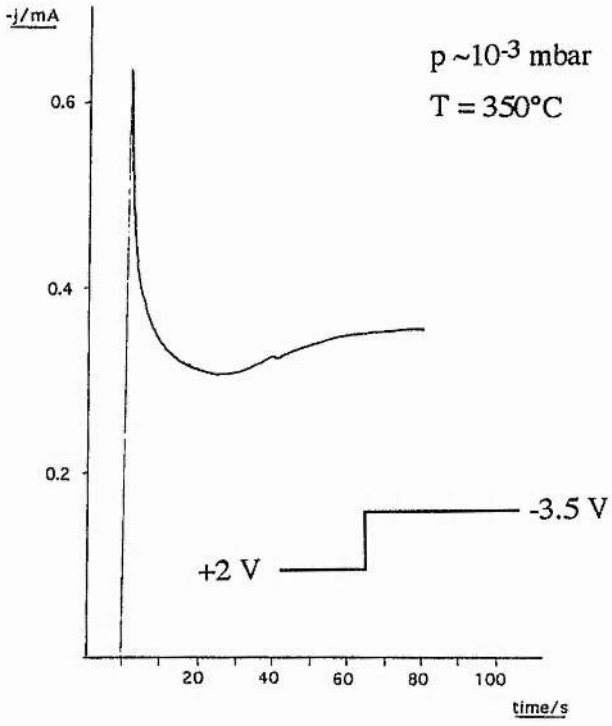

Fig. 5-6. A rising current-time transient recorded with the lithium source operating at 10^{-3} mbar. The rising part represents the formation of liquid lithium or lithium containing compounds on the stainless steel surface.

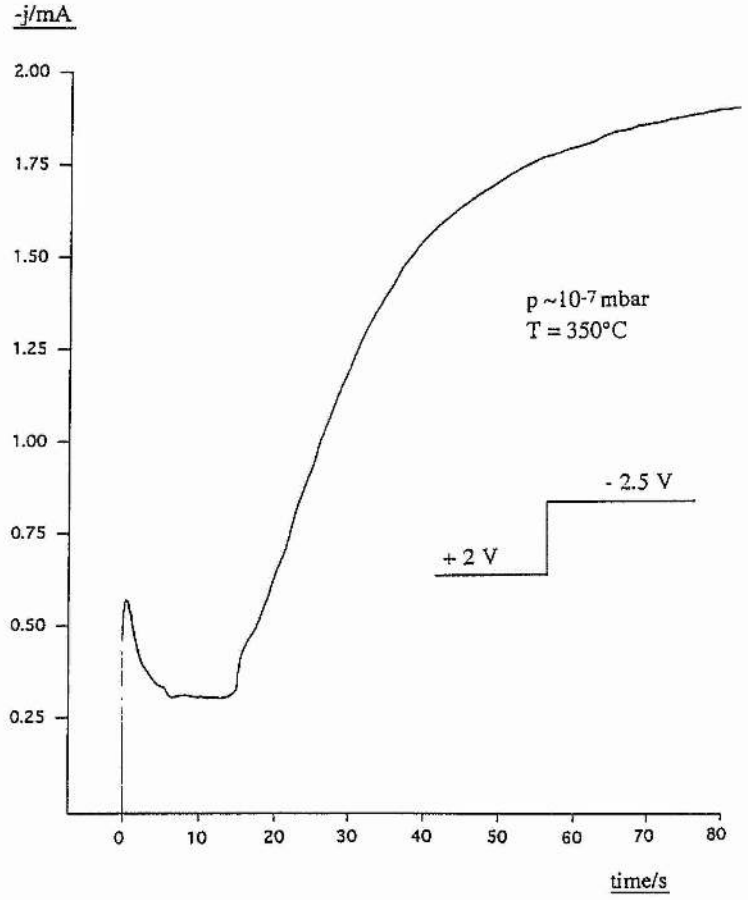

Fig. 5-7. j-t response of the lithium source in UHV to a potential step from +2.0 V to -2.5 V.

AC Impedance

A complex impedance plane plot recorded at -4.0 V vs. $LiMn_2O_4$ with a signal amplitude of 50 mV is shown in Fig. 5-8. During this experiment the cell was maintained at 10^{-3} mbar and 350°C. The complex impedance defined a semicircle at high frequencies and an inductive shape at low frequencies. By using the theory outlined in chapter 3 a value of capacitance was assigned to the high frequency semicircle. This value, 2.18 nF, was too low to be attributed to a double layer process therefore it was concluded that the high frequency semicircle represented grain boundary responses. The intercept of the semicircle with the Z' axis was taken to be the bulk electrolyte resistance and had a value of 750 Ω.

Like the potassium source, at low frequencies an inductive shape was found to be present which represented nucleation and growth.

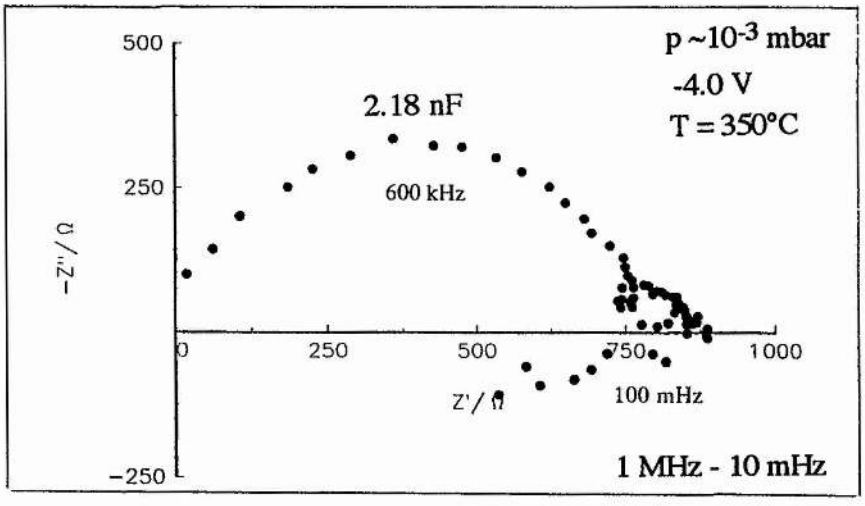

Fig. 5-8. AC impedance data from the lithium source operating at 10^{-3} mbar and at a relatively high cathodic potential.

5.3 Study of the Na-BASE/Metal Gauze/Vacuum Interface

1) Cyclic Voltammetry, Chronoamperometry and AC Impedance Experiments with the Na-BASE/Stainless Steel Interface at 10^{-3} mbar

Cyclic Voltammetry

The cyclic voltammogram in Fig. 5-9 was recorded with a scan rate of 200 mV/s from 0 V to +3.0 V with respect to $Na_{1-x}CoO_2$. It shows that no significant redox behaviour was observed.

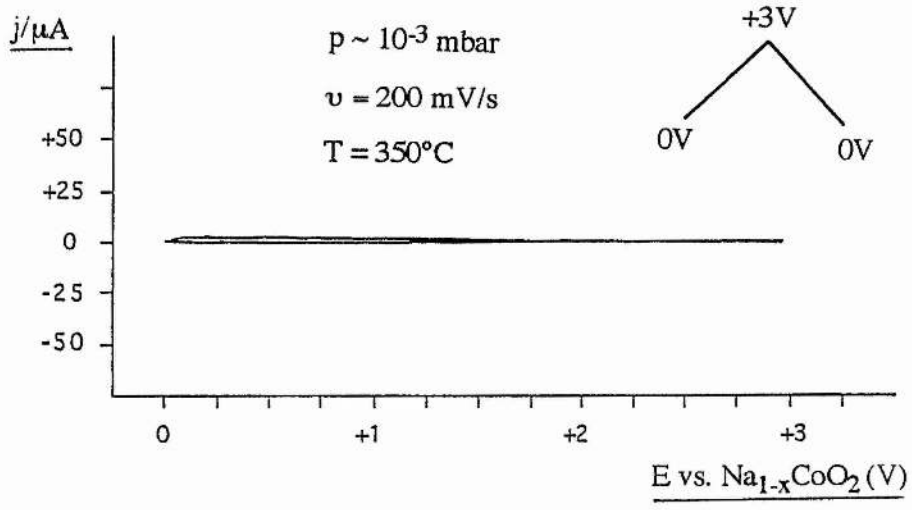

Fig. 5-9. A cyclic voltammogram of the Na source recorded at anodic potentials.

Starting at 0 V and applying a cathodic sweep to -3 V, followed by anodic sweep to +3 V at a rate of 100 mV/s (Fig. 5-10) showed that a nucleation loop was present at negative potentials. A Coulombic efficiency of 0.4 indicated that 40% of the deposited sodium had remained on the gauze. It was also observed that a significant

current, thought to be due to underpotential deposition of sodium, flowed prior to the equilibrium potential.

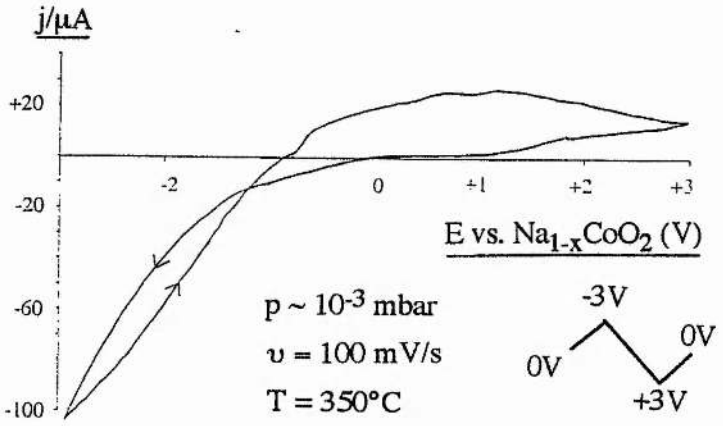

Fig. 5-10. Cyclic voltammogram showing the deposition and stripping of liquid sodium.

Repeating the cathodic scan (Fig. 5-11) showed a reduction in size of the nucleation loop which meant that less nucleation was taking place since this sodium was obviously being deposited on a sodium surface and not clean stainless steel.

Fig. 5-12 shows the effect of repeating scans at anodic potentials. Even after four sweeps the wave was still present. The fact that it was impossible to rid the gauze of sodium by repeated stripping suggested that a following chemical reaction had taken place; possibly the conversion of sodium to sodium oxide or sodium carbonate.

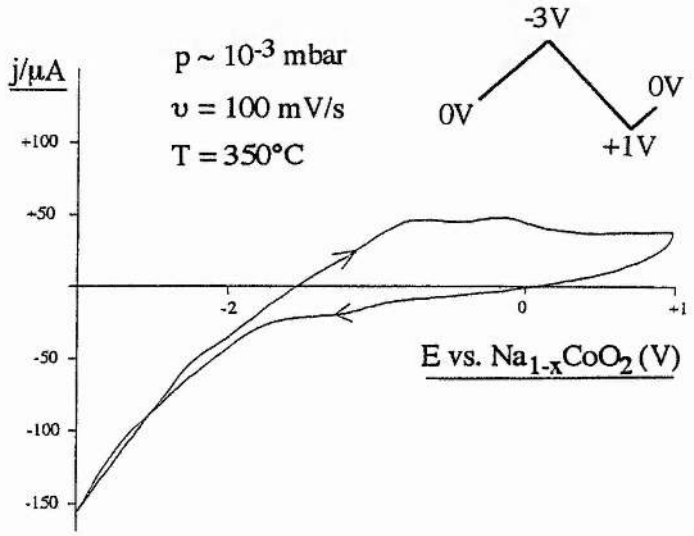

Fig. 5-11. A reduced nucleation loop recorded after the first scan.

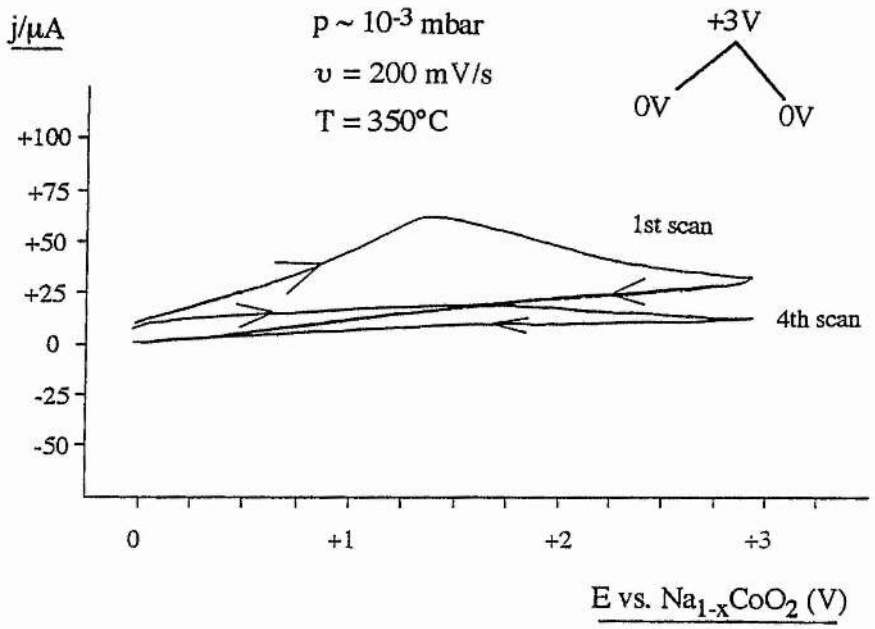

Fig. 5-12. The effect of repetitive scanning in the anodic direction after the production of sodium.

Chronoamperometry

The potential of the gauze was stepped from +2.0 V to -2.5 V and the current passing through the cell monitored as a function of time (Fig. 5-13). After initial double layer charging the current rose steeply with time which was further evidence that sodium was being produced by a nucleation and growth mechanism.

Attempts at fitting data like Fig. 5-13 to various models which represented possible shapes of the nucleation points were unsuccessful. This was not surprising since cyclic voltammetry had shown that sodium was being evaporated from the stainless steel surface after its production. Also, a possible following chemical reaction between sodium and oxygen would have complicated this analysis.

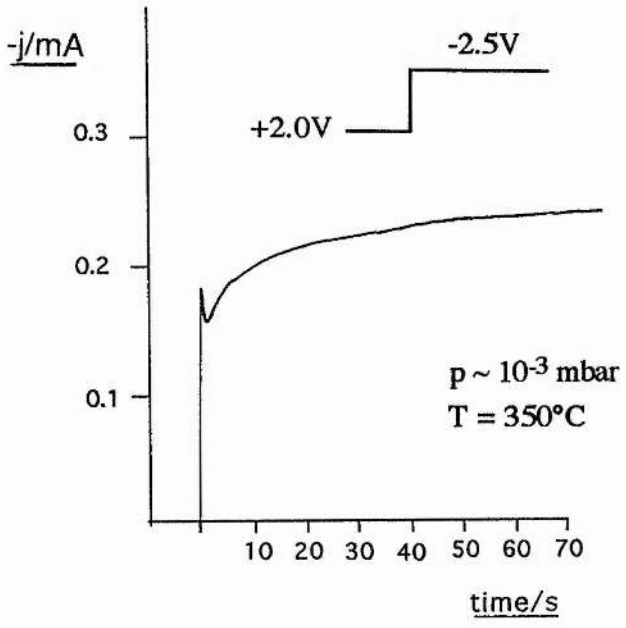

Fig. 5-13. A rising current-time transient recorded with the sodium source operating at 10^{-3} mbar. The rising part represents the formation of liquid sodium or sodium containing compounds on the stainless steel surface.

AC Impedance

Like the potassium source, ac impedance experiments at high overpotentials provided complex impedance plane plots which showed some evidence of inductive loops at low frequencies. This was further proof for a mechanism involving nucleation and growth [69]. Fig. 5-14 shows the result obtained when the source was operating at -2.5 V with respect to $Na_{1-x}CoO_2$.

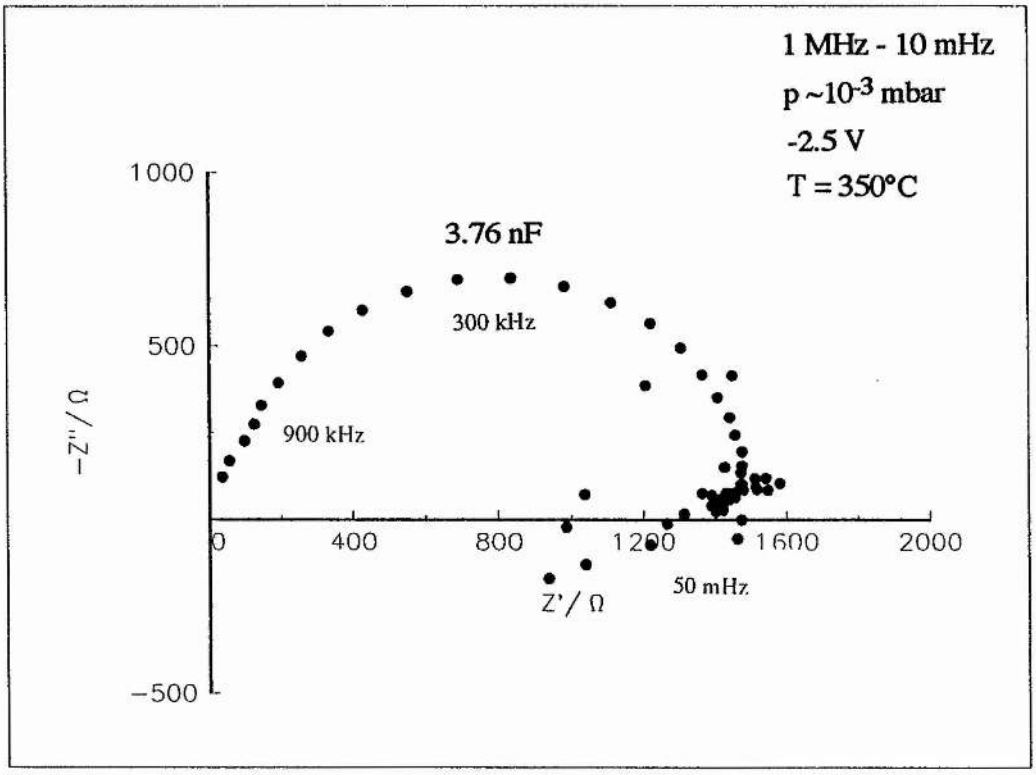

Fig. 5-14. Ac impedance data from the sodium source operating at 10^{-3} mbar and a relatively high cathodic potential.

2) Cyclic Voltammetry and Chronoamperometry Experiments with the Na-BASE/Stainless Steel Interface at 10^{-8} mbar

Cyclic Voltammetry

Fig. 5-15 shows that the source behaves quite differently in UHV. Instead of a nucleation loop in the cathodic region between -2.5 V and -3.0 V all that is observed is a linear variation of current with voltage which means that an ohmic relationship exists between them. This suggests that only the iR drop of the Na-BASE between reference and working electrodes is impeding the current. From this reasoning it seems fair to conclude that in this potential range no nucleation of sodium metal is occurring.

Like experiments carried out with the potassium source in UHV, significant underpotential deposition was also observed when this source was operated in UHV.

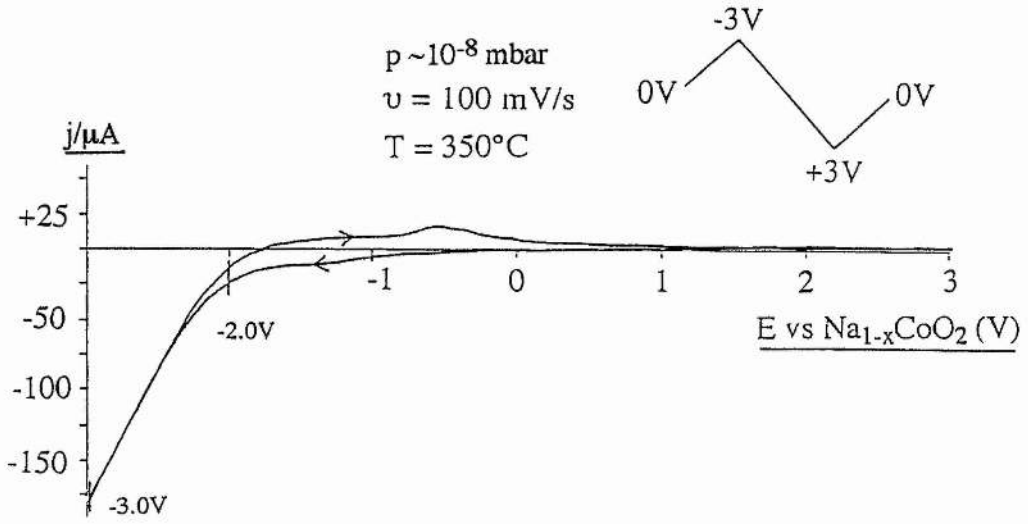

Fig. 5-15. Cyclic voltammogram of the sodium source recorded in UHV and showing that the nucleation loop observed at 10^{-3} mbar (Fig. 5-10) has been replaced with linear j-E behaviour.

Chronoamperometry

Fig. 5-16 shows results obtained when the potential was stepped from +2 V to a range of values located on the linear region of the cyclic voltammogram in Fig. 5-15. Unlike the result shown in Fig. 5-13, there was no observable rise in current due to nucleation of sodium metal. The current was found to maintain constant values whilst the cell was left at various potentials for three minutes each time. It should also be pointed out that unlike potential step experiments carried out with the potassium source in UHV (Fig. 5-3) no spikes were present.

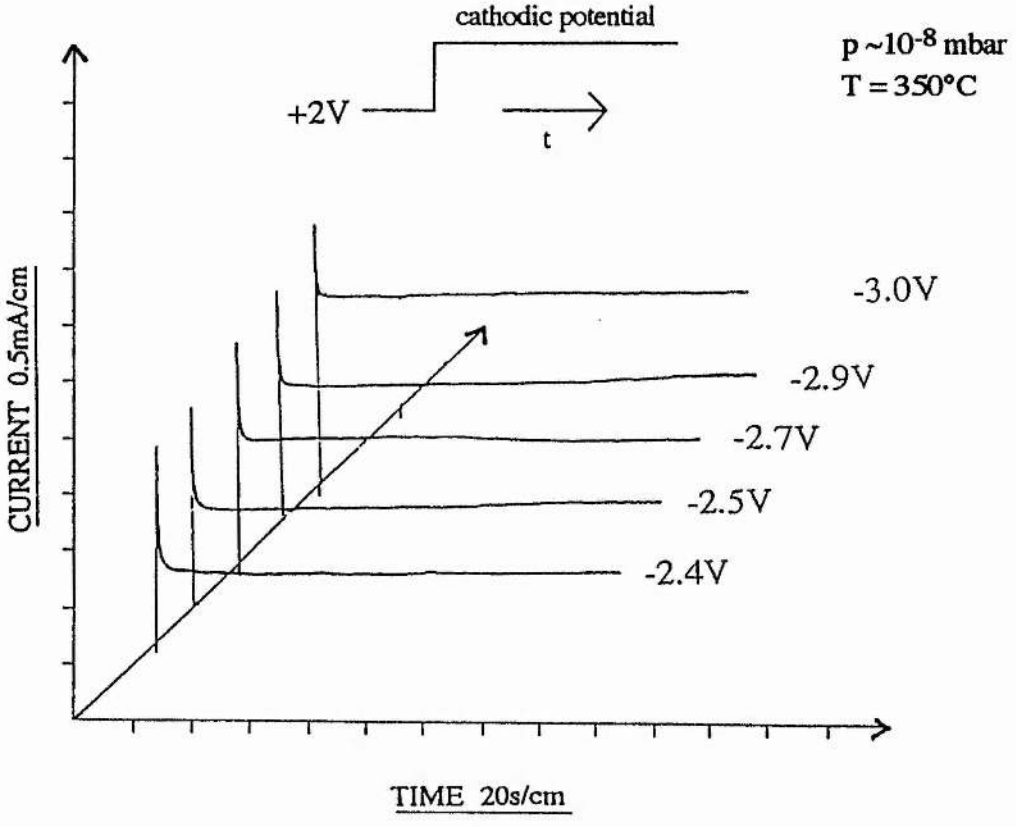

Fig. 5-16. Current-time transients from the sodium source in UHV when the potential of the working electrode is stepped from +2.0 V to cathodic potentials located on the linear region of the cyclic voltammogram in Fig. 5-15.

3) Cyclic Voltammetry Experiment with the Na-BASE/Platinum Interface at 10^{-8} mbar

Fig. 5-17 is a cyclic voltammogram of the source operating in UHV with a platinum gauze electrode used instead of stainless steel. It can be seen that the behaviour is very similar to that observed in Fig. 5-15, the only notable difference being considerably less underpotential deposition. This may suggest that it is the oxide layer on stainless steel which is responsible for monolayer/submonolayer formation of sodium since, when compared with stainless steel, platinum has less oxygen adsorbed on its surface [73].

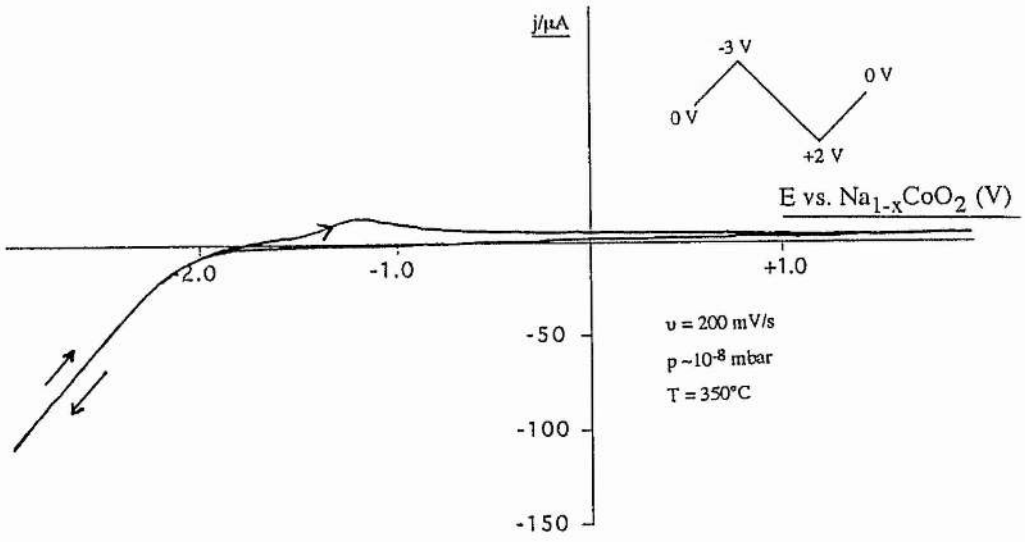

Fig. 5-17. Cyclic voltammogram of the sodium cell with a platinum working electrode.

4) AC Impedance Analysis of the Na-BASE/Stainless Steel Interface at 10^{-8} mbar

Carrying out ac impedance at a range of cathodic overpotentials prior to the linear region of the cyclic voltammogram in Fig. 5-15 yielded complex impedance plane plots consisting of two semicircles. Impedance plots for three potentials are shown in Fig. 5-19. Changing the DC potential influenced the size of the low frequency semicircle but not the high frequency semicircle. This suggested that the low frequency semicircles represented an interfacial process and that the high frequency semicircles represented bulk electrolyte responses.

The data could be modelled using the equivalent circuit shown in Fig. 5-18 and a computer programme written by MacDonald [74].

R_b and C_b are resistances and capacitances associated with the electrolyte whilst R_{ct} represents a resistance due to the interfacial process and C_{dl} represents the double layer capacitance.

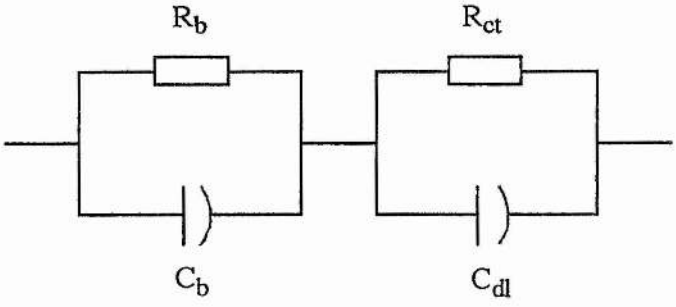

Fig. 5-18. The equivalent circuit which was used to represent the physical processes behind sodium production.

The appendix contains a representation of this circuit as used in the fitting program [75].

As outlined in chapter 3 the parallel combination of a resistor and a capacitor gives rise to a perfect semicircle on the complex impedance plane. Inspection of Fig. 5-19,

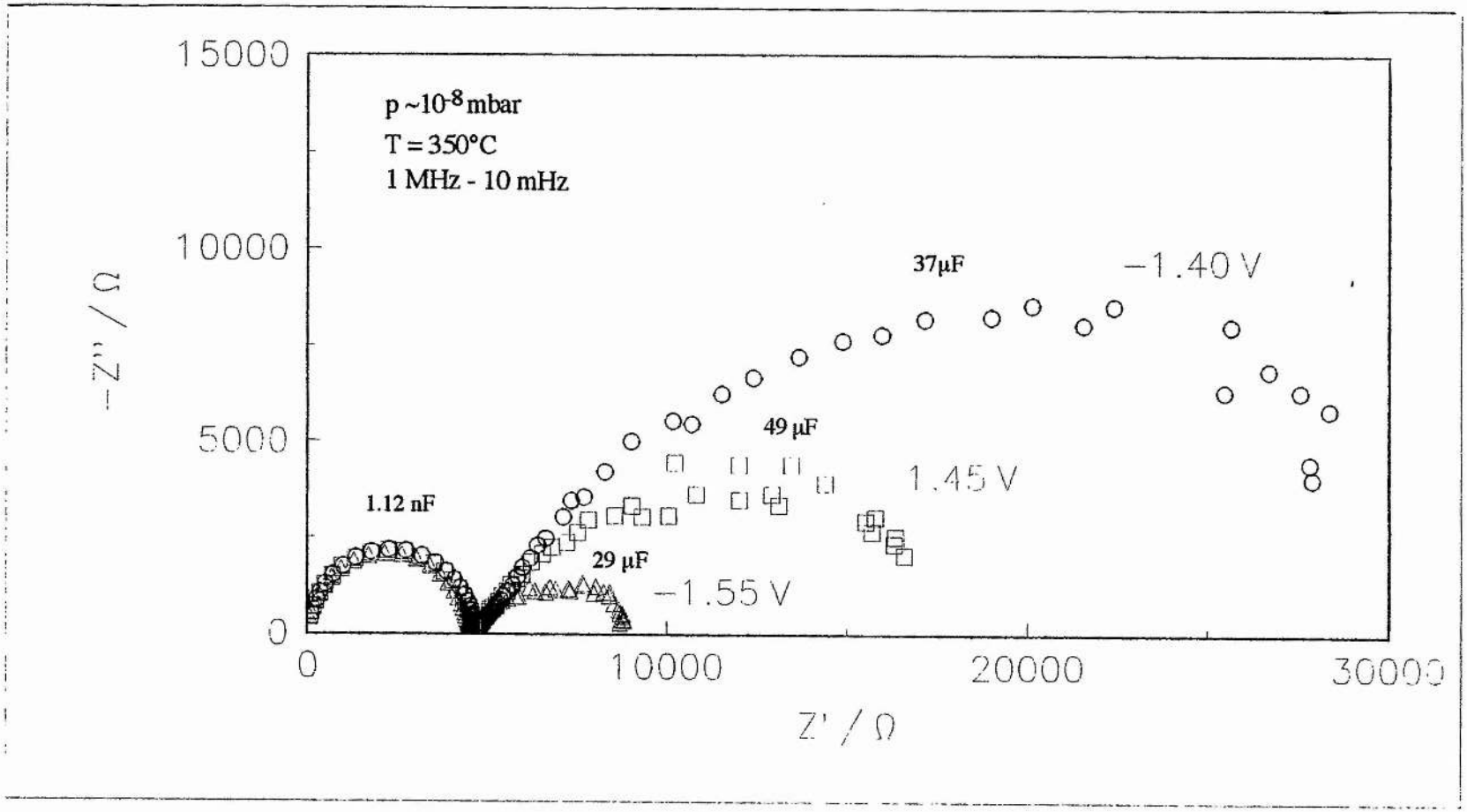

Fig. 5-19. Complex impedance plane plots from the sodium source in UHV. The potentials were measured vs. the $Na_{1-x}CoO_2$ reference electrode.

however, shows that both high and low frequency semicircles are broadened and distorted. This can be explained as follows:

Reason for distortion of high frequency semicircle

There are several reasons for distorted semicircles due to bulk electrolyte responses on the complex impedance plane. Previous ac impedance experiments carried out on single crystals of Na-BASE have led to semicircles on the complex impedance plane with centres which lie below the real axis [76, 77]. Such non-ideal response is only observed in single crystal electrolytes with a high concentration of mobile charges which supports the belief that the origin of this behaviour lies in co-operative interactions between mobile ions [78]. In polycrystalline systems, however, distorted semicircles may arise due to heterogeneity of the grain boundaries. Also, the high frequency semicircle on Fig. 5-19 may represent both grain boundary and bulk responses which are melded together. Such overlap of the two semicircles also leads to an overall distorted response.

Reason for distortion of low frequency semicircle

There are also several theories available which explain why semicircles on the complex impedance plane corresponding to *electrode processes* can be broadened and distorted [79]. The first was by de Levie [80] who calculated the effect of electrode surface roughness on impedance. A different approach was published in 1984 by Brug *et al.* [81]. In order to explain the distortion they state that semicircles representing ideal behaviour have to be rotated clockwise by an angle $\Psi = \alpha\pi/2$ (Fig. 5-20). This means that instead of the classical representation of the impedance of a capacitor, $Z_C = (i\omega C)^{-1}$ (as derived in chapter 3) which when combined with a parallel resistor leads to perfect semicircles on the complex impedance plane, a more complicated expression with the capacitor replaced by a constant phase angle element (CPE) has to be employed. The reason why this element (—|)— in Fig. 5-18) is

called a CPE is because the phase angle of the impedance of the CPE remains unchanged whilst the frequency of the voltage signal is varied.

The computer programme written in Fortran in the appendix represents CPEs for both electrolyte and electrode responses.

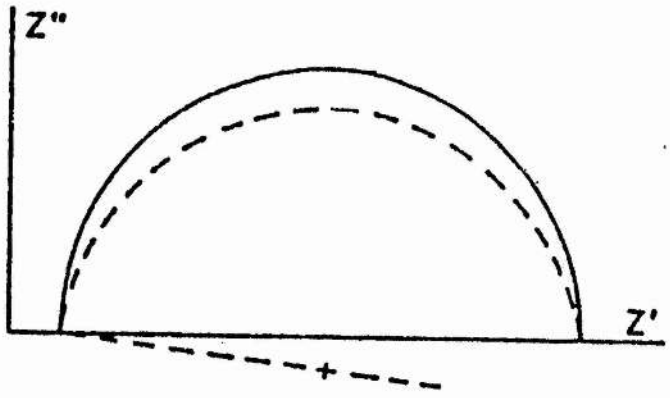

Fig. 5-20. The presence of a constant phase angle element (CPE) on the complex impedance plane results in perfect semicircles being rotated by an angle $\psi = n\pi/2$. From reference [81].

Tafel Plot Analysis

Page 47 of chapter 3 showed that the Butler-Volmer equation could be transformed into simpler equations (the Tafel equations) which enable exchange current densities (j_o) and transfer coefficients (α) to be determined from experiment. The following equations show how the Tafel equations can be expressed in terms of charge transfer resistance (R_{ct}) instead of current.

The simplest case is when the overpotential is small (Eq. 5-2).

$$j = j_o nF\eta/RT. \qquad (5\text{-}2)$$

R_{ct} is defined by rearranging Eq. 5-2 by analogy with Ohm's law.

$$R_{ct} = RT/nFj_o \qquad (5\text{-}3)$$

When, as in this case, the overpotential is large and cathodic, Eq. 5-4 applies.

$$j = -j_o \exp(-\alpha nF\eta/RT) \qquad (5\text{-}4)$$

Sluyters [82] has shown that this expression can be rearranged to give the following relationship between R_{ct} and high cathodic overpotentials.

$$R_{ct} = (RT/n^2F^2k^o)(1/\alpha c^\sigma.\exp(-\alpha nF\eta/RT)) \qquad (5\text{-}5)$$

c^σ is the concentration of Na^+ at the electrode surface. This reduces to,

$$1/R_{ct} = 1/R_{ct}^o.\exp(-\alpha nF\eta/RT). \qquad (5\text{-}6)$$

Here, $1/R_{ct}^o$ represents the reciprocal of the charge transfer resistance which corresponds to the exchange current density j_o.

Values of R_{ct} were obtained from the low frequency semicircles in Fig. 5-19. It was assumed that these semicircles represented impedances of charge transfer since the DC potentials used were lower than those associated with the linear region of the cyclic voltammogram in Fig. 5-15. A plot of $\log(1/R_{ct})$ vs. η (Fig. 5-21) gave a straight line with gradient equal to $-\alpha nF/2.3RT$ that intersected the $\log(1/R_{ct})$ axis at $\log(1/R_{ct}^o)$ and by assuming that n was equal to 1, the transfer coefficient was found to equal 0.6.

Derivation of the Butler-Volmer equation in chapter 3 showed that both concentration of oxidant (c_{ox}) within the electrolyte *and* interfacial potential difference expressed as the overpotential ($\eta = E\text{-}E^{o'}$) were contributory factors to the variation of current with overpotential at the electrode/electrolyte interface (see Eq. 3-17). It therefore appears at first sight that a simple Tafel relationship between current and overpotential should

not arise when a solid electrolyte/electrode interface is being studied because it is impossible to vary the concentration of oxidant within the solid electrolyte (and hence the electrode potential) because the condition of charge neutrality would be violated [9]. Indeed, when this statement is more closely considered it becomes apparent that the Nernst equation is not applicable to the solid electrolyte/electrode interface.

However, the change in ion concentration associated with a change in electrode potential (E) is so small that significant potentials can be applied without seriously violating electroneutrality which, in any case, is only an approximation [83]. Therefore the linear variation of log j with η (Fig. 5-21) that gives rise to values of α and j_o is solely dependent on the change of electrode potential. It is for this reason that the simple Tafel equations do indeed hold for solid electrolyte/electrode interfaces.

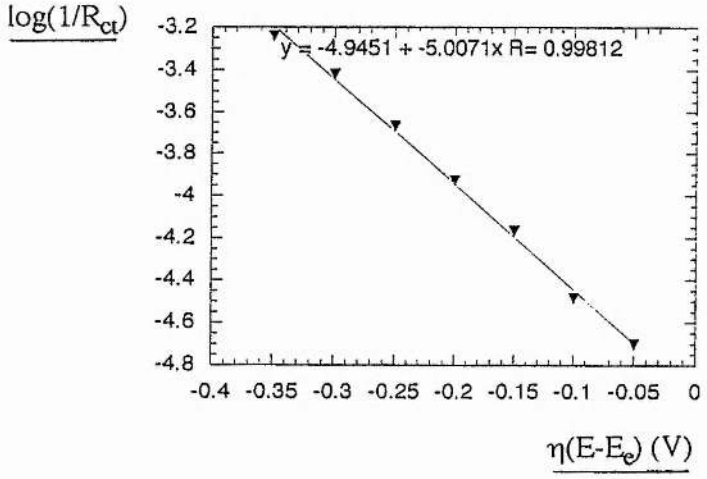

Fig. 5-21. Values of $\log(1/R_{ct})$ taken from the ac impedance data and plotted against their corresponding overpotentials.

Activation Energy for Na^+ Reduction

Since the determination of the activation energies of electrode reactions is important for the theory of electrode reactions it was decided to use the variation of charge

transfer resistance with temperature to extract a value for the activation energy ($\Delta H_o^{\#}$) of sodium ion reduction. This is defined as,

$$1/R_{ct} = 1/R_{ct}^{o}.\exp(-\Delta H_o^{\#}/RT). \qquad (5\text{-}7)$$

AC impedance measurements were made at E_e (-1.70V vs. $Na_{1-x}CoO_2$ - the equilibrium potential of the half-cell reaction in Eq. 5-8)) between temperatures of 280°C and 325°C.

$$Na \rightleftharpoons Na^+ + e^- \qquad (5\text{-}8)$$

The values of $\log(1/R_{ct})$ and 1000/T which were used to produce the Arrhenius plot in Fig. 5-22 are listed in table 5-1. $\Delta H_o^{\#}$ was found to equal 21 $kJmol^{-1}$. It is interesting to note that this value is similar to various standard activation energies of electrode reactions listed in reference [84].

Table 5-1.

$\log(1/R_{CT})$	$1000/T / K^{-1}$
-5.39	1.81
-5.06	1.72
-4.84	1.69
-4.55	1.67
-4.36	1.63

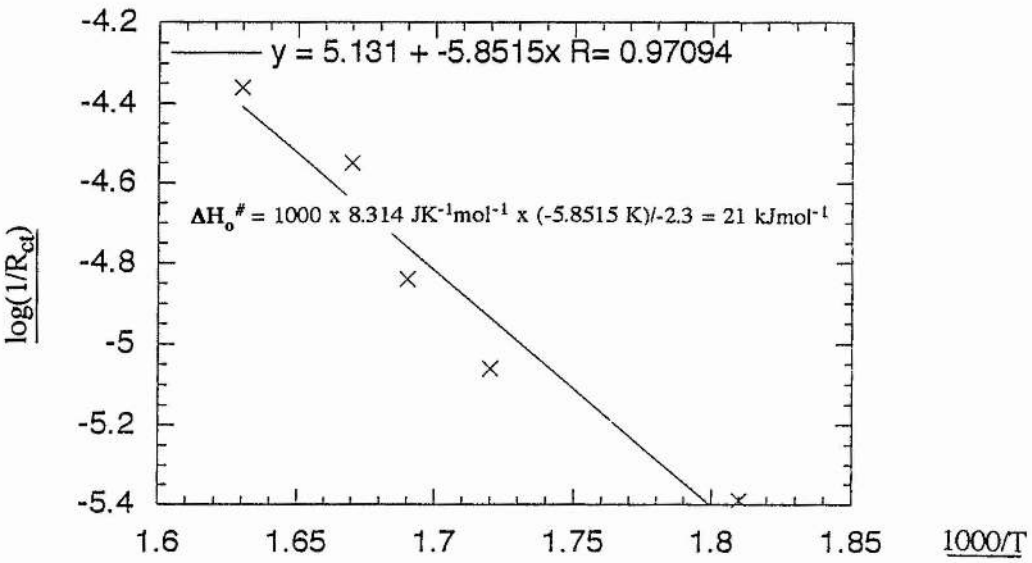

Fig. 5-22. Values of $\log(1/R_{ct})$ taken from ac impedance data and plotted against their corresponding temperatures.

5.4 AC Impedance Analysis of the Na-BASE at 10^{-8} mbar

1) Introduction

Previous complex plane AC impedance analyses of all three sources (Figs. 5-4, 5-8 and 5-19) have shown high frequency semicircles which have been attributed to a parallel combination of resistance and capacitance associated with grain boundaries of the solid electrolyte between reference and working electrodes (iR drop). In order to verify these assumptions, this section sets out to compare ac impedance data obtained from both the three terminal Na cell and two electrode measurements carried out on a pellet of Na-BASE.

2) Experimental

A 13 mm diameter pellet of Na-BASE (0.40 g) was sintered at 500°C for 17 hours in an electric muffle furnace. On removal from the furnace, both sides of the pellet were painted with platinum ink (Englehard - 6082) and initially dried in an oven at 100°C. The pellet was then placed back in the muffle furnace where the temperature was raised from room temperature to 850°C and back to room temperature over a period of three hours in order to attach the platinum to the electrolyte surface.

Two and three electrode ac impedance measurements were made with a 50mV amplitude signal between frequencies of 1MHz and 1mHz without any DC bias.

3) Results and Discussion

The complex impedance plane plot of the pellet in Fig. 5-23, recorded at a temperature of 350°C and a pressure of ~10^{-7} mbar, shows part of a high frequency semicircle with an extended tail at low frequencies. The capacitance associated with the semicircle was found to be 151 $pFcm^{-1}$ which was similar to what was thought to be the capacitance due to grain boundaries separating particles of BASE in the cell (553 pF-Fig. 5-24). Since the electrode geometry was more complicated in the 3 electrode cell it was impossible to accurately measure the cell constant but the

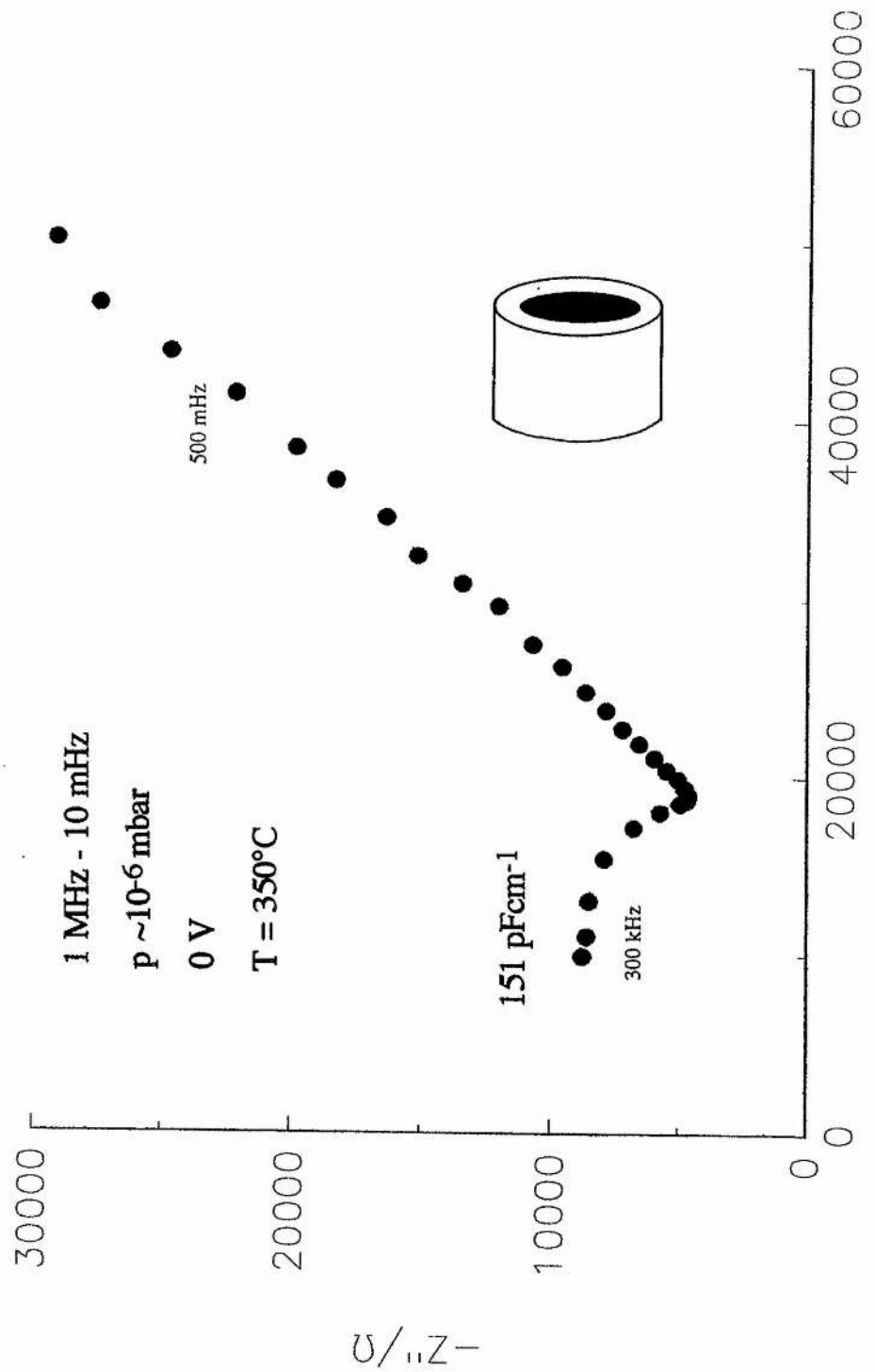

Fig. 5-23. Complex impedance plane plot of a pellet of Na-BASE. Measurements were made at 0 V.

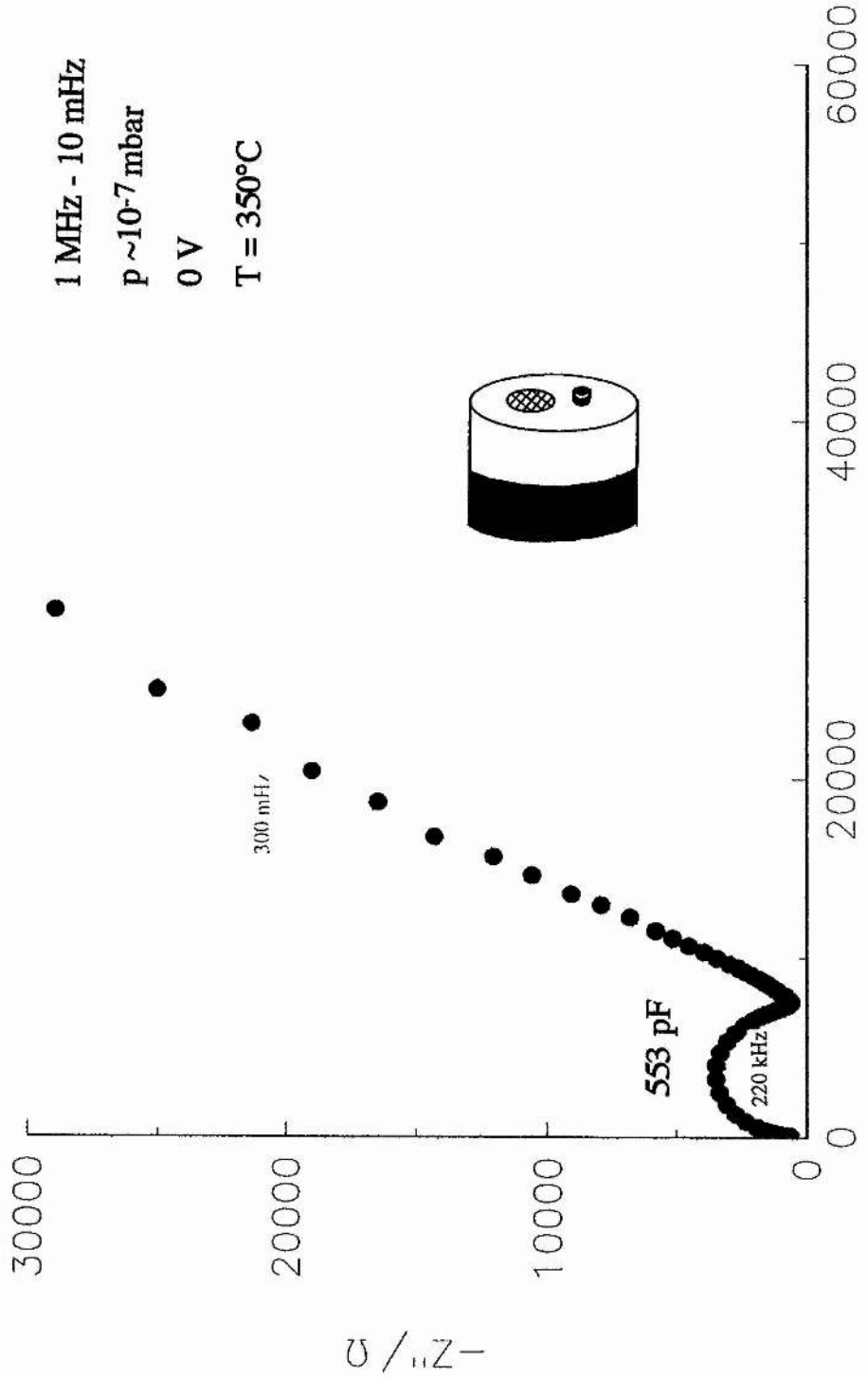

Fig. 5-24. Complex impedance plane plot of the sodium source. Measurements were made at 0 V vs. $Na_{1-x}CoO_2$.

similarity in capacitances suggests that the semicircle in Fig. 5-24 can also be interpreted as an electrolyte response.

The grain boundary resistance of the two electrode cell was taken to be the diameter of the arc and measured approximately 20 kΩ - again similar to the result obtained with the source (8 kΩ).

In conclusion, the previous assumption that the high frequency semicircle is due to electrolyte phenomena is correct.

5.5 Discussion of Sections 5.3 and 5.4

The most important point to extract from the previous two sections is the fact that the nucleation of sodium metal which occurs at 10^{-3} mbar is prevented when the cell is operated in UHV. There are several reasons for this difference in behaviour between 10^{-3} and 10^{-8} mbar. One possible explanation can be given by invoking the following thermodynamic argument. If the liquid metal on the surface is in equilibrium with the gas phase (i.e. at the equilibrium vapour pressure p*) then there would be no evaporation since $\Delta G = 0$. For any other pressure p, ΔG is given by,

$$\Delta G_{evap} = -RT\ln(p^*/p). \qquad (5\text{-}9)$$

In this expression: ΔG_{evap} is the free energy change associated with evaporation of sodium metal; p is the pressure inside the chamber and p^* is the equilibrium vapour pressure of sodium metal.

At 10^{-3} mbar ΔG_{evap} is positive since the electroanalytical measurements clearly indicate the occurrence of nucleation. This infers that $p^* << p$. In UHV the absence of nucleation indicates that $p^* >> p$.

The thermodynamic argument can only be approximate since we know that sodium vapour is still evolved at 10^{-3} mbar. However it is clear that the rate of evaporation is much lower at 10^{-3} mbar than 10^{-8} mbar following the trend in ΔG.

Another explanation could be due to the nucleation and growth of sodium oxide (Na_2O) and/or sodium carbonate (Na_2CO_3) on the surface at 10^{-3} mbar but not at 10^{-8} mbar.

As noted in section 5.3 (Fig. 5-10) cyclic voltammetry with the source at 10^{-3} mbar indicates underpotential deposition of sodium since on the first cycle a reduction current is observed at potentials positive of the equilibrium value. This behaviour was also noted when the same experiment was carried out in UHV (Fig. 5-15).

An AC impedance analysis has shown that two semicircles are present on the complex impedance plane (Fig. 5-19) when the source is operating at relatively low cathodic overpotentials in UHV. The high frequency semicircle has been assigned to the iR drop between reference and working electrodes. This has been verified experimentally in section 5.4 by comparing two electrode measurements (Figs. 5-23 and 5-24) on a pellet of the Na-BASE with those results obtained with the cell.

The low frequency semicircle in Fig. 5-19 becomes smaller as the potential of the working electrode is increased to higher negative values. It has been assumed that this feature represents electron transfer and indeed an activation energy of 21 $kJmol^{-1}$ is similar in magnitude to previously listed values of activation energies for electron transfer [84]. Assuming that this process *is* the transfer of one electron to a sodium ion to create a neutral sodium atom, the reason for the rate of electron transfer becoming faster with increasing cathodic potentials can be explained as follows.

Eq. 5-10 represents the first stage of sodium production i.e. atomic adsorption onto the stainless steel surface after reduction of the sodium ion,

$$Na^+ + e^- \rightleftharpoons Na_{(ads)} \qquad (5\text{-}10)$$

The activation barrier related to the overall free energy change $\Delta G°$ for this process is represented by Fig. 5-25.

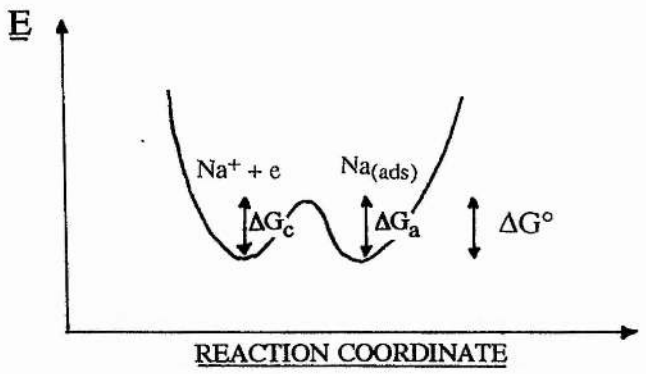

Fig. 5-25. Energy curve for the reaction $Na^+ + e \rightleftharpoons Na$ when $E = E^{o'}$.

The free energy of activation for the reduction of Na^+, ΔG_c, responds to changes of electrode potential because the Na^+ ion is sensitive to the potential difference across the interface. When the potential of the electrode is perturbed from the standard potential, the free energy curves for O and R move apart by an amount given by Eq. 5-11,

$$\Delta G = nF(E-E^{o'}) = \Delta G_c - \Delta G_a. \qquad (5\text{-}11)$$

This is illustrated by Fig. 5-26 where E is made more negative and therefore k_c is greater than k_a.

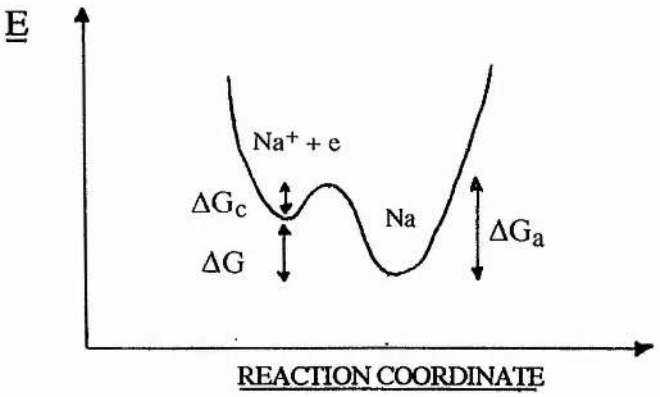

Fig. 5-26. Energy curve for $Na^+ + e \rightleftharpoons Na$ when $E<E^{o'}$ (i.e. reduction of Na^+ occurs).

At the point on the cyclic voltammogram in Fig. 5-15 where the linear region is reached, ΔG_c must be very small since Na^+ reduction is a very facile process at this overpotential. Consequently the energy profile diagram would be expected to resemble Fig. 5-27.

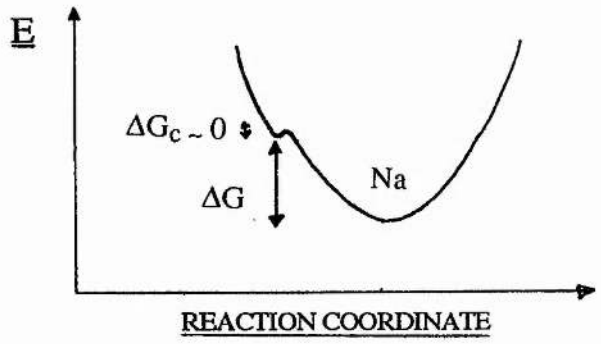

Fig. 5-27. Energy curve for $Na^+ + e \rightleftharpoons Na$ when $E \ll E^{o'}$ and the equilibrium leans very far to the right.

The relationship between rate constants and activation energies can be derived from absolute rate theory. For a heterogeneous reaction the result is Eq. 5-12,

$$k_{(a \text{ or } c)} = \kappa Z.\exp(-\Delta G_{(a \text{ or } c)}/RT). \qquad (5\text{-}12)$$

By considering this it is apparent that as ΔG_c becomes less, k_c becomes greater until it simply equals κZ which is the temperature dependent upper limit to k_c set by the vibrations of the transition state.

So, if the activation energy approximates to zero, the current due to Na^+ reduction becomes independent of overpotential. The fact that UHV prevents the nucleation of sodium means that the only electrical response left for the system to offer is due to the resistance of the Na-BASE between the reference and working electrodes.

Therefore, by assuming that the kinetic process is a simple one electron transfer which produces a sodium atom that is transferred directly into the gas phase, the mechanism can be written as follows:

1st stage $Na^+ + e^- \rightleftharpoons Na_{(ads)}$ underpotential deposition

2nd stage
- $Na^+ + e^- \longrightarrow Na_{(g)}$ rds at low η
- Na-BASE conductivity rds at high η

5.6 In-situ Mass Spectrometry of Na Emission

1) Experimental

Exactly the same equipment which was used during the electroanalytical measurements (Figs. 2-2 and 2-3) was employed during this work; the only difference being the insertion of the quadrupole mass spectrometer head (Fig. 2-5) inside the UHV chamber. The entrance to the ionisation chamber was located approximately 2 cm from the stainless steel gauze surface. Mass spectra were recorded in the range 0-50 amu. The signal intensity could be varied by controlling the multiplier current which was measured on an arbitrary scale from 0 - 2.0.

2) Results and Discussion

The following three experiments were carried out:

a) A test experiment to ensure that the MS could detect reaction products.

b) A spectroelectrochemical experiment with a slow sweep cyclic voltammogram being recorded in conjunction with mass spectroscopic data.

c) A control experiment with the cell removed from the cell holder in order to eliminate peaks due to contaminants within the chamber.

a) The Test Experiment

Fig. 5-28 shows a typical mass spectrum recorded with the cell at elevated temperature but with the power switched off. The chamber pressure was $3x10^{-7}$ mbar and the signal multiplier was set at 2.0. The most intense peaks, found at m/z = 18,

28, 32 and 44, were thought to correspond to H_2O, N_2, O_2 and CO_2 respectively. It was assumed that these molecules were appearing from the interior of the chamber and not the source. Fig. 5-29a shows that turning the multiplier dial down to 1.0 and leaving the chamber to bakeout until the pressure had fallen to $8x10^{-8}$ mbar caused the elimination of these peaks, apart from a small hump due to N_2.

The source was then polarised at -2.5 V with respect to $Na_{1-x}CoO_2$ for 15 minutes. This resulted in the gradual appearance of two peaks (Fig. 5-29b); one at m/z = 23 due to sodium and the other at m/z = 39 which was initially thought to be due to potassium. Why potassium appeared was thought to be due to K^+ ions trapped within the conduction planes of the Na-BASE. Attempts at surmounting this problem by preparing fresh Na-BASE and ensuring that the cells were kept in an oxygen atmosphere after their preparation still resulted in this peak at m/z = 39.

Carrying out this experiment with the sodium peak overriding all others was detrimental to the mass spectrometer since, after 15 minutes had elapsed the pressure rose dramatically and the system ceased to operate. Upon dismantling it was noted that the filament within the ionisation chamber was broken.

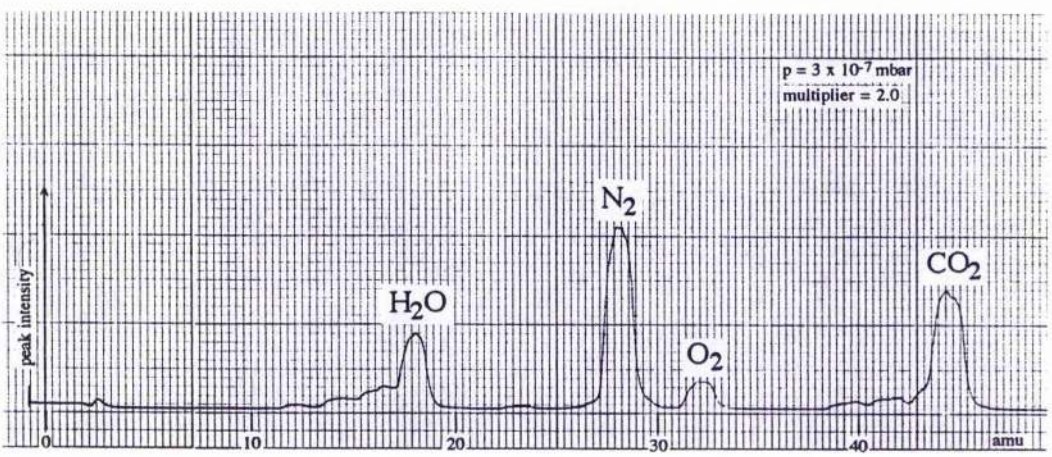

Fig. 5-28. Initial mass spectrum recorded with the cell switched off and with a high multiplier current.

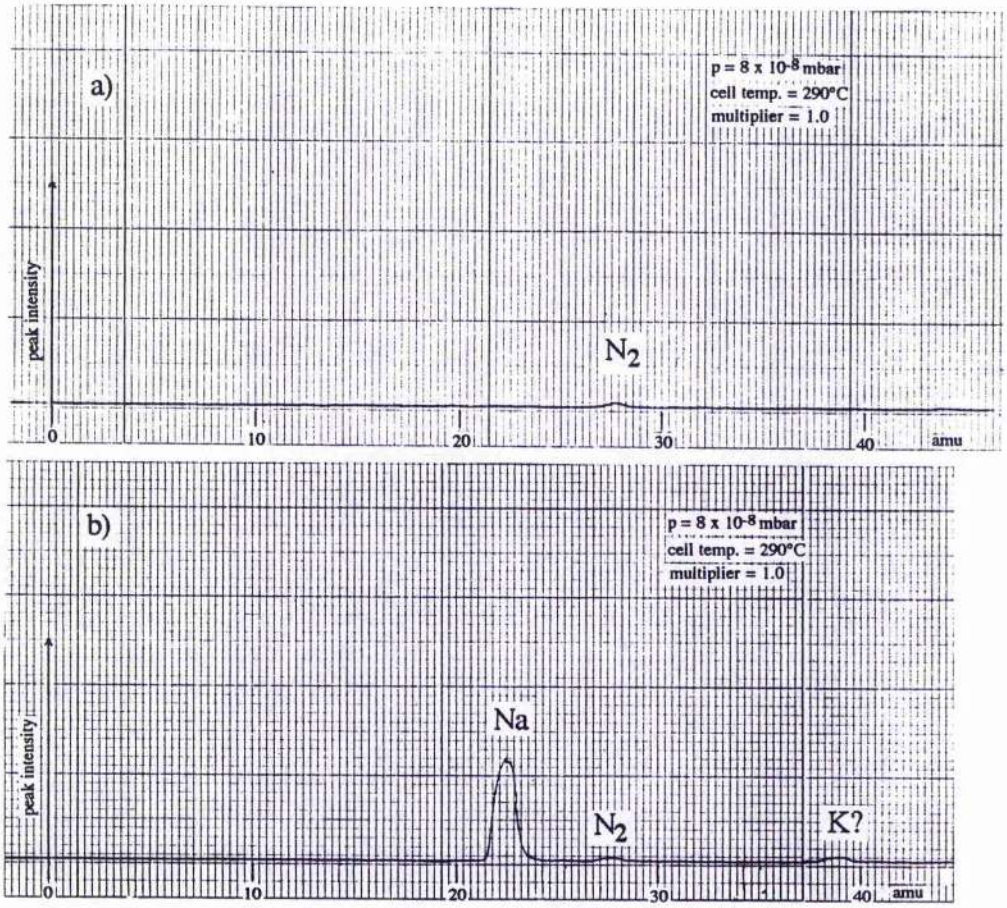

Fig. 5-29. Mass spectra recorded with reduced multiplier currents. a) Cell off. b) After polarising the cell at -2.5 V vs. $Na_{1-x}CoO_2$ for 15 mins.

b) The Spectroelectrochemical Experiment

Fig. 5-30 shows the results of a cyclic voltammetry experiment carried out at a sweep rate of 1.66 mV/s with the mass spectrometer on.

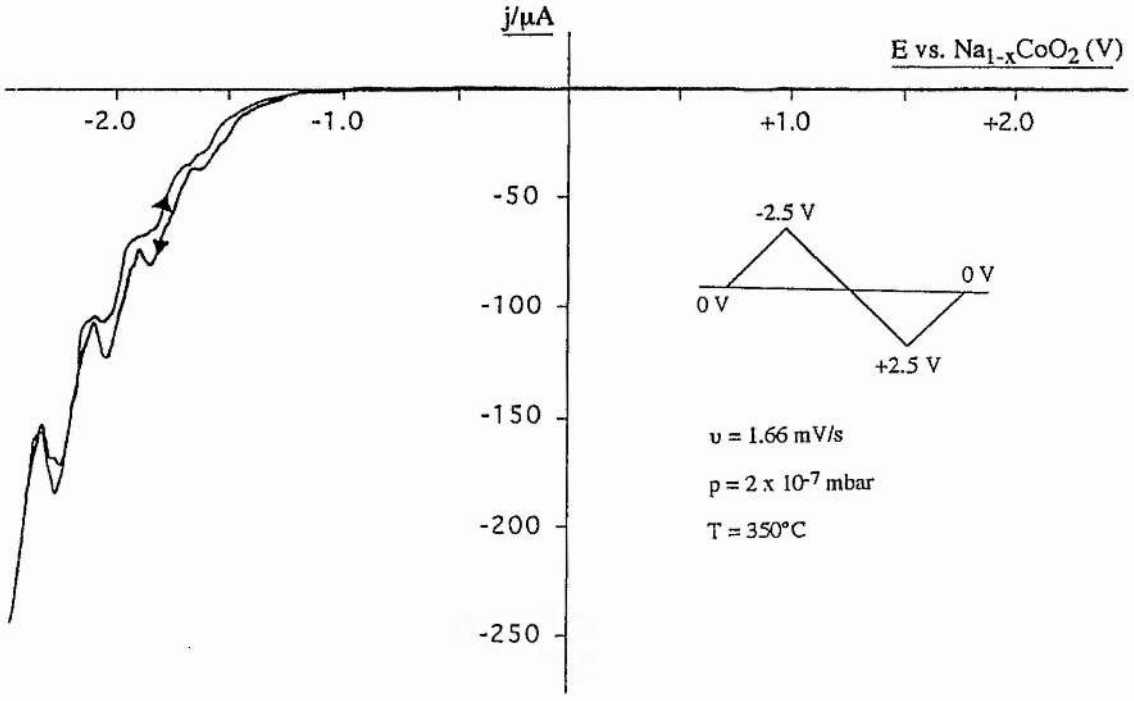

Fig. 5-30. Slow sweep cyclic voltammogram recorded whilst the mass spectrometer was sampling the source's exhaust.

Nineteen mass spectra were recorded throughout this sweep with the multiplier set at 2.0 (Fig. 5-31 a-s). Fig. 5-31a, recorded at the very start of the initial cathodic sweep, showed small responses at m/z = 23 and 39 which were probably left over from the test experiment. The other significant peaks were due to H_2O, N_2, O_2 and CO_2 from the chamber since they remained practically invariant throughout the sweep. Once the potential had been swept to -1.87 V (Fig. 5-31d) there was a notable peak at m/z = 23 corresponding to sodium but no change in the magnitude of the peak at m/z = 39. Indeed it was only once the potential had been swept to values in excess of -2.0 V (Fig. 5-31f) that the m/z = 39 peak became significant. Upon sweep reversal at -2.5 V the sodium and m/z =39 peaks both decayed (Figs. 5-31 j-o). Continuing the sweep into anodic potentials resulted in mass spectra (Figs. 5-31 p-s)

which were exactly the same as that obtained at the start of the sweep with no products of a cell reaction being observed.

c) The Control Experiment

After the previous two experiments the cell was removed from its holder, the system was restored to its original condition, and a mass spectrum recorded in order to ensure that the peaks due to H_2O, N_2, O_2 and CO_2 on Fig. 5-28 and Figs. 5-31 a-s were indeed due to contamination from the interior of the chamber. Fig. 5-32 shows that all peaks are still present alongside small contributions from the m/z = 23 and m/z = 39 peaks which were probably left over from the previous spectroelectrochemical experiment.

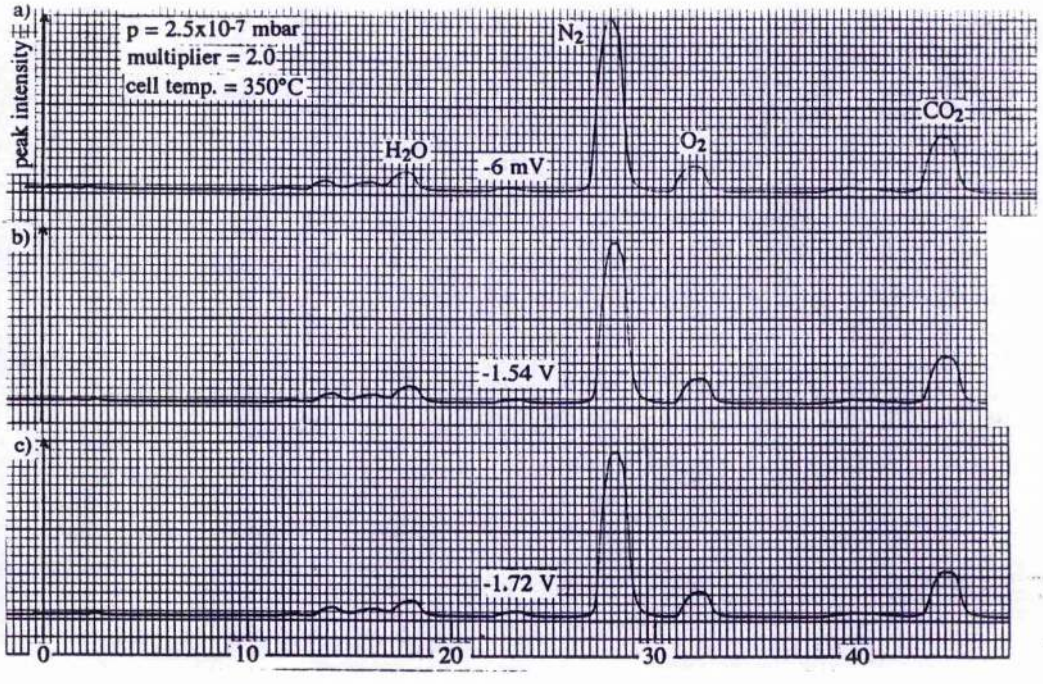

Fig. 5-31 a-c. Mass spectra recorded at potentials on the forward cathodic sweep of Fig. 5-29.

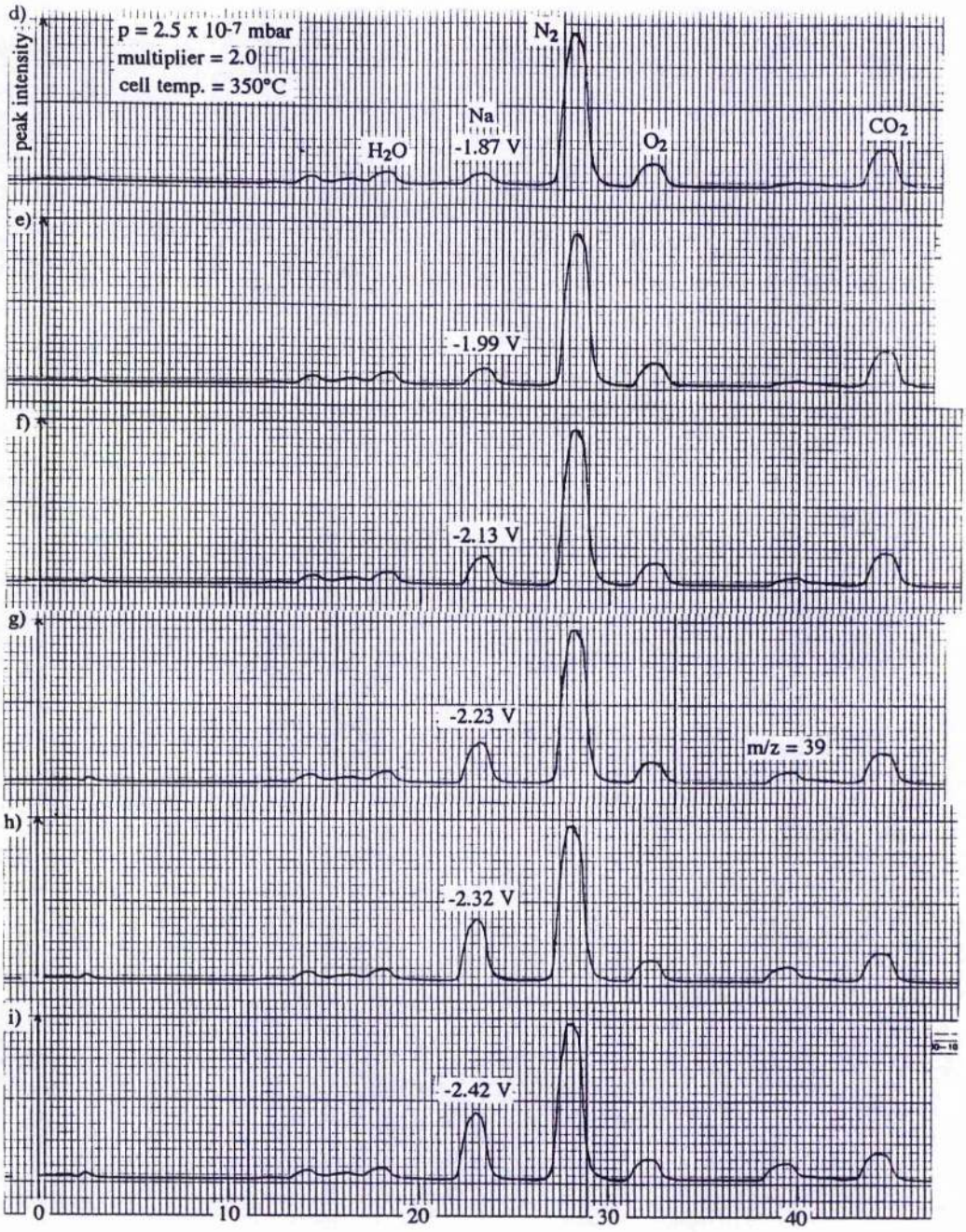

Fig. 5-31 d-i. Mass spectra recorded at potentials on the forward cathodic sweep of Fig. 5-29. The peak at m/z = 23 due to sodium steadily increases as does the ambiguous peak at m/z = 39.

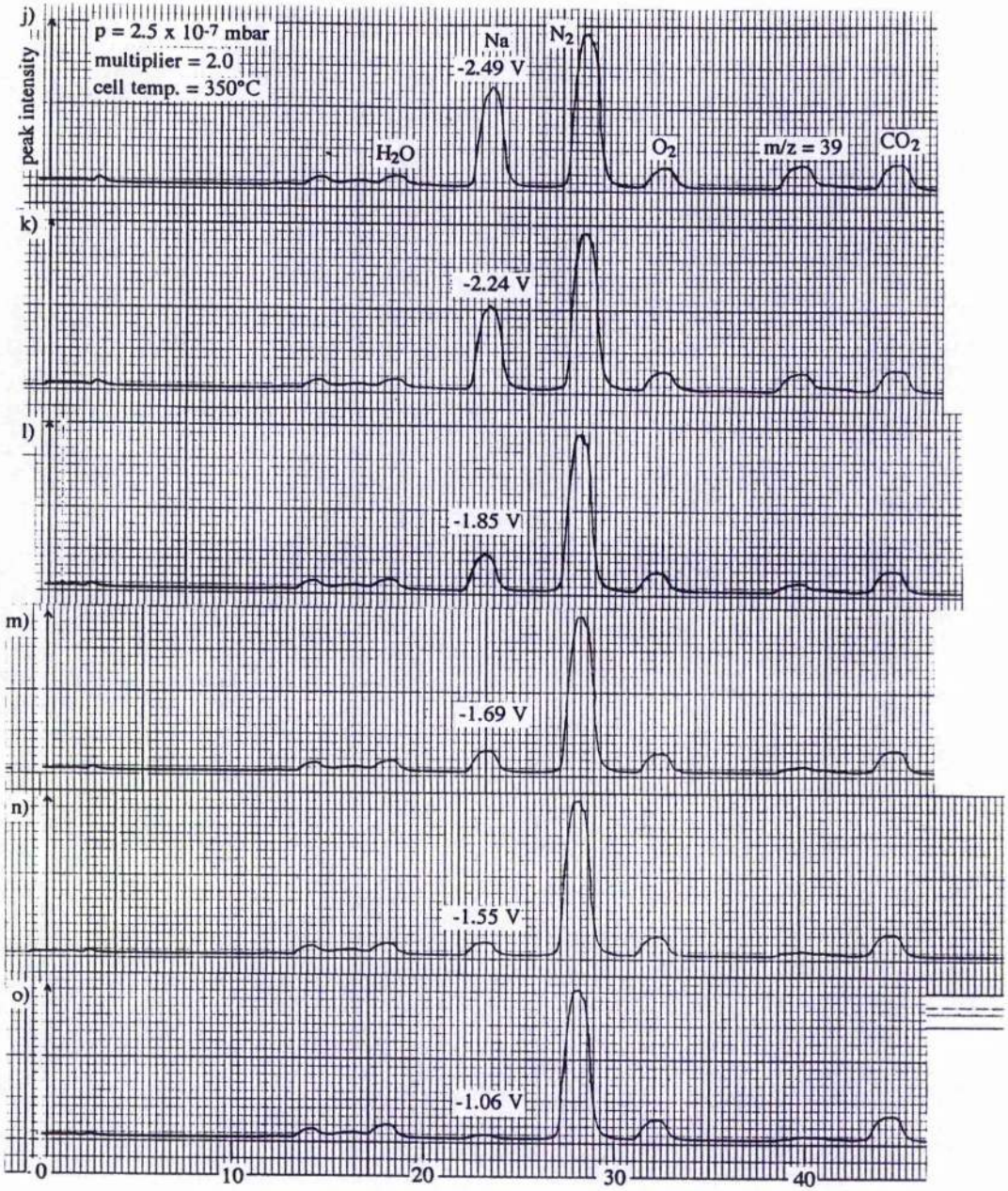

Fig. 5-31 j-o. Mass spectra recorded at potentials on the reverse cathodic sweep of Fig. 5-29. The peak at m/z = 23 due to sodium steadily decreases as does the ambiguous peak at m/z = 39.

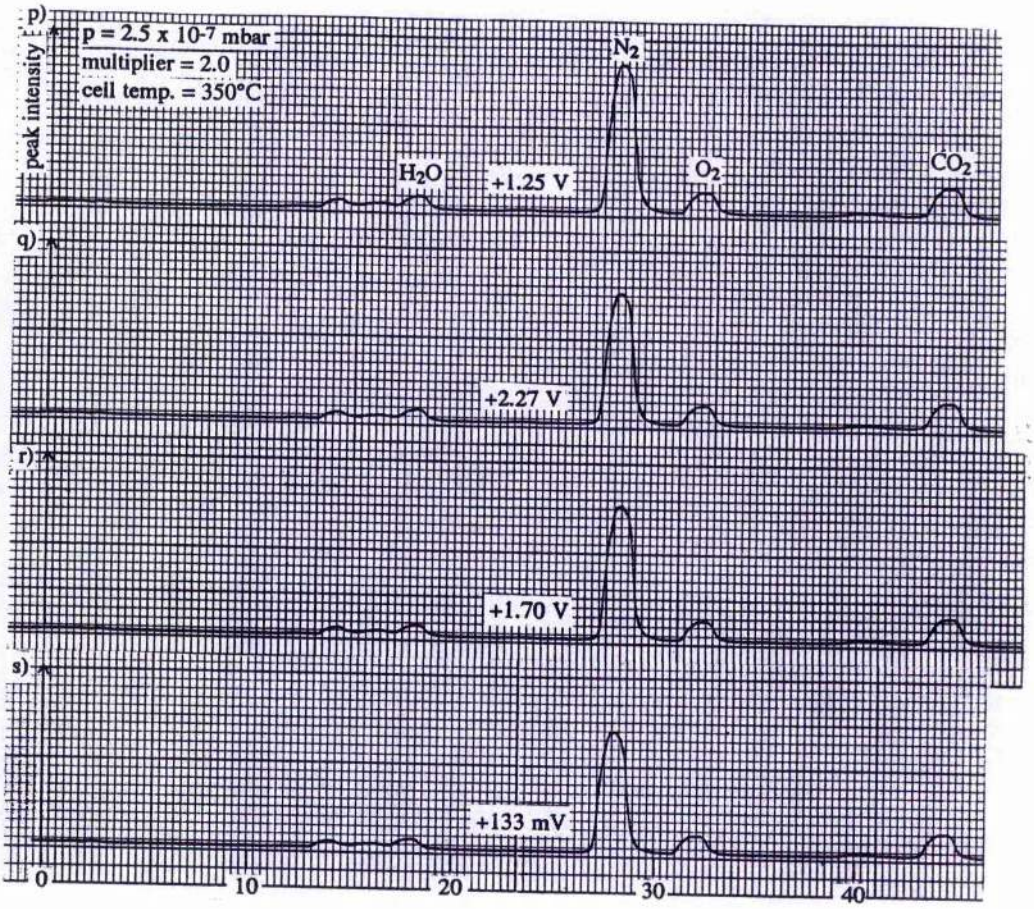

Fig. 5-31 p-s. Mass spectra recorded at anodic potentials on the cyclic voltammogram in Fig. 5-29. The peaks at m/z = 23 and 39 are no longer present.

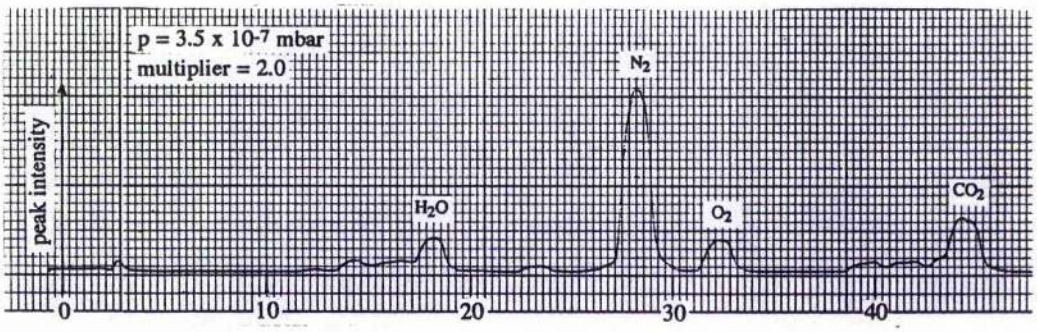

Fig. 5-32. Mass spectrum recorded after the spectroelectrochemical experiment with the cell removed from its holder, but with the UHV system in the same condition as was used to record the mass spectra in Figs. 5-28 and 5-31.

3) Conclusions

The main question which arises from this data concerns the origin of the peak at m/z = 39. It seems unlikely to be due to potassium since care was taken to ensure that the materials used to prepare the cells were as pure as possible. In Fig. 5-31j the ratio of sodium : m/z = 39 is 4:1 and the corresponding current of -240 μA (Fig. 5-30) corresponds to 1.5 x 10^{15} atoms of sodium being released from the source per second. This means that if m/z = 39 is due to potassium, the source would be releasing 3 x 10^{14} atoms of potassium per second - enough to have contaminated the LIMA result shown in Fig. 4-28b.

A m/z ratio of 39 amu could correspond to a NaO^+ fragment which may either be the result of a reaction taking place on the surface of the Na-BASE or a gas phase reaction occurring between the released sodium and oxygen present in the chamber.

Although this experiment has demonstrated the feasibility of monitoring evolution of sodium from the source by in-situ mass spectroscopy, further work will need to be carried out before reliable quantitative information can be obtained.

Cell Applications: Semiconductor Growth

6.1 Potassium Source

1) The Quest for High Quality p-type ZnSe

The development of the III-V compound semiconductor p-n junction throughout the 1960's led to the production of red and green LEDs and semiconductor lasers which have been commercially available since the early 1970's.

III-V semiconductors such as GaP and GaAs have bandgap energies varying from 0.8 ev to 2.4 eV, and are suitable for use as devices in fibre optic communication systems and laser printers as well as red and green LED displays. If these electroluminescent devices were made with materials of larger bandgap, LEDs would be able to emit blue light as would semiconductor lasers. Currently, most compact disc players rely on red semiconductor lasers to read information from the disc. A blue semiconductor laser would lead to a higher density of optical storage since blue light has a shorter wavelength than red. It is anticipated that the disc would be able to hold up to ten times more information. Also, blue semiconductor lasers would aid the development of faster laser printers since a shorter wavelength of laser light would allow the organic pigments responsible for this typing to cast themselves onto the paper at a faster rate [85].

Recently blue LEDs have been made from p-n junctions of silicon carbide [86] (which has a band gap of 2.9 eV) and these are often found on displays which are integral parts of video recorders and hi-fis. SiC is unsuitable for manufacturing blue lasers, however, because it can convert only 0.01 per cent of input power into light or in other words it has a very low quantum efficiency. This is because it has an indirect bandgap and so electron-hole recombinations are slow and compete poorly with nonradiative processes.

Unlike SiC, the II-VI compound semiconductor ZnSe has a direct band gap (E_g = 2.58 eV) and has long been expected to fulfil the requirements necessary for the realization of blue semiconductor lasers [87].

The two main epitaxial growth technologies which are currently being used for synthesising ZnSe semiconductor materials are MOVPE and MBE; both of which have been discussed in the introduction. The remainder of this chapter will focus solely on the role of MBE in p-type ZnSe synthesis, however, since it is the technique with which this part of the research is concerned.

Up until 1991 the main barrier prohibiting the successful production of blue semiconductor lasers based on ZnSe was as fundamental as rendering ZnSe p-type. In the past it has been believed that the establishment of ZnSe as a p-type semiconductor is impossible due to a process called self compensation. In order to understand this phenomenon consider the doping of ZnSe with potassium. For a K atom to replace a Zn atom and hence produce p-type material, the semiconductor temperature has to be raised, and this creates selenium vacancies by evaporation of Se atoms. Each Se vacancy acts as a double donor by donating two free electrons. Let $\Delta E(Se)$ be the energy required to create a Se vacancy, and let $\Delta E(K)$ be the energy released when an acceptor level combines with a donor electron created by the Se vacancy. Since the binding energy of donors and acceptors is small, $\Delta E(K)$ approximately equals the band gap energy E_g. Now suppose that a Se vacancy is created in ZnSe doped with K. If two acceptor levels (from two K atoms) can combine with the Se vacancy, an energy of $2E_g$ is regained in the process. If $2E_g > \Delta E(Se)$, the energy of the system is lowered by the creation of Se vacancies, and the trapping of the acceptor levels by these vacancies will frustrate all efforts to dope ZnSe with K atoms.

The advent of MBE (and MOVPE) meant that this problem could be avoided since it is a low temperature growth technique and therefore less likely to cause the evaporation of elements like Se during crystal growth.

More recently research into II-VIs has been concerned with gaining high quality p-type ZnSe. The term "high quality" refers to optimum values of the material's optical and electrical properties. Three widely used semiconductor characterisation techniques for ZnSe are: photoluminescence spectroscopy, capacitance-voltage

profiling, and secondary ion mass spectrometry (SIMS). This powerful combination has allowed groups from around the world to decide which growth conditions are best for achieving commercially useful p-type ZnSe.

The most successful attempts so far have been made by Haase and co-workers in the USA; their main breakthrough occurring with the use of an active nitrogen beam produced by plasma discharge which creates atomic nitrogen that replaces part of the Se sublattice. Reference [88] provides an account of this work. In this paper, capacitance-voltage profiling showed that when the doping experiment was carried out at a substrate temperature of 230°C, the net acceptor level concentration (N_A-N_D) was 1.0 x 10^{18} cm^{-3}. This was less than the nitrogen density (5.2 x 10^{18} cm^{-3}) detected by SIMS; a result which was thought to be a consequence of impurity donor levels compensating the acceptor levels (donor-acceptor pair recombination - DAP). Further evidence for DAP in this system was gained via photoluminescence spectroscopy. Shortly after this discovery it was found by Cavenett's group at Heriot-Watt University that after storing a 2μm thick wafer of ZnSe:N for a period of 4 months the N_A-N_D level markedly fell [89]. This was thought to be due to selenium vacancies being formed on the surface of the layer which could diffuse through the crystal and create compensating donors.

Prior to this work, our group had carried out an experiment which involved using the potassium cell as a source of dopant. This was an alternative method of producing p-type ZnSe since it involved replacing part of the *zinc* sublattice with an alkali metal. The main reason for trying potassium was that high acceptor level concentrations had previously been gained by doping with lithium [43].

One major problem with lithium, however, is its ability to diffuse through the semiconductor lattice and, therefore, probably through any p-n junctions consisting of ZnSe:Li. The diffusion of Li from p-type to n-type regions of a semiconductor device would cause compensation of donors and subsequent deterioration of device performance.

It was anticipated that this problem could be surmounted by doping with an alkali metal of greater atomic radius - hence potassium. Details of results obtained with the potassium source are presented later in this chapter. Due to lack of access to MBE facilities, only a limited number of experiments could be carried out; however the results are promising and justify further attempts with potassium and sodium sources since there are obviously still problems associated with the material quality of ZnSe:N.

2) Growth of p-type ZnSe with the K Source by MBE

a. Experimental

The MBE apparatus used for semiconductor growth has been described in 2.6 and a brief outline of the MBE process can be found on page 26.

After introduction to the MBE growth chamber the cell holder containing the source (Fig. 6-1) was baked and then degassed for 24 h at 325°C to remove any absorbed water vapour and carbon dioxide.

ZnSe layers were then grown with conventional Zn and Se K-cells on a GaAs (100) substrate which was held at a temperature of 280°C. Source materials were Se (Osaka Asahi, 6N super grade) and Zn (Johnson-Matthey 6N). During growth the cell was maintained at 325°C and a constant current of 25 μA was passed through the cell which generated a potassium atom flux of $1.6 \times 10^{14}\ s^{-1}$. The pressure within the MBE machine was $\sim 10^{-9}$ Torr.

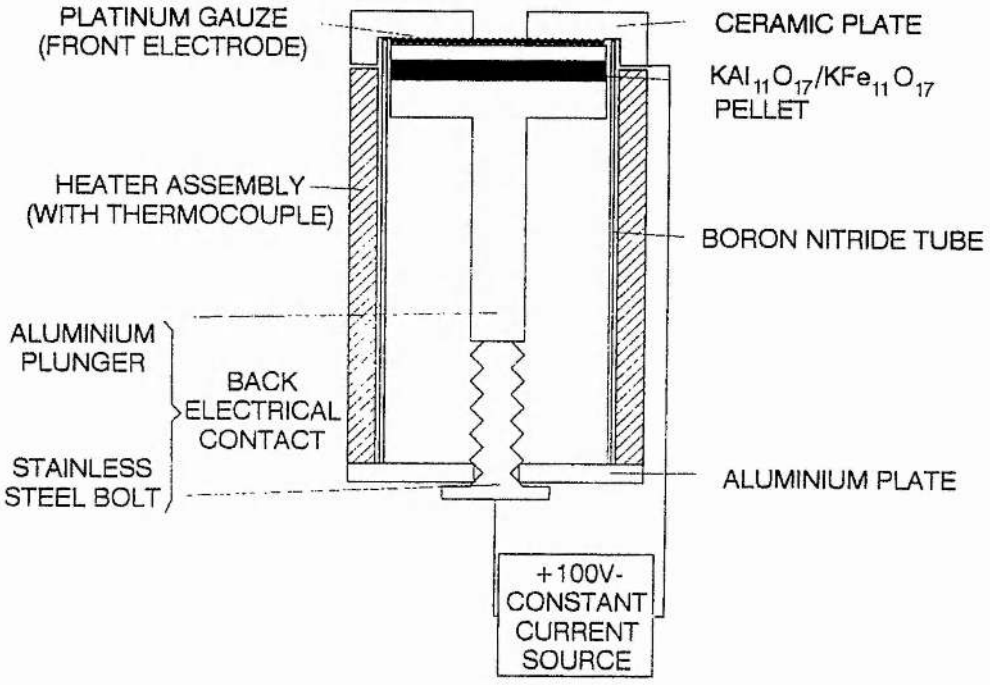

Fig. 6-1. A diagram of the source as used in MBE, showing the component parts and external circuitry.

b. Results and Background Concerning the Semiconductor Characterisation

All experimental equipment used to obtain the results has been mentioned in 2.6.

Photoluminescence Spectroscopy

Photoluminescence is based on the excitation of a semiconductor material by a light source containing photons with energies larger than the bandgap of the material. This results in the creation of excess electron-hole pairs which give rise to the spontaneous emission of luminescence that allows a qualitative assessment to be made of impurities and defects present within the semiconductor.

Reduced to its essentials, the PL spectrometer is represented by Fig. 6-2.

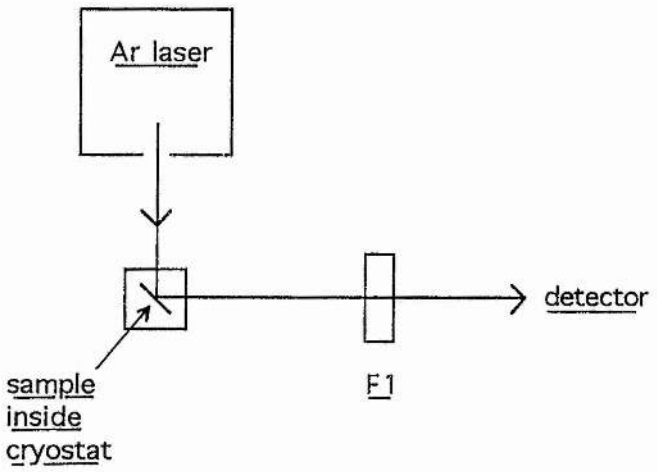

Fig. 6-2. Schematic diagram of a photoluminescence spectrometer.

In this work an Ar laser with a wavelength of 514.5 nm was used as the excitation source.

The resultant luminescence is focused into a monochromator via the filter F1 which excludes any residual exciting laser light.

The sample to be analysed is placed in a cryostat containing liquid helium which ensures that measurements are recorded at approximately 4 K in order to minimise the broadening of sharp spectral features by lattice vibrations.

Fig. 6-3 shows two luminescence decay processes stimulated by above band gap photoexcitation.

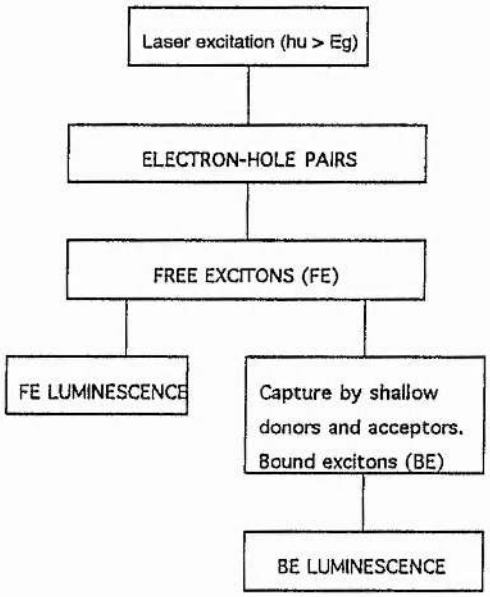

Fig. 6-3. Luminescence decay processes stimulated by above band gap photoexcitation.

In high purity material, excess holes and electrons predominantly form excitons which subsequently decay giving rise to free-exciton luminescence (the left hand path of Fig. 6-3). If the material contains donors and acceptors with concentrations $>10^{15}$ cm^{-3} then virtually all of the free excitons are captured giving rise to impurity-specific bound-exciton luminescence (the right hand path in Fig. 6-3).

Fig. 6-4 shows the 4 K PL spectrum of a 1.5 μm thick sample of the ZnSe doped with potassium. The spectrum shows a clear acceptor bound exciton (A^o,X) peak as well as residual free excitons (FE) and a donor bound exciton (D^o,X) which was believed to be due to Ga diffusion from the substrate. No donor-acceptor

pairs were observed. This was proof that the potassium atoms were effectively incorporating themselves into the zinc sites and thus creating acceptor energy levels.

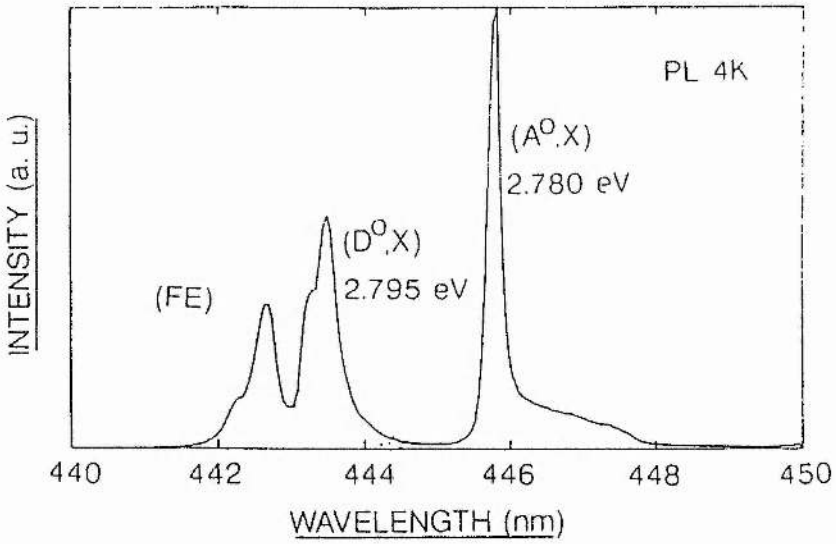

Fig. 6-4. 4K PL spectrum of potassium doped ZnSe.

Capacitance-Voltage Profiling

This technique was used to find out the concentration of acceptor levels as a function of semiconductor depth. It involved making electrical measurements on a Schottky diode which was prepared from the grown material by placing it in contact with an aqueous solution of 1M sodium hydroxide and 1M sodium sulphite [90] which is also capable of etching the semiconductor.

Fig. 6-5 shows the experimental arrangement which is an electrochemical cell. The sample was mounted on a PVC sealing ring that defined the area to be etched. A back electrical contact was attached to the semiconductor which was deemed the working electrode. Besides this, three other electrodes were employed: a platinum electrode was used for C/V measurements; a carbon electrode was used as the counter electrode, and a saturated calomel electrode was used as a reference against which the equilibrium potential and overpotential could be measured.

To measure carrier concentration by C/V methods, conditions must be such that a region depleted of carriers is formed. For p-type ZnSe, where the majority carriers are holes, this condition is satisfied by positive ions in solution, Fig. 6-6. By making the semiconductor more negative than its equilibrium value (reverse biasing the junction) positive ions are attracted to the interface.

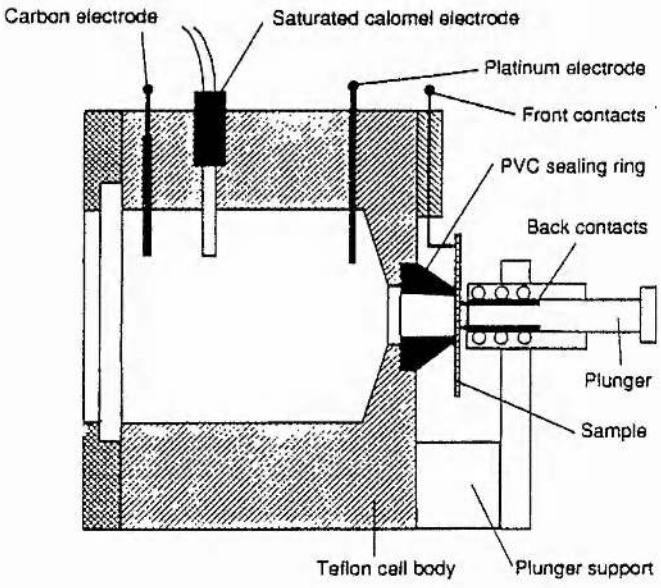

Fig. 6-5. Electrochemical cell for carrying out capacitance-voltage measurements.

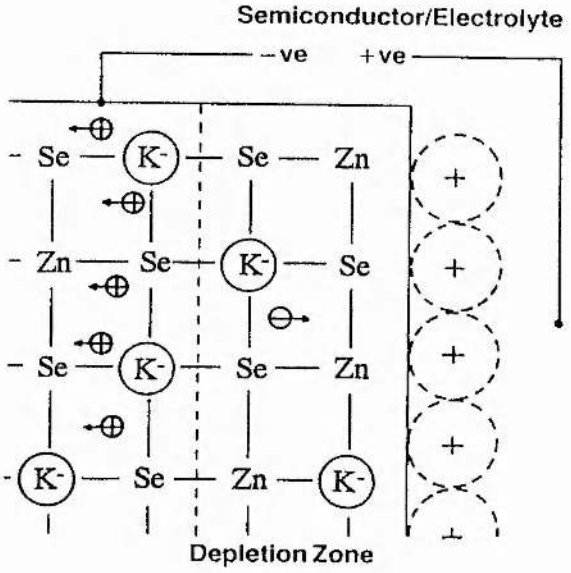

Fig. 6-6. The ZnSe:K/liquid electrolyte junction under reverse bias during a capacitance-voltage profiling experiment.

Eqs. 6-1 and 6-2 which define depletion width (W_d) and capacitance (C) respectively are well known for metal/semiconductor junctions and also apply to this type of interface.

$$W_d = (2\varepsilon_o\varepsilon_r(\Phi\text{-}V)/eN)^{0.5} \qquad (6\text{-}1)$$

$$C = A(eN\varepsilon_o\varepsilon_r/2(\Phi\text{-}V))^{0.5} \qquad (6\text{-}2)$$

From Eq. 6-2 we can write Eq. 6-3.

$$C = \varepsilon_r\varepsilon_o A/W_d \qquad (6\text{-}3)$$

By differentiating C with respect to W_d we arrive at Eq. 6-4.

$$dC/dW_d = -\varepsilon_r\varepsilon_o A/W_d^2 = -C^2/\varepsilon_o\varepsilon_r A \qquad (6\text{-}4)$$

Substituting Eq. 6-4 into Eq. 6-5,

$$C = dQ(W_d)/dV = eN(W)dW_d A/dV \qquad (6\text{-}5)$$

gives,

$$C = -eN(W)\varepsilon_r\varepsilon_o A^2(dC/dV)/C^2. \qquad (6\text{-}6)$$

Which can be rearranged to give Eq 6-7.

$$N(W_d) = -C^3(e\varepsilon_r\varepsilon_o A^2)^{-1}.(dC/dV)^{-1}. \qquad (6\text{-}7)$$

Thus from measurement of capacitance C at applied reverse voltage V and of the rate of change of C with V, the carrier concentration N at the depth W_d (found from the measured capacitance of Eq. 6-3) can be determined.

The use of liquid electrolytes in capacitance-voltage measurements is a relatively new development since conventional C-V experiments involve making metal-semiconductor Schottky diodes. Using a liquid electrolyte (1M NaOH / 1M Na_2SO_3 in this case) is advantageous because when the semiconductor / liquid electrolyte junction is forward biased, holes (h) are attracted to the interface which promote the dissolution of ZnSe and permit depth profiling of the material by either Eq. 6-8 or Eq. 6-9.

$$ZnSe + 4OH^- + 2h \longrightarrow ZnO_2^{2-} + Se + 2H_2O \qquad (6\text{-}8)$$

$$ZnSe + 10OH^- + 6h \longrightarrow ZnO_2^{2-} + SeO_3^{2-} + 5H_2O \qquad (6\text{-}9)$$

Fig. 6-7 shows that the prepared p-type ZnSe had an acceptor level concentration of approximately 10^{15} cm^{-3} at depths between 1.0 and 1.5 μm.

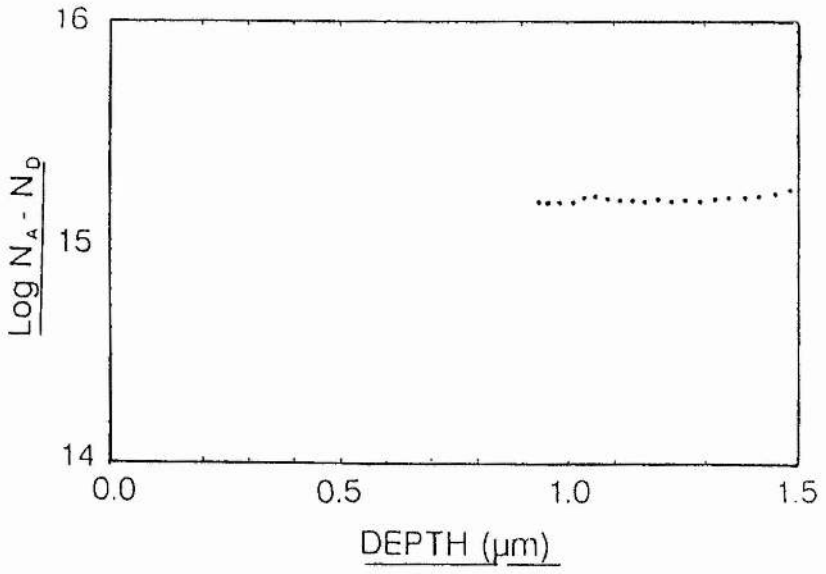

Fig. 6-7. CV profile of ZnSe:K.

Secondary Ion Mass Spectrometry (SIMS)

In SIMS the sample is bombarded in vacuo by an energetic beam of primary ions. As a result, particles are sputtered from the sample surface, some of which are in the form of secondary ions. The positive or negative ions are extracted into a mass spectrometer and separated according to their mass to charge ratio. With primary beam rastering, the sputter erosion causes the sample surface to recede in a very controlled way. By monitoring the intensity of one or more mass peaks as a function of bombardment time, an in depth concentration profile is obtained.

The SIMS profile in Fig. 6-8 was measured using O_2^+ primary ion bombardment at 8 keV with secondary ions being sampled from an 8 μm diameter area. The potassium level is high at the surface (10^{19} at. cm^{-3}) but decays rapidly to 10^{15} at. cm^{-3} within the first 0.1μm. There is a peak at the layer/substrate interface of 10^{17} at. cm^{-3} which was thought to be due to residue left on the substrate prior to growth. Zinc, selenium and arsenic (which is from the GaAs substrate upon which growth took place) profiles are shown as counts, not concentration, and the right hand axis applies for these species.

Figure 6-9 is a separate profiling run with a larger secondary ion acceptance area (60 μm diameter) in an attempt to increase the potassium signal. This showed a marked slope from the surface down to 0.7 μm which was different from the previous analysis. Nevertheless the base level of mid 10^{14} at. cm^{-3} was similar. It was thought that spatial inhomogeneity of potassium on the surface of the wafer may have been responsible for these higher concentrations. In order to verify this a further investigation was carried out with an ion imaging system which provided images over a 150 μm diameter area (Figs. 6-10 a-d).

Images are shown at the following depths: surface, 0.05 μm, 0.07 μm, 0.1 μm. They show an overall "wash" of potassium at the surface with 10-20 μm aggregations of high concentration. These persisted up to 0.1 μm and were therefore responsible for the higher concentrations observed in Fig. 6-9

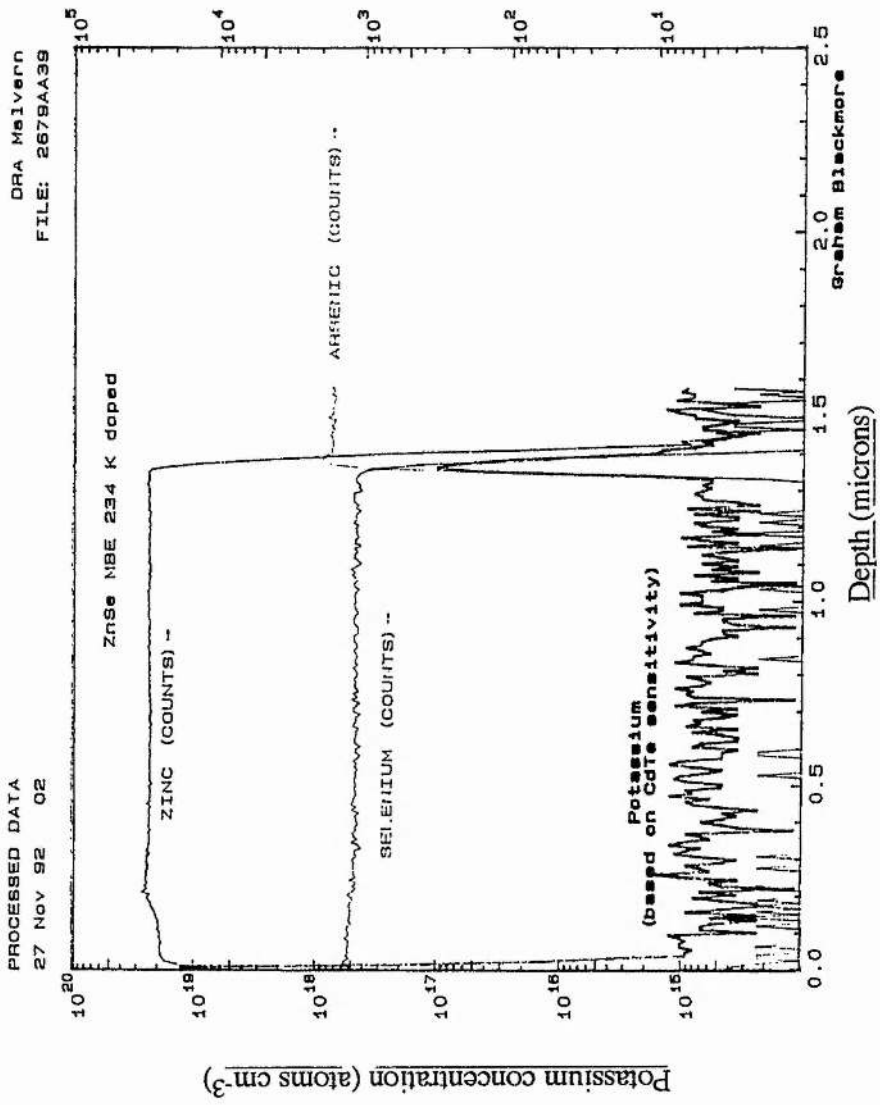

Fig. 6-8. SIMS profile of ZnSe:K with secondary ions sampled from an 8 μm diameter area.

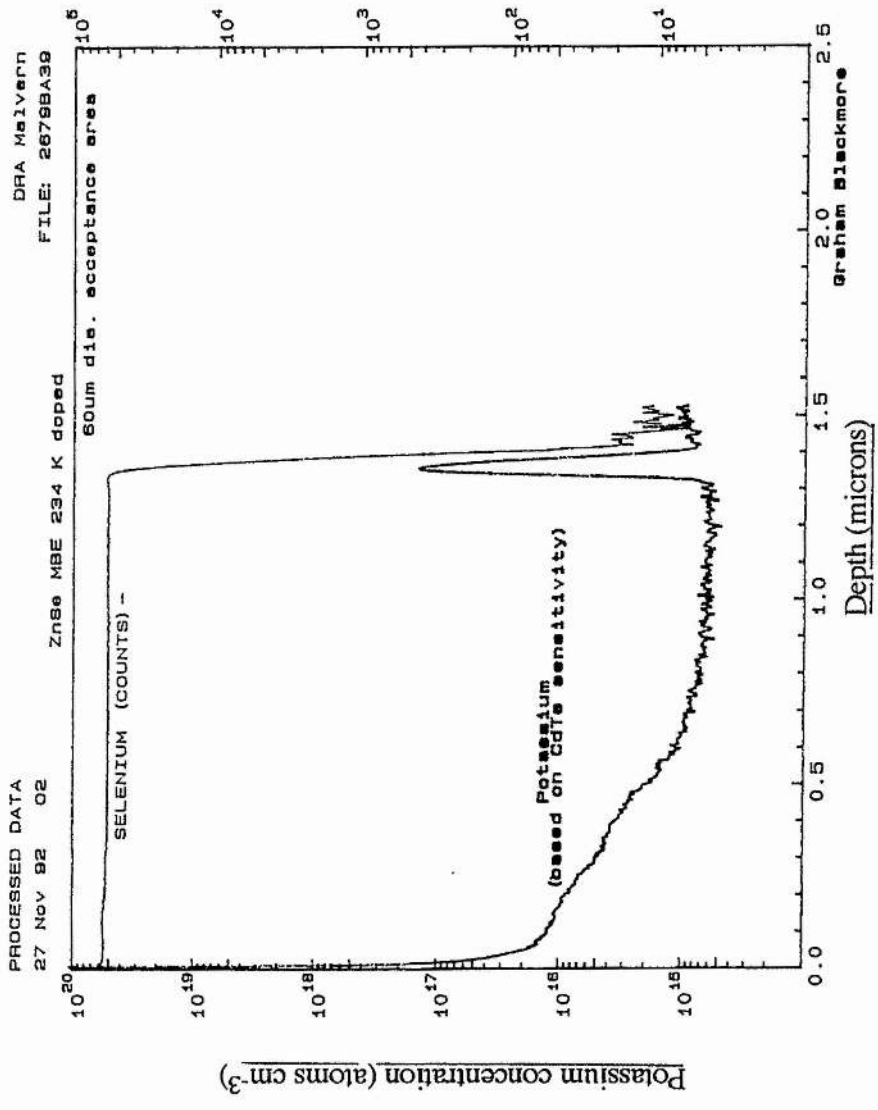

Fig. 6-9. SIMS profile of ZnSe:K with secondary ions sampled from a 60 µm diameter area.

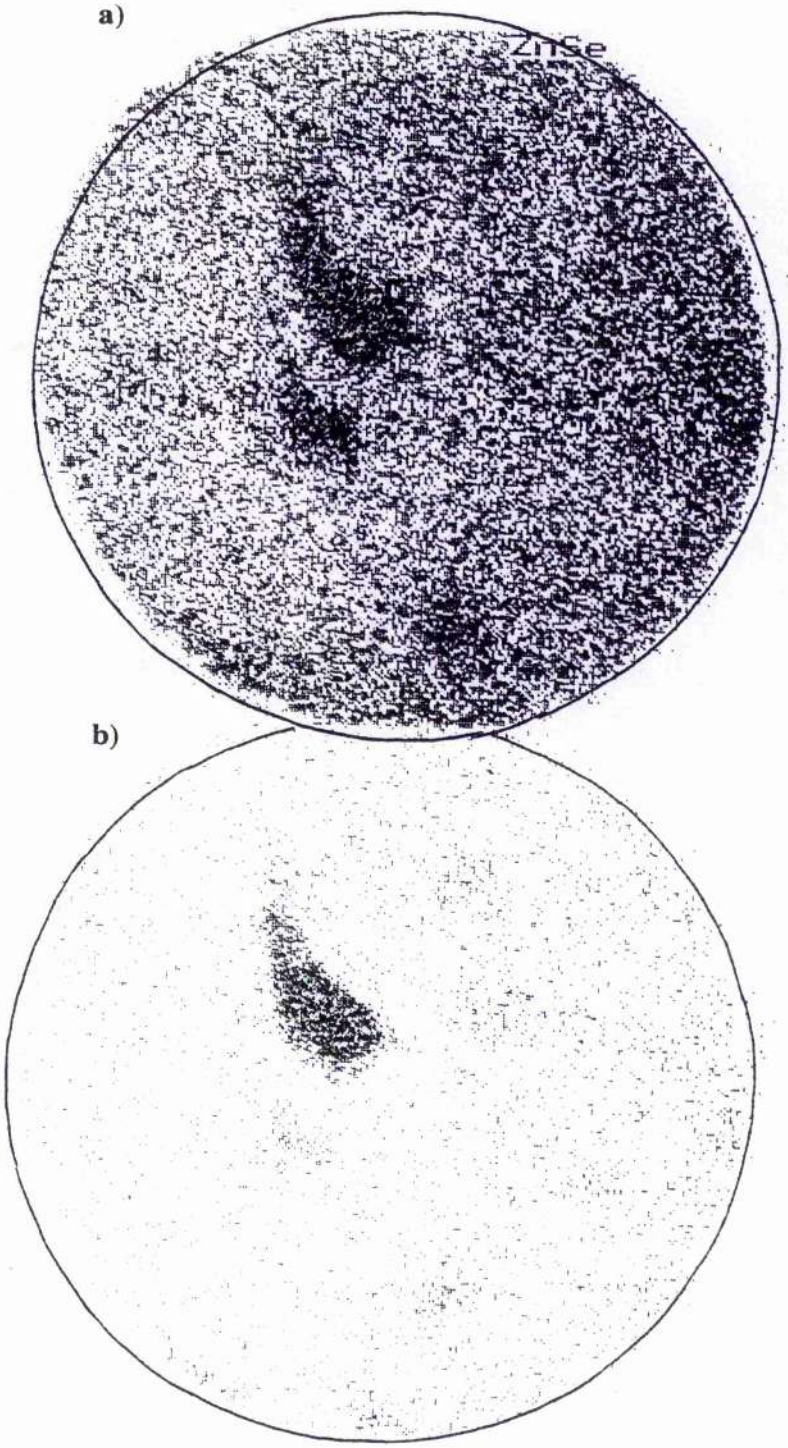

Fig. 6-10. Imaging SIMS results taken from a 150 μm diameter area of ZnSe:K. The black dots represent potassium.

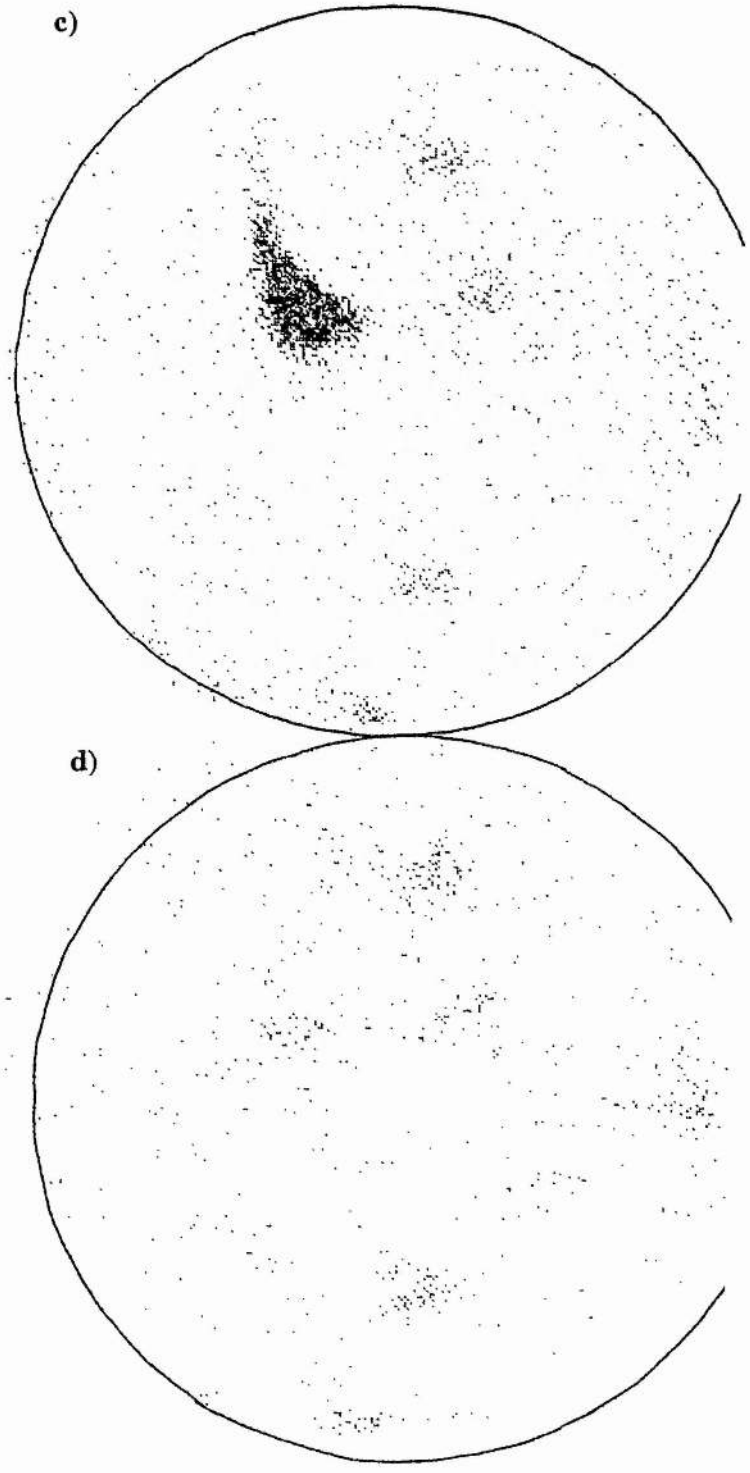

Fig. 6-10. Imaging SIMS results taken from a 150 μm diameter area of ZnSe:K. The black dots represent potassium.

3) Discussion

The PL measurements showed that ZnSe could be doped by the potassium source to produce uncompensated p-type material.

A C/V measurement showed that the ZnSe:K was doped to a level of 2-3 x 10^{15} acceptors/cm^3 which is low compared with, say nitrogen (1.0 x 10^{18} cm^{-3}).

SIMS analysis showed that high levels of potassium were present on the surface but significantly less was detected further in the sample.

There is therefore a considerable barrier to incorporation of potassium under the growth conditions used in this work. This has been observed in other dopant systems, such as ZnSe:Na [43] and GaAs:Sn [91]. Surface enrichment in the case of GaAs:Sn occurs at substrate temperatures of ~600°C. Starting with a surface free of tin, it is not until the surface concentration C_s becomes one thousand times that of the bulk concentration C_b that a steady state is reached where all the incident Sn flux is incorporated as active dopant in the bulk. According to Heckingbottom *et al.* [91] there are two ways of explaining this barrier to Sn incorporation.

The first is a kinetic argument which is best understood by considering Eq. 6-10.

$$dC_s/dt = J_{Sn} - KC_s - DC_s \qquad (6\text{-}10)$$

Where C_s is the surface concentration of Sn, J_{Sn} is the Sn flux, K is the surface rate limited incorporation rate constant and D the desorption rate constant. It has been shown previously [92] that the desorption rate is negligible i.e. $DC_s = 0$, so that the mass balance equation becomes simply

$$dC_s/dt = J_{Sn} - KC_s \qquad (6\text{-}11)$$

During the MBE experiment C_s builds up with time until $KC_s = J_{Sn}$, and there is a steady state situation where $dC_s/dt = 0$.

Secondly, they state that two thermodynamic considerations also explain why surface enrichment occurs. This time a distribution coefficient for Sn between surface and bulk (σ) is assumed to equal unity (Eq. 6-12).

$$\sigma = C_b(\text{equil.})/C_s(\text{equil.}) \qquad (6\text{-}12)$$

Figure 6-11 (taken from their paper) represents two different explanations; both based on the free energy of Sn either in the bulk or on the surface. In Fig. 6-11a the free energy in the bulk is lower than on the surface so easy incorporation would be expected. As illustrated on the diagram, however, a large kinetic barrier prevents this. In Fig. 6-11b the free energy of surface Sn is considered to be *lower* than that in the bulk. Therefore, even though there is only a small kinetic barrier to its incorporation in the bulk, most Sn will accumulate on the surface.

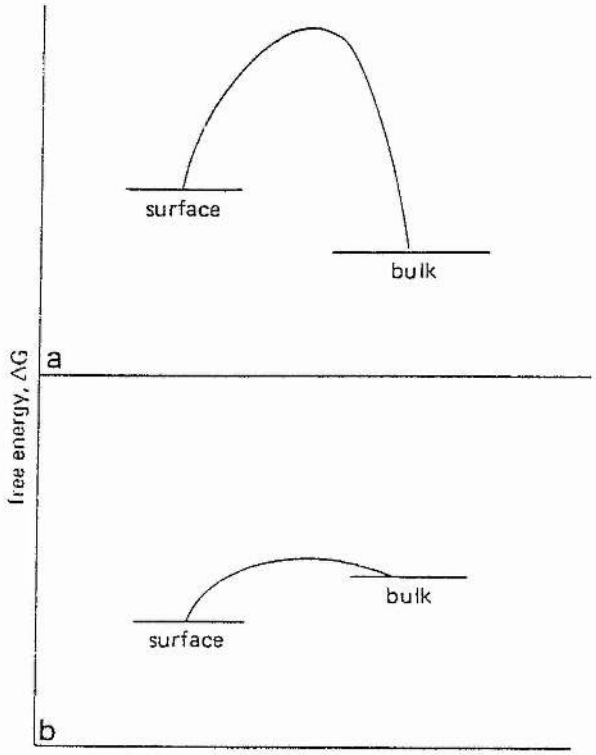

Fig. 6-11. Schematic representation of the thermodynamic explanations for the observed surface enrichment in Sn doping of GaAs. From reference [91].

These two thermodynamic models both provide explanations for why there is considerable difficulty associated with introducing Sn into GaAs, but it should be pointed out that there is a flaw in their terminology. If the distribution coefficient (or equilibrium constant) is assumed to equal unity then ΔG should equal zero and there should be no difference in energy between surface and bulk levels as shown in Fig. 6-11. Equation 6-13 is the Van't Hoff isotherm.

$$\Delta G = \Delta G^{o} + RT\ln(a_b/a_s) \qquad (6\text{-}13)$$

In this expression a_b/a_s is expressed in terms of the activity of Sn in the bulk (a_b) and Sn on the surface (a_s).

When $\Delta G = 0$ the ratio of activities is that of the equilibrium values for the two situations depicted by Fig. 6-11 where surface Sn is prevented from entering the bulk. Therefore, if standard Gibbs free energies (ΔG^{o}) are used instead of simply Gibbs free energies (ΔG), the arguments are correct.

After considering the preceding discussion, assuming that the same reasons for the problem associated with GaAs:Sn also apply to ZnSe:K, and taking into account the fact that potassium is a more volatile element than tin, it appears that perhaps the ZnSe may not have been exposed to the potassium source for a long enough period of time in order to allow the surface concentration to become sufficiently greater than the bulk concentration such that the steady state is reached.

6.2 Lithium Source

1) Diamond Electronics

A recent review of diamond film semiconductors by Geis and Angus in Scientific American [93] states that: "Devices resulting from this material would be able to operate at temperatures up to 700 degrees Celsius." An example of a situation where this property associated with diamond based devices would be useful can be found by consulting reference [94] which provides a fairly detailed account of the electrical properties and device applications of diamond films. The following quote is taken from the introduction: "In unmanned spacecraft the systems required to cool conventional silicon devices to 125°C could be largely eliminated if operating temperatures of 325°C were permissible. These cooling systems can occupy up to 60% of the volume of an unmanned satellite".

Credit goes to W. G. Eversole of Union Carbide who, in the early fifties, succeeded in growing diamond seed crystals from carbon monoxide and hydrocarbon gases at moderate pressure for the first time. Shortly after this event the fact that diamonds possess semiconducting qualities was recognised by Custers. These two important discoveries showed that there was a possibility of fabricating bipolar devices made out of diamond and this should eventually lead to verification of the two aforementioned quotations.

Forty years on, however, many obstacles preventing this must still be overcome. The most important is the difficulty of developing a means of producing films which are actually suitable for diodes and transistors. Today, there are essentially four different methods of diamond film growth. Microwave enhanced CVD (MWECVD) has been mentioned in chapters 1 and 2 since this research involves its use and details of the other three can be found by consulting reference [40]. At present, none of the four methods can be termed "the best" since the applications of diamond are so varied that in many instances one of the techniques is preferable to the others. An important point to note is that all four approaches result in the

production of polycrystalline diamond films consisting of innumerable tiny grains and the atomic disorder at grain boundaries makes the films unsuitable for semiconductors. Current methods of inhibiting this polycrystalline film formation during crystal growth are capable of producing diamond substrates up to an inch in diameter but standard semiconductor fabrication equipment requires circular substrates two inches or more across. Although growing films of this size does not appear to present insuperable difficulties, the experiment has yet to be attempted.

Another problem, the one which this chapter addresses, is associated with obtaining a route to synthesis of diamond with n-type conductivity. Obviously the construction of electronic devices requires both n-type and p-type materials. Naturally occurring diamond stones often contain small amounts of boron which renders them p-type but these diamonds suffer a range of disadvantages for electronics, however, since: their size is usually limited to a few millimetres side length; the inherent quality from stone to stone is highly variable; and the quality inside any one stone is also subject to observable variation [95].

In 1986, Fujimori *et al.* reported the synthesis of p-type semiconducting diamond by use of the MWECVD technique with diborane (B_2H_6) as the dopant [96]. Besides diborane it has also been found that boron trioxide (B_2O_3) is a suitable precursor for introducing boron to the diamond lattice during CVD [97]. In contrast to CVD, another method capable of producing p-type diamond is ion implantation of boron [98].

Attempts at making n-type diamond have been less successful owing to the apparent difficulty in introducing donor states in the bandgap. Diphosphorous pentoxide (P_2O_5) has been used in hot filament CVD equipment by Okano *et al.* [97] and they report that Hall measurements indicate signs of n-type conduction with a carrier concentration of $1.5 \times 10^{15}\,cm^{-3}$, although it has not been confirmed whether or not this is a result of phosphorous incorporation in the diamond lattice. The other obvious substitutional dopant which should create n-type diamond is

nitrogen. Although it has been shown [93] that nitrogen readily dissolves in diamond, the material is ineffective since the corresponding donor level is 1.7eV below the bottom of the conduction band; a magnitude of energy which is too large to allow the material to be electrically active. Both ion implantation and CVD experiments have been performed with nitrogen.

The preparation of n-type diamond is not simply limited to the introduction of substitutional impurities, however, since it is known from nuclear reaction studies [99] that lithium occupies an interstitial site in the diamond lattice and can donate its $2s^1$ electron to the conduction band since this is not involved in bonding to carbon. It has also been theoretically predicted that sodium is a potential shallow donor which is also expected to occupy an interstitial site [42]. Recent ion implantation experiments with Li and Na by Kalish *et al.* [100] have resulted in conductivities directly related to the presence of the implanted ion residing in a relatively undamaged diamond matrix although there is some dispute concerning the mechanism of conduction within the crystal.

Three years prior to this experiment, Mort *et al.* [101] attempted to introduce lithium into diamond by placing previously grown diamond films in quartz ampoules containing lithium metal. The ampoules were designed to ensure that the samples would not directly contact the lithium but would only be exposed to its vapour. After evacuating to a pressure of $\sim 10^{-8}$ Torr, the ampoules were sealed off and placed inside a furnace held at temperatures varying from 400 to 900°C, for intervals ranging from a few minutes to half an hour. The presence of lithium in the films was qualitatively determined by standard SIMS techniques. These results also showed that the concentration of Li was a maximum at the surface but decreased within ~3000 Å to a constant value in the sample bulk. Only small changes in electrical conductivity between the samples and undoped diamond were observed. It was thought a chemical reaction between atmospheric oxygen and lithium which had diffused from the bulk of the diamond to its surface may have deteriorated the material's electrical performance.

Mort's work perhaps bears closest resemblance to the experiment carried out in this chapter. Apart from technique, the major difference is that instead of simply exposing a diamond film to lithium vapour generated from our source and then measuring its conductivity, we attempted to sandwich the lithium between two layers of diamond by growing another diamond film on top of lithium in the hope that this would prevent possible chemical reactions occurring when the lithium doped diamond was exposed to the atmosphere.

2) Doping of Diamond with the Li Source by MWECVD

a. Experimental

A brief outline of MWECVD can be found by consulting page 24. In order to fully understand the procedure adopted during this experiment it is best to refer to the schematic diagram which represents the MWECVD apparatus on page 40. The thick arrow pointing downwards represents the part of the machine where the cell holder (the same type as was used during the MBE experiment with the K source - Fig. 6-1) containing three lithium sources was positioned. This is known as the loadlock since it is normally used to load substrates into the spherical multiport growth chamber where diamond film growth takes place.

Before any doping was carried out, a layer of diamond was grown in the spherical chamber by the following method. A 4" diameter Si substrate of crystallographic orientation (100) was placed on the graphite stage (see Fig. 1-13) and heated to 1120°C. A 99.5% CH_4/0.5% H_2 mixture was introduced to the chamber until the pressure remained constant at 45 Torr. The microwave power (400 W) was then switched on to generate a plasma and growth was carried out over a period of 20 hrs.. It was calculated that the temperature of the diamond during growth was 700°C.

Once growth had been terminated the diamond film on Si(100) was removed from the spherical chamber via the loadlock and the surface morphology examined by SEM.

The diamond was placed back in the loadlock which was then evacuated to ~10^{-6} mbar with a turbo-molecular pump and the lithium source positioned approximately 10 cm above it. On heating the Li source at 250°C and applying a DC potential of 10 V for 17 hrs. it was noted that the current flowing through the cells fell from 3.10 mA to 0.48 mA.

Removal of the Li/diamond/Si(100) wafer from the loadlock and back into the spherical chamber was followed by growth of diamond with exactly the same method as previously outlined. In-situ optical emission spectroscopy of the contents of the resulting plasma was carried out during this growth - the results of which are presented below.

A further SEM analysis and a laser ionisation mass analysis (LIMA) were then performed on the resulting material in attempts at examining morphology of the crystal after growth and detecting Li respectively.

b. Results

SEM Images of the Diamond Layer Before Exposure to Lithium

SEM images (Figs. 6-12 a-c) were recorded from the outskirts of the silicon wafer to the centre of the polycrystalline diamond deposit. They show that the diamond crystallites are larger nearer the centre of the film. This is because the growth temperature is comparatively high at the centre.

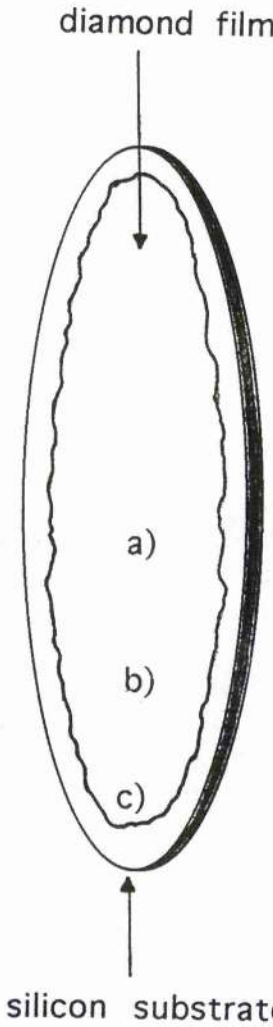

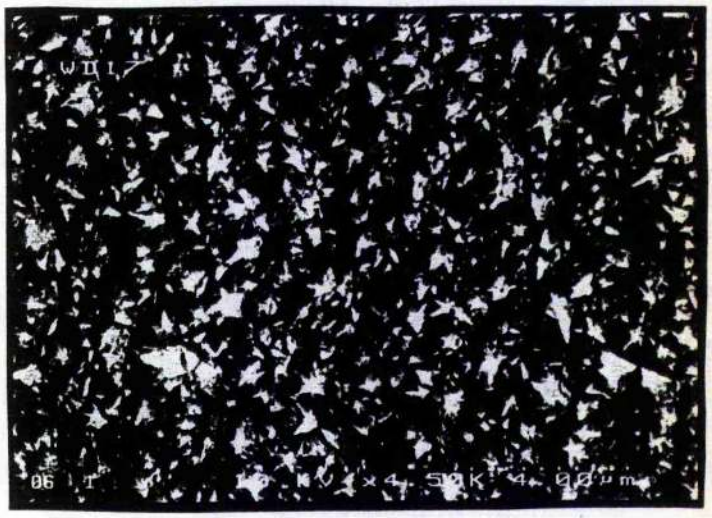

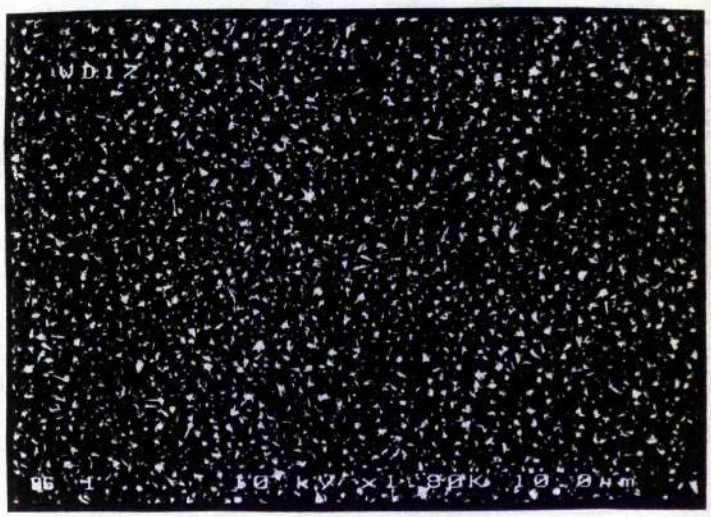

Fig. 6-12. SEM images of the diamond surface before exposure to lithium. a) 4.5 cm from the edge of the Si (100) substrate, b) 2.0 cm, c) 0.8 cm.

Optical Emission Spectra of the Plasma after Exposure to Lithium

Fig. 6-13 is a typical optical emission (OE) spectrum of a methane/hydrogen plasma without any lithium. To record data like this, the light produced by the whole plasma ball is collected through a quartz window, coupled to a quartz fibre optic guide and analysed in the range 200-900 nm. The spectral features represent electron excitation processes occurring within the plasma. By comparing the absorptions with literature values it is possible to determine the plasma contents and investigate diamond deposition chemistries.

Fig. 6-14 is an OE spectrum recorded directly after switching the plasma on once the Li coated diamond had been positioned inside the growth chamber. Reasons for the loss of sensitivity compared with Fig. 6-13 were due to the absence of focusing optics which couple light from the plasma into the fibre optics. Most notable are the single peaks at 655 nm and 671 nm due to H_α and Li respectively. The peak at 768 nm is due to potassium which was thought to have arisen from contamination of the cell holder which had previously been used during the potassium doping of ZnSe.

A second OE spectrum was recorded 5 minutes after switching the plasma on (Fig. 6-15a) and showed that both the H_α and K lines had diminished into the background noise leaving a strong Li signal at 671 nm.

After 10 minutes a third OE spectrum was recorded (Fig. 6-15b) which still indicated the presence of Li within the plasma.

These results suggested that the plasma was too hot to allow the lithium to be trapped by fresh diamond.

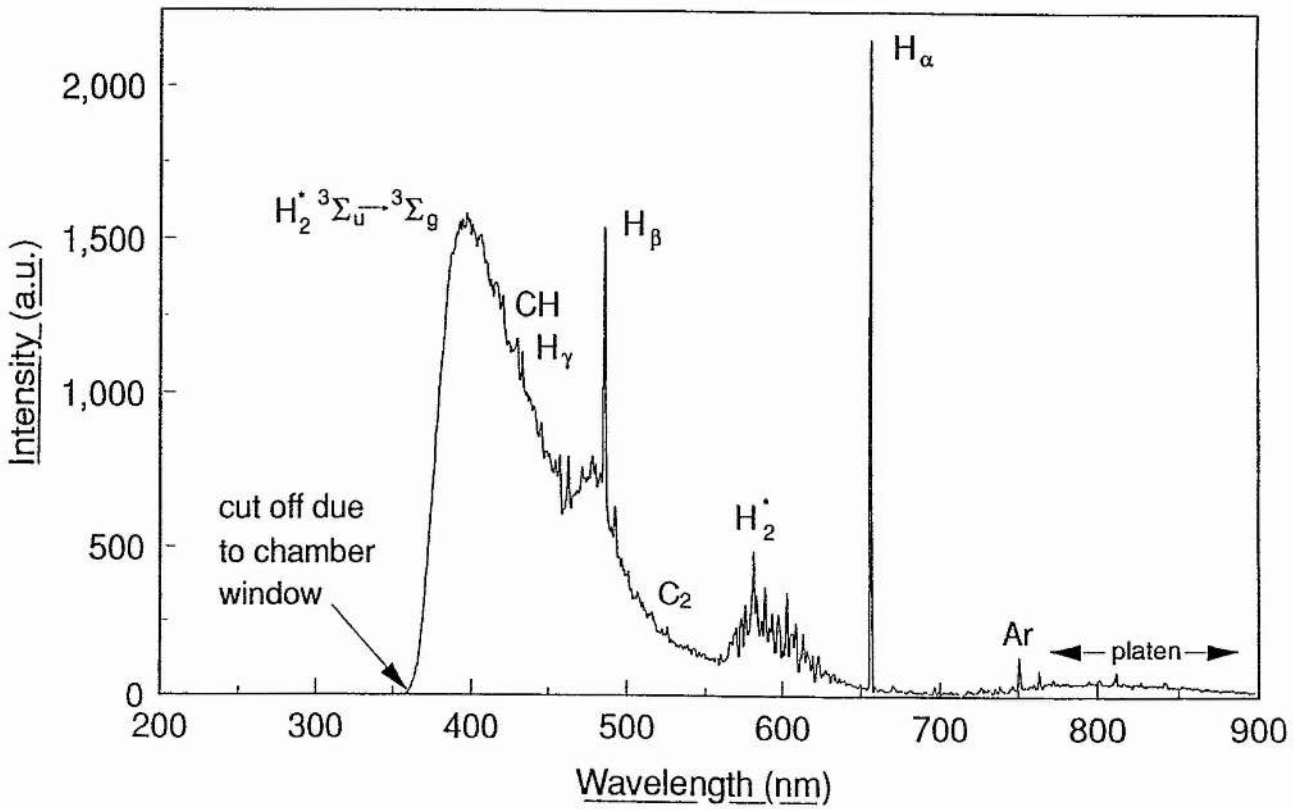

Fig. 6-13. Typical optical emission spectrum of a methane/hydrogen plasma. From reference [48].

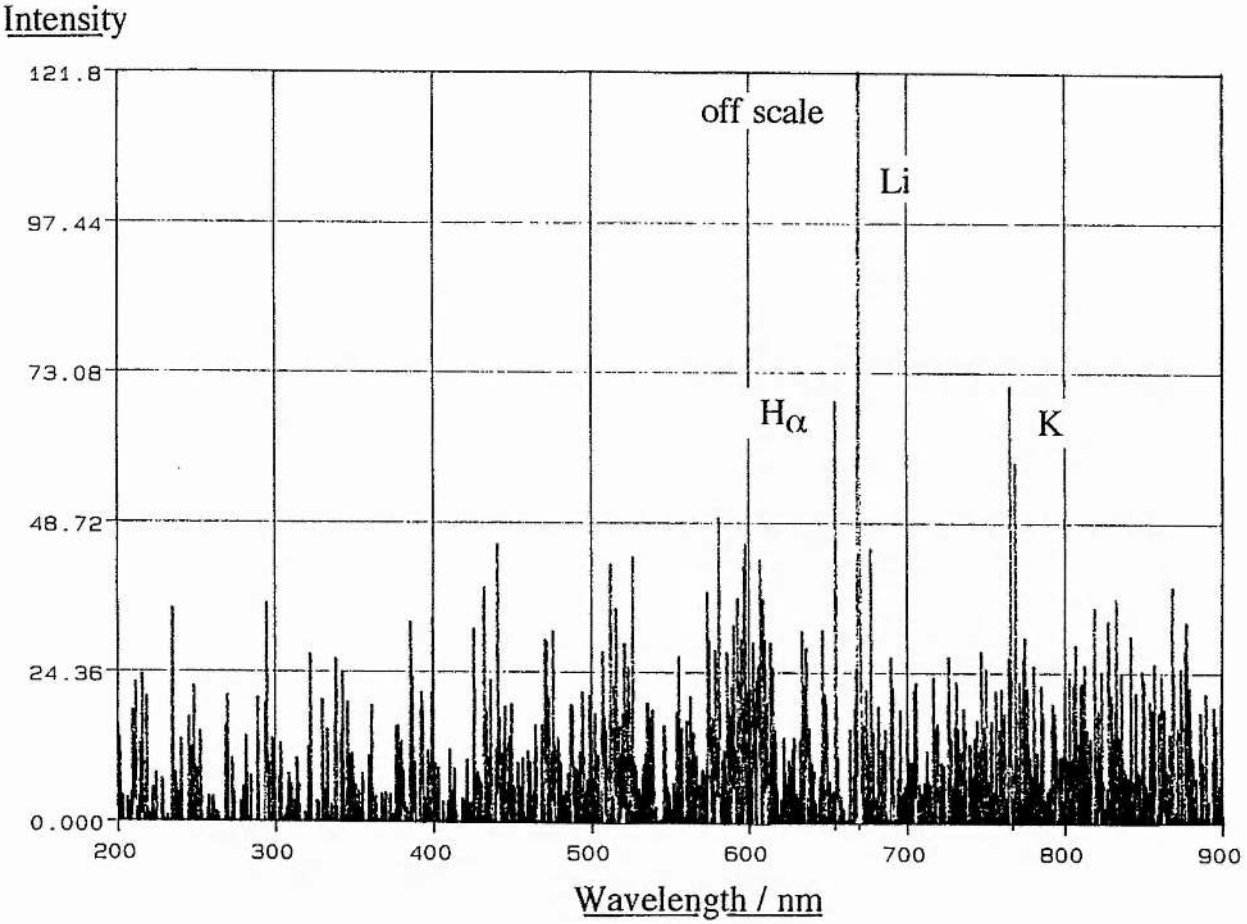

Fig. 6-14. Optical emission spectrum recorded directly after switching the plasma on to grow diamond on top of the deposited lithium. The sharp line at 671 nm corresponds to lithium and the doublet at 768 nm to potassium.

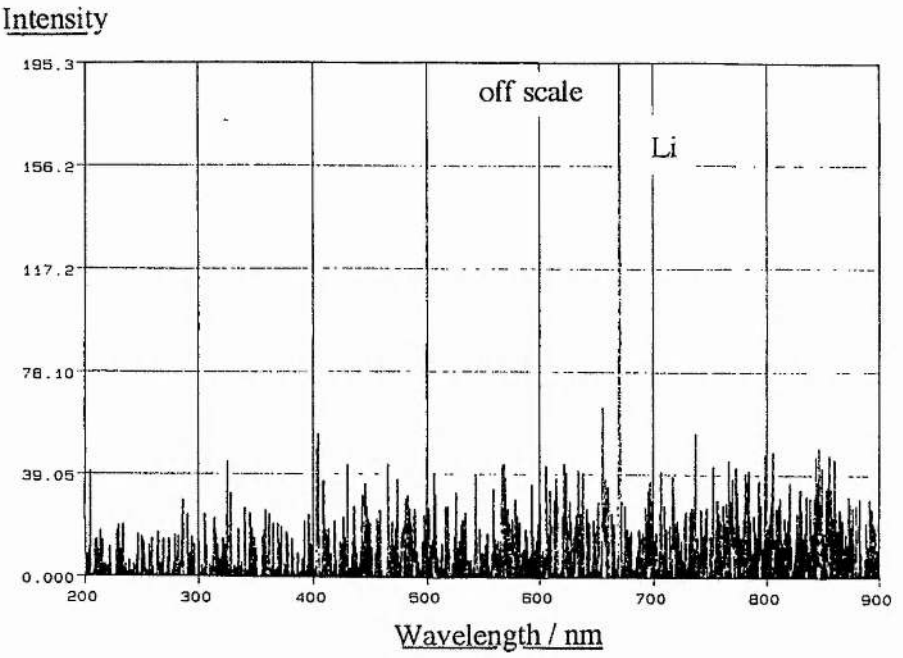

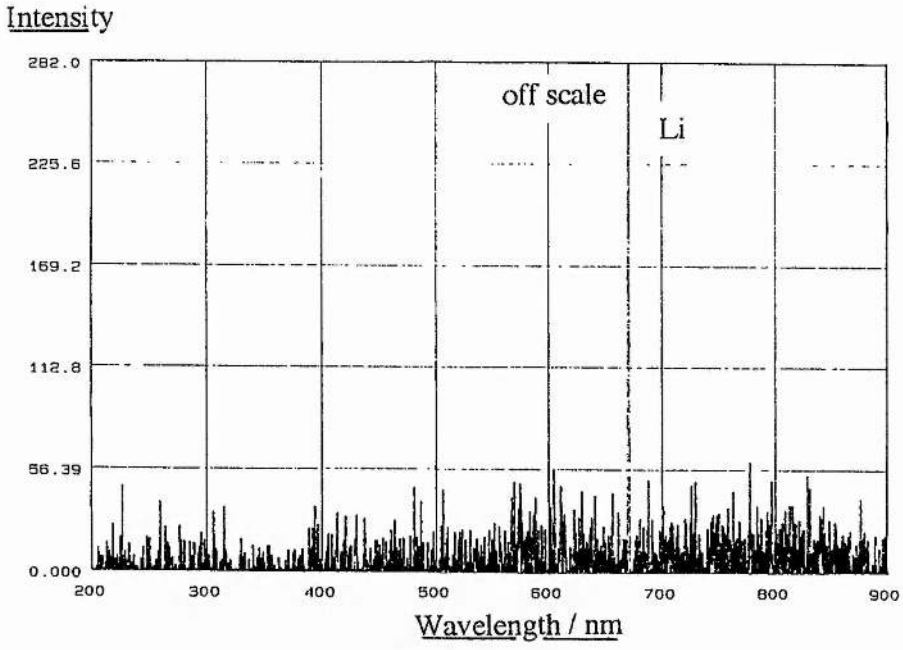

Fig. 6-15. Further OE spectra. a) Recorded 5 minutes after switching the plasma on. b) Recorded 10 minutes after. In both spectra the potassium observed in Fig. 6-13 is no longer present, but Li is.

SEM Images of the Diamond/Lithium/Diamond Composite

After growing more diamond on top of the lithium the wafer was removed from the MWECVD apparatus and cut into slices. The edge of one such slice was examined by SEM (Fig. 6-16 a and b) and showed that growth of the second diamond layer had been suppressed. Reasons why this should occur are still unclear.

LIMA of the Diamond/Lithium/Diamond Composite

Fig. 6-17a is a LIMA spectrum taken from the surface of the layer where the diamond growth had been suppressed. No lithium was detected and the peaks at 12, 24, 36, 48, 60, and 72 were due to C, C_2, C_3, C_4, C_5, and C_6 respectively. The pulses from the Nd:YAG laser which are used to ablate the surface of the analyte reach a depth of approximately 0.2 μm per pulse. After 6 pulses (corresponding to a depth of 1.2 μm) there was still no lithium detected (Fig. 6-17b).

A third LIMA experiment (Fig. 6-17c) with parts of the diamond wafer being examined from the opposite side of the wafer (the 1st diamond layer/Si substrate side) showed that there was still no lithium present.

3) Conclusions

The optical emission spectra (Figs. 6-14 and 6-15) recorded after exposing the 1st diamond layer to lithium vapour generated from the source provide clear evidence that lithium can be deposited onto diamond prior to switching the plasma on.

The fact that no lithium was detected by LIMA (Fig. 6-17) in the diamond after attempting to trap it between two layers may be due to two reasons. Either the temperature of the plasma is so hot that it causes all the deposited lithium to evaporate from the diamond surface, or the detection limit of the LIMA spectrometer (10 ppm) is not sensitive enough to locate the lithium. Secondary Ion Mass Spectrometry (SIMS), however, can detect elements on a part per billion

scale and this technique may have to be adopted in order to complete the analysis. Another means of determining whether or not any lithium doping has occurred would involve performing electrical measurements on the wafer and comparing the resistivity with a literature value previously obtained for an undoped crystal. An enhanced conductivity would indicate that the doping experiment has been successful.

Finally, restricted growth of the second diamond layer (Fig. 6-16) is a result which has not been previously observed during any MWECVD experiments. It seems likely that the presence of lithium was responsible and further experiments, where the 1st diamond layer is exposed to lithium for variable periods of time, should be carried out in order to investigate this.

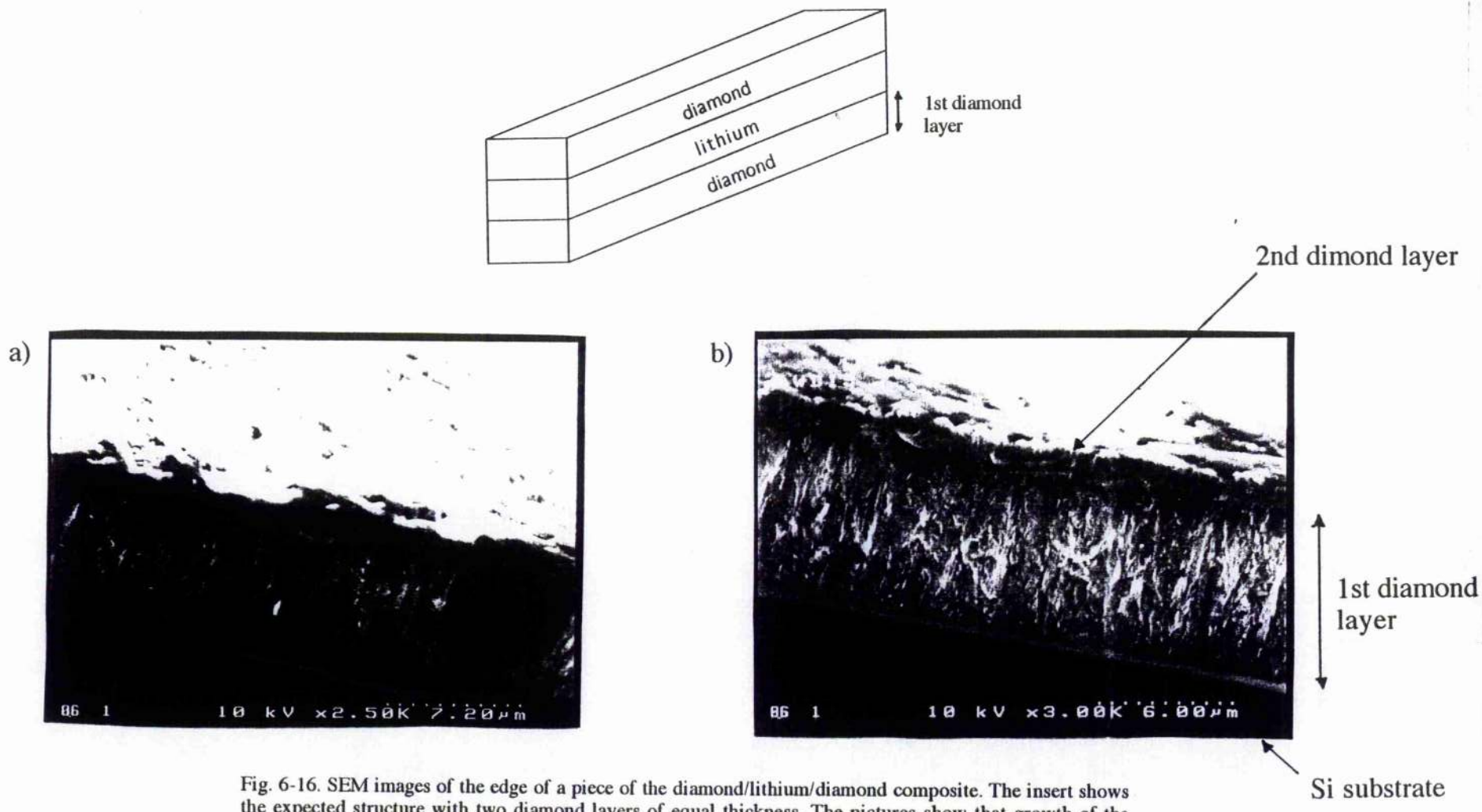

Fig. 6-16. SEM images of the edge of a piece of the diamond/lithium/diamond composite. The insert shows the expected structure with two diamond layers of equal thickness. The pictures show that growth of the second diamond layer has been inhibited. Both pictures have been taken from the same sample. b) was taken with more tilt and at higher magnification than a).

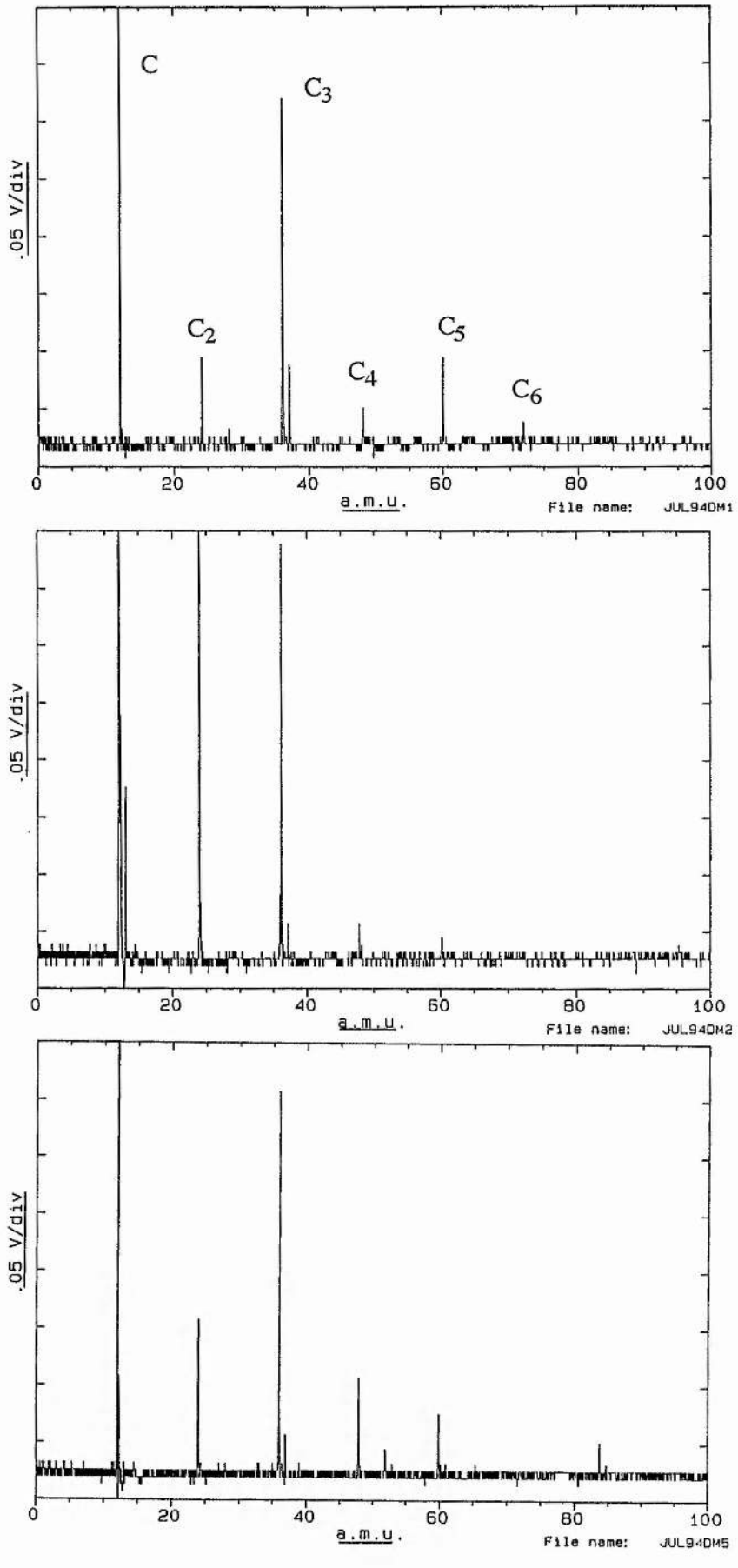

Fig. 6-17. LIMA spectra of the diamond wafer shown in Fig. 6-15. a) Taken from the surface of the layer where diamond growth had been suppressed. b) Taken at a depth of 1.2 μm into this layer. c) Recorded from the opposite side of the wafer (the 1st diamond layer/Si substrate side).

Chapter 7

Conclusions and Suggestions for Further Work

All solid state cells consisting of a solid ceramic electrolyte, an intercalation electrode and a metal gauze electrode have been successfully fabricated. These cells can produce beams of lithium, sodium or potassium when polarised in high vacuum. A major potential difficulty with cells of this type is the mechanical stability of the ceramic electrolyte-ceramic electrode interface. I have succeeded in developing cells with mechanically stable interfaces. During manufacture of the lithium cell, the composition between the intercalation electrode and electrolyte had to be graded to develop a robust ceramic-ceramic interface capable of thermal cycling between 25°C and 350°C.

An obvious suggestion for further work would be to demonstrate that all solid state cells could be used to generate beams of other elements. Recent preparation of the new intercalation compound; $Zn_{0.4}WO_2Cl_2$ [102] which has mobile Zn^{2+} cations, presents the possibility of fabricating solid state cells for the production of Zn vapour. In order to achieve this, a ceramic solid electrolyte which conducts Zn^{2+} ions would also have to be available. Recent research into multivalent beta aluminas has shown that it is possible to prepare Zn(II) β"-alumina [103] by ion exchanging sodium β"-alumina.

Since this work has demonstrated that beams of highly reactive elements can be generated by solid state electrochemical cells which eliminate any safety hazards encountered when these elements are handled in their pure form, the concept could be extended to the generation of other reactive elements such as rubidium and fluorine. These elements also have potential applications in the semiconductor industry.

Turning now to the electrochemical mechanisms responsible for alkali metal production. At 10^{-3} mbar alkali metals or alkali metal containing compounds from each source nucleate and grow on the working electrode and then evaporate. When operating in UHV both potassium and sodium sources emit their vapours without any observed nucleation unlike lithium emission which still involves this stage. It

has been assumed that the pressure in the chamber is responsible for changing the mechanisms of sodium and potassium production. More conclusive evidence to back this assumption up could be obtained by recording cyclic voltammograms and chronoamperometry results at intermediate pressures between 10^{-3} mbar and UHV. Going from 10^{-3} mbar to UHV should show both the gradual disappearance of the nucleation loop on cyclic voltammetric data and diminution of the rise of current with time during potential step experiments.

In-situ mass spectrometry of sodium emission during a slow sweep cyclic voltammetry experiment has indicated the presence of two peaks at m/z = 23 and m/z = 39. The former of these is due to sodium whilst the later is thought to represent an NaO^+ fragment which is either produced electrochemically at the Na-BASE/stainless steel interface or is the result of a gas phase reaction between sodium and oxygen present in the UHV chamber. This experiment should be repeated for potassium and lithium sources.

During all experiments concerning the electrochemical mechanisms behind alkali metal evolution the electrical failure of cartridge heaters within the stainless steel heating block, which were required to maintain the cells at 350°C whilst all measurements were made, occurred frequently. The reason for this fault was due to each heater being insufficiently powerful. To avoid this problem in future, cartridge heaters capable of sustaining higher temperatures should be used instead.

Recent advances in microscopy have led to the development of scanning probe microscopy (SPM), a technique which provides resolution intended primarily for atomic level surface imaging. There is a possibility that an SPM capable of analysing the events occurring on the stainless steel gauze in UHV will eventually become available.

Finally, and most importantly, the semiconductor growth results are discussed.

The potassium source has been used successfully during the production of p-type ZnSe [104]. Photoluminescence spectroscopy, capacitance-voltage profiling and SIMS results have demonstrated this. There is, however, a considerable barrier preventing potassium incorporation into the growing chalcogenide. As mentioned in the discussion on p. 155 this may be due to insufficient exposure of the ZnSe to the source. Alternative methods of improving the quality of the semiconductor include doping with sodium which has a smaller atomic radius than potassium and is therefore more likely to effectively incorporate itself in the zinc sites. Trying photoassisted MBE [105] where an argon ion laser is directed onto the growing semiconductor may also enhance the electrical activity of the material. The rationale for this approach is to provide, by means of the incident photon beam, the energy required to surmount surface potential barriers which might ordinarily prevent or limit the incorporation of the dopant species at tetrahedrally bonded sites, and thus increase the degree of dopant activation. Also, lowering the growth temperature of the crystal may reduce any kinetic barriers responsible for hindering dopant incorporation.

Using the lithium source during attempts at preparing n-type diamond with MWECVD apparatus has shown that the source can coat a diamond film with lithium. Attempting to "sandwich" the lithium by growing a second diamond layer above the lithium demonstrated that the temperature within the growth chamber was too high to allow the deposited lithium to remain attached to the 1st diamond layer. As a consequence, no lithium was detected in the film by LIMA. Further semiconductor characterization experiments such as SIMS and electrical measurements need to be carried out, however, before any serious conclusions can be drawn from this experiment. If these results are also found to be negative then a different method of introducing lithium from the source should be attempted. For example, instead of trying to grow a layer of diamond on top of the lithium, the source should be exposed to the plasma in order to trap the lithium within the growing diamond lattice.

Equivalent Circuit Written in Fortran

The following computer programme represents the equivalent circuit shown in Fig. 5-18.

```
  ADDED PART OF CNLS PROGRAM TO RUN ON MICROSOFT FORTRAN, V4
                J.R. Macdonald, 05/30/87
              LEVM-OLSON SUBROUTINE JSUB
SUBROUTINE KSUB(M,FREQ,P,F)
IMPLICIT REAL*8(A-H,O-Z)
DOUBLE PRECISION P(*),F(*),FREQ(*),FI,RB,CG,RCT,FIO,TDE
COMPLEX*16 ZT,IOMEGA,YB,YA,YP

RB=P(1)
CG=P(2)
RCT=P(3)
FIO=P(4)
TDE=P(5)
FI=P(6)
DO 100 I=1,M
OMEGA=FREQ(I)
IOMEGA=DCMPLX(0.,OMEGA)
YA=1.DO/RB+IOMEGA**FIO*CG
YP=(IOMEGA)**FI*TDE
YB=1.DO/RCT+YP
ZT=1.DO/YB+1.DO/YA
F(I)=DREAL(ZT)
F(I+M)=DIMAG(ZT)
CONTINUE

RETURN
END
```

Where: FIO and CG represent the bulk CPE (C_b)

FI and TDE represent the interfacial CPE (C_{dl})

RB and RCT represent the bulk resistance (R_b) and charge transfer resistance (R_{ct}) respectively.

Symbols that seldom occur have not been included in the following list, their meaning having been given in the text.

A = effective contact or etch area (m^2)

a = activity

C = capacitance (Farads)

c = concentration (mol cm^{-3})

c^{σ} = concentration at the electrode surface (mol cm^{-3})

c^{∞} = concentration in the bulk solution (mol cm^{-3})

D = diffusion coefficient ($cm^2\ s^{-1}$)

E = electrode potential (V) *or* energy (J)

E^o = standard potential (V)

$E^{o'}$ = formal potential (V)

E_M = voltage amplitude during an AC impedance experiment (V)

e = charge of electron (1.60219 C)

f = frequency (s^{-1})

F = Faraday's constant (96500 C mol^{-1})

i = complex number operator ($\sqrt{-1}$)

j = current density (A cm^{-2})

j_o = exchange current density (A cm^{-2})

h = height (cm) *or* Planck constant (Js)

k = electrode reaction rate constant (cm s^{-1})

k^o = formal rate constant (cm s^{-1})

k_B = Boltzmann constant (1.381×10^{-23} JK^{-1})

k^* = rate of incorporation of atoms into a growth centre (mol $cm^{-2}\ s^{-1}$)

M = molecular weight (g mol^{-1})

N = carrier concentration

n = number of electrons exchanged

P = κZ - electrode potential independent pre-exponential factor (cm s^{-1})

Q = charge stored in a depletion region of depth W_d

$Q(r)$ = charge required to form a cylinder of any radius r (C)

q = charge (C) or elementary charge (1.602×10^{-19} C)

R = gas constant (8.314 J K^{-1} mol^{-1}) or resistance (Ω)

r = radius (m)

t = time (s)

T = temperature (K)

V = applied voltage ((-)ve in reverse bias sense) (V)

W_d = depletion depth

Z = impedance (Ω)

Z' = real component of impedance (Ω)

Z'' = imaginary component of impedance (Ω)

x = distance perpendicular to the electrode surface (cm)

α = electron transfer coefficient

δ = reaction length of the order of a molecular diameter (m)

ΔH = potential dependent activation enthalpy (J mol^{-1})

ΔH^o = potential independent activation enthalpy (J mol^{-1})

$\Delta H_o^{\#}$ = activation energy of electrode reaction (J mol^{-1})

ε = dielectric constant of the solid electrolyte

ε_r = relative permittivity of the semiconductor

ε_o = vacuum permittivity (8.85×10^{-14} Fcm^{-1})

Φ = "built in" or contact potential (V)

η = overpotential (V)

$\kappa Z = \kappa k_B T \delta / h$

κ = transmission cofficient

θ = phase angle

ρ = density (g cm^{-3})

ω = angular frequency ($2\pi f$)

[1] M. Faraday, in *Experimental Researches in Electrochemistry*, Taylor and Francis, London (1839).

[2] F. Haber and St. Tolloczko, *Z. anorg. Chem.*, **41** (1904) 407.

[3] R. T. Foley, *J. Electrochem. Soc.*, **116** (1969) 13C.

[4] K. Kiukkola and C. Wagner, *J. Electrochem. Soc.*, **104** (1957) 379.

[5] B. B. Owens and G. R. Argue, *Science*, **157** (1967) 308.

[6] N. Weber and J. T. Kummer, *Proc. Ann. Power Sources Conf.*, **21** (1967) 37.

[7] J. O'. M. Bockris and A. K. Reddy, *Modern Electrochemistry*, Vol. 1, p. 22, Macdonald, London (1970).

[8] J. Koryta, J. Dvorak, L. Kavan, *Principles of Electrochemistry*, p. 79, Wiley, Chichester (1993).

[9] W. I. Archer and R. D. Armstrong, in *Electrochemistry*, Vol. 7 (Edited by H. R. Thirsk), p. 157, The Chemical Society, London (1980).

[10] D. O. Raleigh, in *Electroanalytical Chemistry*, Vol. 6 (edited by A. J. Bard), p. 98, Marcel Dekker, New York (1973).

[11] P. G. Bruce and I. Abrahams, *J. Solid State Chem.*, **95** (1991) 74.

[12] M. S. Whittingham, *Science*, **192** (1976) 1126.

[13] P. G. Bruce and M. Y. Saidi, *Solid State Ionics*, **51** (1992) 187.

[14] G. J. Dudley and B. C. H. Steele, *J. Solid State Chem.*, **21** (1977) 1.

[15] D. G. Wickham and W. J. Croft, *J. Phys. Chem. Solids*, **7** (1958) 351.

[16] M. M. Thackeray, W. I. F. David, P. G. Bruce, and J. B. Goodenough, *Mat. Res. Bull.*, **18** (1983) 461.

[17] G. Rob Lee and Joe A. Crayston, *Adv. Mater.*, **5 (No. 6)** (1993) 434.

[18] Olivier Tillement, *Solid State Ionics*, **68** (1994) 9.

[19] G. J. Davies, D. A. Andrews, and R. Heckingbottom, *J. Appl. Phys.*, **52 (12)** (1981) 7214.

[20] H. Rickert, *Electrochemistry of Solids*, p. 129, Springer-Verlag, Berlin (1982).

[21] H. Rickert, C. D. O'Brian, *Z. phys. Chem. Neue Folge*, **31** (1962) 71.

[22] D. A. Andrews, M. Y. Kong, R. Heckingbottom, and G. J. Davies, *J. Appl. Phys.*, **55 (4)** (1984) 841.

[23] K. A. Prior, J. M. Wallace, J. J. Hunter, S. J. A. Adams, M. J. L. S. Haines, M. Saoudi and B. C. Cavenett, *J. Crystal Growth*, **101** (1990) 176.

[24] J. Simpson, J. M. Wallace, S. Y. Wang, H, Stewart, J. J. Hunter, S. J. A. Adams, K. A. Prior and B. C. Cavenett, *Semicond. Sci. Technol.*, **7** (1992) 464.

[25] P. G. Bruce, I. Abrahams, K. A. Prior and H. Stewart, *Solid State Ionics*, **53** (1992) 1.

[26] J. T. Kummer and N. Weber, U.S. Patent 3,458,356 (1968), Assigned to Ford Motor Company.

[27] M. L. Underwood, R. M. Williams, B. Jeffries-Nakamura, M. A. Ryan, and D. O'Connor, in: Proc. Eight Symp. Space Nuclear Power systems, eds. M. El-Genk and M. Hoover (Am. Institute of Physics, New York, 1991).

[28] R. M. Williams, G. Nagasubramanian, S. K. Khanna, C. P. Bankston, A. P. Thakoor, and T. Cole, *J. Electrochem. Soc.*, **133** (1986) 1587.

[29] R. M. Williams, B. Jeffries-Nakamura, M. L. Underwood, M. A. Ryan, D. O'Connor, and S. Kikkert, *Solid State Ionics*, **53-56** (1992) 806.

[30] R. M. Williams, M. E. Loveland, B. Jeffries-Nakamura, M. L. Underwood, C. P. Bankston, H. Leduc, and J. T. Kummer, *J. Electrochem. Soc.*, **137** (1990) 1709.

[31] R. M. Williams, B. Jeffries-Nakamura, M. L. Underwood, C. P. Bankston, and J. T. Kummer, *J. Electrochem. Soc.*, **137** (1990) 1716.

[32] R. D. Armstrong, T. Dickinson and J. Turner, *J. Electroanal. Chem.*, **44** (1973) 157.

[33] R. D. Armstrong, *J. Electroanal. Chem.*, **52** (1974) 413.

[34] E. Butchereit, M. Schreiber and J. Schoonman, *Solid State Ionics*, **69** (1994) 1.

[35] Stanley Bruckenstein and R. Rao Gadde, *J. Am. Chem. Soc.*, **93** (3) (1971) 793.

[36] X. H. Xia and T. Iwasita, *J. Electrochem. Soc.*, **140** (1993) 2559.

[37] H. M. Yates, J. O. Williams and D. J. Cole-Hamilton, *Appl. Phys. Lett.*, **59** (**22**) (1991) 2835.

[38] T. Yasuda, I. Mitsuishi, and H. Kukimoto, *Appl. Phys. Lett.*, **52** (**1**) (1988) 57.

[39] J. O. Williams, *Angew. Chem. Int. Ed. Engl. Adv. Mater.*, **28** (**No. 8/9**) (1989) 1110.

[40] P. K. Bachmann, *Adv. Mater.*, **2** (**No. 4**) (1990) 195.

[41] S. A. Kajihara, A. Antonelli, and J. Bernholc, *Mat. Res. Soc. Symp. Proc.*, **162** (1990) 315.

[42] S. A. Kajihara, A. Antonelli, J. Bernholc, and R. Car, *Phys. Rev. Lett.* **66** (1991) 2010.

[43] H. Cheng, J. M. DePuydt, J. E. Potts and M. A. Haase, *J. Crystal Growth*, **95** (1989) 512.

[44] J. Lilja, M. Toivonen, P. Wysocki and M. Pessa, *Vacuum*, **40** (1990) 491.

[45] N. S. Clarke, *Chem. Brit.* **25** (1989) 484.

[46] J. H. Batey, J. M. Tedder, *J. Chem. Soc. Perkin Trans. II*, (1983) 1263.

[47] M. T. Mason, in *Modern Aspects of Mass Spectrometry*, p. 61, Plenum Press, New York (1968).

[48] M. G. Jubber, J. I. B. Wilson, I. C. Drummond, P. John and D. K. Milne, *Vacuum*, **45** (1994) 499.

[49] R. D. Armstrong, M. Fleischmann and H. R. Thirsk, *J. Electroanal. Chem.*, **11** (1966) 208.

[50] E. Bosco and S. K. Rangarajan, *J. Electroanal. Chem.*, **134** (1982) 213.

[51] M. Y. Abyaneh, *Electrochimica Acta*, **36** (1991) 727.

[52] P. J. Sonneveld, W. Visscher and E. Barendrecht, *Electrochimica Acta*, **37** (1992) 1199.

[53] W. Obretenov, U. Schmidt, W. J. Lorenz, G. Staikov, E. Budevski, D. Carnal, U. Muller, H. Siegenthaler and E. Schmidt, *J. Electrochem. Soc.*, **140** (1993) 692.

[54] J. H. Sluyters, *Rec. Trav. Chim.*, **79** (1960) 1092.

[55] M. D. Rogers and C. A. Vincent, *J. Phys. D: Appl. Phys.*, **25** (1992) 1264.

[56] I. Abrahams and P. G. Bruce, *Acta Cryst.*, **B47** (1991) 696.

[57] R. D. Shannon, B. E. Taylor, A. D. English, and T. Berzins, *Electrochimica Acta*, **22** (1977) 783.

[58] J. P. Boilot, G. Collin, Ph. Colomban, and R. Comes, *Phys. Rev. B*, **22 (12)** (1980) 5912.

[59] S. Nariki, S. Itok, K. Kozawa, T. Uchida, and N. Yoneda, *Solid State Ionics*, **40/41** (1990) 95.

[60] G. J. Dudley and B. C. H. Steele, *J. Mat. Sci.*, **13** (1978) 1267.

[61] C. Fouassier, G. Matejka, J. Reau, and P. Hagenmuller, *J. Solid State Chem.*, **6** (1973) 532.

[62] G. Yamaguchi and K. Suzuki, *Bull. Chem. Soc. Jpn.*, **41** (1968) 93.

[63] J. S. Subramanian, S. A. Akbar, and K. S. Goto, *J. Electrochem. Soc.*, **139 (9)** (1992) 2562.

[64] L. Guillet, *Rev. Met.*, **1** (1904) 155.

[65] F. P. A. Robinson, *Stainless Steel - The Miracle Alloy*, Inaugural Lecture delivered on 5th April 1979, Witwatersrand University Press, Johannesburg, 1980.

[66] P. R. Elliot, *Constitution of Binary Alloys*, McGraw-Hill Book Company, p. 421, New York (1958).

[67] D. M. Kolb, in *Advances in Electrochemistry and Electrochemical Engineering*, Vol. 11 (Edited by P. Delahay and C. W. Tobias), p. 127, Wiley, New York (1978).

[68] S. C. Roy, 4th year undergraduate project.

[69] R. D. Armstrong and Adrienne A. Metcalfe, *J. Electroanal. Chem.*, **71** (1976) 5.

[70] Handbook of Chemistry and Physics, 72nd edition (1991-1992), p. 5-69 - 5-70, CRC Press, Boca Raton.

[71] Graham Hills, Azar Kaveh Pour and Benjamin Scharifker, *Electrochimica Acta*, **28** (7) (1983) 891.

[72] Gamini Gunawardena, Graham Hills, Irene Montenegro and Benjamin Scharifker, *J. Electroanal. Chem.*, **138** (1982) 225.

[73] S. Gilman, in *Electroanalytical Chemistry*, Vol. 2 (edited by A. J. Bard), p. 111, Marcel Dekker, New York (1967).

[74] James Ross Macdonald, *Electrochimica Acta*, **38** (**14**) (1993) 1883.

[75] My thanks to Dr Przemyslaw Los for writing this programme.

[76] P. G. Bruce, A. R. West and D. P. Almond, *Solid State Ionics*, **7** (1982) 57.

[77] Herbert Engstrom, J. B. Bates, W. E. Brundage and J. C. Wang, *Solid State Ionics*, **2** (1981) 265.

[78] A. K. Jonscher, *Nature*, **267** (1977) 673.

[79] L. Nyikos and T. Pajkossy, *Electrochimica Acta*, **30** (**11**) (1985) 1533.

[80] R. De Levie, *Electrochimica Acta*, **10** (1965) 113.

[81] G. J. Brug, A. L. G. Van Der Eeden, M. Sluyters-Rehbach and J. H. Sluyters, *J. Electroanal. Chem.*, **176** (1984) 275.

[82] Margaretha Sluyters-Rehbach and Jan H. Sluyters in, *Electroanalytical Chemistry*, Vol. 4 (edited by A. J. Bard), p. 1, Marcel Dekker, New York (1970).

[83] R. D. Armstrong and M. Todd, private communication.

[84] J. Koryta, J. Dvorak, L. Kavan, *Principles of Electrochemistry*, p. 266, Wiley, Chichester (1993).

[85] Dr A. Iqbal (Ciba Geigy) A lecture on organic photoconductors at St. Andrews University (1994).

[86] Takahiro Matsumoto, Jun Takahashi, Teruyuki Tamaki, Toshiro Futagi, Hidenori Mimura, and Yoshihiko Kanamitsu, *Appl. Phys. Lett.*, **64** (**2**) (1994) 226.

[87] Z. L. Wu, J. L. Merz, C. J. Werkhoven, B. J. Fitzpatrick, and R. N. Bhargava, *Appl. Phys. Lett.*, **40** (**4**) (1982) 345.

[88] Qiu, J. M. DePuydt, H. Cheng and M. A. Haase, *Appl. Phys. Lett.*, **59** (23) (1991) 2992.

[89] I. S. Hauksson, J. Simpson, S. Y. Wang, K. A. Prior and B. C. Cavenett, *Appl. Phys. Lett.*, **61** (18) (1992) 2208.

[90] S. Y. Wang, J. Simpson, K. A. Prior, and B. C. Cavenett, *J. Appl. Phys.*, **72** (**11**) (1992) 5311.

[91] R. Heckingbottom, G. J. Davies and K. A. Prior, *Surface Science*, **132** (1983) 375.

[92] C. E. C. Wood and B. A. Joyce, *J. Appl. Phys.*, **49 (9)** (1978) 4854.

[93] Michael W. Geis and John C. Angus, *Scientific American*, October 1992, 64.

[94] Gennady Sh. Gildenblat, Stephen A. Grot, and Andrzej Badzian, *Proceedings of the IEEE*, **79 (5)** (1991) 647.

[95] I. M. Buckley-Golder, R. Bullough, M. R. Hayns, J. R. Willis, R. C. Piller, N. G. Blamires, G. Gard and J. Stephen, *Diamond and Related Materials*, **1** (1991) 43.

[96] N. Fujimori, T. Imai and A. Doi, *Vacuum*, **36** (1986) 99.

[97] K. Okano, H. Kiyota, T. Kurosu and M. Iida, *Diamond and Related Materials*, **3** (1993) 35.

[98] C. A. Hewett, P. R. de la Houssaye, M. Roser, and J. R. Zeidler, *J. Electrochem. Soc.*, **139** (1992) 2977.

[99] G. Braunstein and R. Kalish, *Proc. Conf. on Ion Beam Modification of Materials*, Albany, July 1980.

[100] S. Prawer, C. Uzan-Saguy, G. Braunstein, and R. Kalish, *Appl. Phys. Lett.*, **63 (18)** (1993) 2502.

[101] K. Okumura, J. Mort, and M. Machonkin, *Appl. Phys. Lett.*, **57 (18)** (1990) 1907.

[102] P. G. Bruce, F. Krok, P. Lightfoot, J. L. Nowinski, and V. C. Gibson, *Solid State Ionics*, **53-56** (1992) 351.

[103] S. Sattar, B. Ghosal, M. L. Underwood, H. Mertwoy, M. A. Saltzberg, W. S. Frydrych, G. S. Rohrer, and G. C. Farrington, *J. Solid State Chem.*, **65** (1986) 231.

[104] P. G. Bruce, S. Roy, H. Stewart, and K. A. Prior, *Mat. Res. Soc. Symp. Proc.*, **293** (1993) 93.

[105] R. N. Bicknell, N. C. Giles, and J. F. Schetzina, *Appl. Phys. Lett.*, **49 (17)** (1986) 1095.